Final Report

Work Scope:	Materials Aging and Degradation (RC-5)
Project:	Project 17-12523 (NE0008699)
Title:	Experimental and Computational Studies of Stress Corrosion Cracking of Alloys 308/309 and 82/182 Weldments in Corrosive and Radiation Environment

PI:	Brent J. Heuser	University of Illinois at Urbana-Champaign
Co-PIs:	Xianming (David) Bai	Virginia Polytechnic and State University
	Gary S. Was	University of Michigan
	Benjamin W. Spencer	Idaho National Laboratory

Final Report for (Project 17-12523) Experimental and Computational Studies of Stress Corrosion Cracking of Alloys 308/309 and 82/182 Weldments in Corrosive and Radiation Environment

Materials Aging and Degradation (RC-5)

M2NU-17-IL-UIUC-030207-011

Brent J. Heuser (University of Illinois Urbana-Champaign/PI), Xianming (David) Bai (Virginia Polytechnic and State University), Benjamin Spencer (Idaho National Laboratory), and Gary S. Was (University of Michigan)

Executive Summary

The goal of the project was to determine factors that influence SCC and IASCC in weldments found in LWR nuclear power plants. We focused on a SA508-304L SS weldment fabricated by EPRI using gas tungsten arc welding and used an aggressive BWR normal water chemistry (NWC) immersion environment. This weldment used 309L butter and 308L groove filler material. The microstructure of the 309L butter was non-uniform, exhibiting a 20–30μm thick martensitic layer closest to the SA508 interface, a 1–4 mm thick single γ austenite phase dilution zone, and a γ–δ duplex region extending to the 308L groove filler. The 308L groove filler had an entirely γ–δ duplex microstructure. Two approximately 1-inch thick 304L and SA508 plates approximately 12 by 6 square inches were joined using standard nuclear grade welding techniques. This included a post weld heat treatment of the 309L butter after application, a 0.32 cm fit-up root opening, and 57 bead lines of 308L groove filler applied in 18 layers. A 60 degree weld bevel angle was used and the 309L butter was 1.5 cm thick. Displacement cascade damage was induced using proton irradiation at the Michigan Ion Beam Laboratory. The incident proton energy was 2 MeV, the sample temperature was 360 ºC, and the calculated dpa value at 10 μm (60% of the Bragg peak depth of ~18 μm) was 5 dpa using the quick Kinchin-Pease model. Proton irradiation to this damage level required approximately 125 hours of beam time. Two types of samples were irradiated, tensile specimens and TEM bars. Samples were selected from all regions of the weldment, including the SA508-309L butter interface, the 309L-308L interface, and 308L-304L interface. The stainless steel alloys (304L, 308L, and 309L) within the heat affected zone are characterized by a duplex skeletal morphology of δ-ferrite and γ-austenite resulting from the recrystallization associated with weld fabrication. Approximately 7 to 8 mm of length along the specimen was irradiated. The gauge volume surfaces were mechanically polished and then electro-polished to remove mechanical damage from the mechanical polishing step prior to irradiation. Immersion tests were performed in a recirculating autoclave under BWR NWC conditions (2000 ppb wt. dissolved oxygen, neutral pH, 288 ºC, 10 MPa, and inlet water conductivity <100 nS/cm) to accelerate corrosion. Constant strain rate tests were performed either to failure or to approximately 5% strain. Strain rates of 10^{-7} to 10^{-6} mm/mm/s were used and typical immersion testing required four to six weeks to achieve failure or strains near 5%. Analysis primarily used advanced electron microscopy techniques of FIB lift out specimens.

Extensive as-received (pre-irradiated) and as-irradiated (pre-immersion) microstructure characterization was performed. This relied heavily on electron microscopy and STEM-EDS, but also included neutron diffraction to characterize residual stress in the as-received weldment and atom probe tomography to characterize clustering and precipitation in the as-irradiated (pre-immersion) 308L filler material. The primary observations from this analysis are:

- Residual stress within the as-received weldments was characterized at the top and bottom of the weldment using neutron diffraction. Both base materials (SA508 and 304L) exhibited small compression stress (< 50 MPa), while 308L fusion zone exhibited a complex stress distribution

ranging from 300MPa tensile stress to 200MPa compressive stress. Largest tensile residual stresses and stress gradients were observed within the 309L butter, especially near the fusion boundary with SA508. Such high tensile residual stress could result in high cracking susceptibility of 309L and coincides with observed cracking locations. Partitioning of the residual stress between δ-ferrite and γ-austenite in the duplex microstructure of the 308L and 309L was not possible due to the low volume fraction (~10%) of the δ-ferrite phase. The gauge volume of the neutron diffraction measurements was 24342 cm^3. This small gauge volume was necessary to sufficiently resolve the measured lattice strains, but reduced the sensitivity to the δ-ferrite phase in the duplex structure within 308L and 309L. Further details of this work can be found at https://doi.org/10.1007/s11661-021-06203-x .

- Segregation of Ni and Si to grain and twin boundaries in γ-austenite and as well as the expected Cr depletion were observed in proton irradiated 308L. These observations are consistent with RIS via the inverse Kirkendall effect. Analysis of clustering and precipitation was performed at a depth of 10 and 18 μm in 308L, the former corresponding to 5 dpa and the latter corresponding to the peak of the Bragg curve (~60 dpa). Circular/loopy Ni-Si clusters were observed in γ-ferrite with APT, presumably decorating dislocation loops. Selected area diffraction analysis indicated these clusters did not form a distinct phase. We suspect these clusters are precursors to the γ' phase known to form in irradiated 300 series stainless steels. In addition, intragranular *matrix* G phase formation ($Mn_6Ni_{16}Si_7$) was observed in irradiated δ-ferrite but not in γ-austenite. This was somewhat surprising since δ-ferrite is largely devoid of these elements and irradiation-induced G phase formation is typically observed in austenitic steels. However, proton irradiation induces significant solute transport via radiation enhanced diffusion and density functional theory computations described below demonstrated that the G phase interfacial energy is lowest in the δ phase matrix. Proton irradiation also induced void formation in the γ-austenite, consistent with the known irradiation induce swelling of FCC stainless steels. The void density versus depth scaled with dpa. Segregation of Ni and Si to the void-matrix interfaces was observed. Further details of this work can be found at https://doi.org/10.1016/j.jnucmat.2021.152825 .
- Atom probe tomography was used further characterize the G phase precipitates and Ni-Si clusters in δ-ferrite and γ-austenite, respectively, in proton irradiated 308L. In addition, elemental segregation/depletion at a γ–δ phase boundary was characterized. The APT tip was fabricated from a FIB lift out at the free surface. This region was characterized by approximately 3 dpa. APT analysis confirmed the STEM analysis, including G phase precipitate composition. The nature of the APT data set allowed us to examine elemental profiles across the γ–δ phase boundary and the G phase-matrix interface. Cr depletion was observed at the γ–δ phase boundary. Elemental profiles of the Ni-Si clusters were studied. Some cluster morphologies suggested the segregating elements were decorating dislocation loops. Unfortunately, we could not perform a FIB lift out for APT analysis that included a γ–γ grain boundary. We determined the G phase particle size distribution and volume fraction at the free surface with APT and compared to distributions at depths of 10 μm and 18 μm from STEM analysis. The volume fraction of the G phase at the free surface and at a depth of 18 μm was similar (~0.05) and exceeded that at 10 μm (~0.001) by a factor of 50. The G phase volume fraction at 10 and 18 μm scaled with dpa. The large volume fraction at the free surface could be due to the free surface acting as a point defect sink. The flux of irradiation induced point defects to the free surface could lead to enhanced precipitation.
- The microstructural changes induced by proton irradiation of the 309L butter varied as a function of distance from the SA508-309L interface. The as-received microstructure consisted of a 20–

30μm thick martensitic layer containing Cr-rich carbide precipitates that formed at the SA508 interface. A much thicker 1–4 mm single γ austenite dilution zone, likely caused by carbon diffusion (a γ stabilizer) from the SA508, extended from this martensitic layer to the 309L γ–δ duplex region, which then connected to the 308L groove filler. Proton irradiation induced the most significant changes in the 309L duplex region. Intergranular $Cr_{23}C_6$ intergranular precipitates formed at the δ–γ phase boundaries and grew into the δ ferrite particles. The $Cr_{23}C_6$ carbide precipitates are implicated in SCC of the 309L in this work. We note that $Cr_{23}C_6$ precipitation was *not* observed in proton irradiated 308L or in unirradiated 309L. The other important distinction of proton irradiated 309L was the lack of matrix G phase precipitation and Ni-Si clustering. It is difficult to attribute this observation to differences in composition of 309L versus 308L and at the time of this writing we do not have an explanation.

- In addition to intergranular $Cr_{23}C_6$ precipitation, RIS was observed in the proton irradiated 309L butter. Chromium depletion and Ni segregation were observed at γ–γ grain boundaries that intersected the free surface. The free surface had a damage level of approximately 3 dpa. Chromium depletion was also observed at the free surface, as was a Cr-rich oxide. The latter is presumed to be Cr_2O_3 and may be the native oxide. The Cr depletion observed at the free surface is thought to be a combination of RIS and the denuded zone associated with chromia formation.

The computational component of the work scope included density functional theory simulations associated with grain boundary strength, with the G phase-matrix interfacial energetics, including magnetic effects, radiation-induced segregation (RIS) using kinetic rate theory, and the development of intergranular facture models (XFEM-based CZM capability) in the INL MOOSE-Grizzly code. The primary deliverables from the computational effort are:

- To understand why G phase ($Mn_6Ni_{16}Si_7$) formation was only observed in BCC δ-ferrite but not in FCC γ-austenite in our irradiated 308L material, DFT computations of the interfacial energetics of G phase particles embedded in δ-BCC, α-BCC, and γ-FCC Fe lattices were performed. Non-magnetic, ferromagnetic, and paramagnetic phases were studied. For the three Fe phases in the equilibrium phase diagram, the DFT results show that the G/Fe interface energy is in the following order: δ/G (0.35 J/m^2) < α/G (0.68 J/m^2) < γ/G (1.25 J/m^2). Therefore, it is energetically favorable to form the G-phase in the δ-Fe matrix rather than in γ-Fe when the two phases coexist, such as in the 308L studied in this work. Further details of this work can be found at https://doi.org/10.1016/j.jnucmat.2021.152825 .
- Kinetic rate theory based on the inverse Kirkendall effect was used to predict elemental segregation/depletion to sinks via RIS, specifically grain boundaries, in binary (Ni-Cr) and ternary (Fe-Cr-Ni) alloys. The simulations of the ternary system agreed very well with the measured segregation of Ni and depletion of Fe and Cr at γ–γ grain boundaries in proton-irradiated 308L observed with STEM-EDS.
- To demonstrate the XFEM-based CZM capability, a simple square domain with a pre-defined horizontal interface at the center of the domain was modeled, both using the interface-based and XFEM-based CZM capabilities in MOOSE. This modeling had dimensions somewhat representative of those seen in a grain-scale model, with edge lengths of 8 μm. The bulk material had a Young's modulus of 170 GPa and Poisson's ratio of 0.3. A CZM with linear softening behavior was used. The penalty stiffness of this CZM is 2e6 MPa/μm, which is sufficiently high relative to the stiffness of the bulk material to have a minimal effect on the system response. The strength of the interface was 400 MPa, and the fracture energy was 10 J/m^2. The material was

modeled in 2D with plane-strain assumptions. The interface-based CZM model uses an irregular triangular mesh that conforms to the horizontal interface passing through the middle of the model. The XFEM CZM model uses a quadrilateral mesh with an element size equivalent to the interface-based CZM model. This mesh is intentionally distorted to illustrate how XFEM is able to represent arbitrary discontinuities through the elements. Comparison of the new XFEM-based model with the interface-based CZM model for grain boundary fracture demonstrated very good agreement for this bicrystal geometry.

- To understand how the grain boundary (GB) oxidation impacts the GB strength in Ni-based and Fe-based alloys, atomistic modeling such as DFT was used to calculate the reduction of GB strength due to the oxidation. For Ni, fully oxidized (NiO) GBs, partially oxidized GBs, and metal/oxide interface were studied. For studying the GB character effects, three different types of GBs ($\Sigma3(111)$, $\Sigma3(112)$, $\Sigma5(210)$) were studied. For partially oxidized GBs, we found that the GB strength decreases with increasing oxygen concentration at these boundaries, for both interstitial and substitutional oxygen. The substitutional oxygen causes a stronger embrittlement effect than the interstitial oxygen, except at the $\Sigma3(111)$ GB. For the fully oxidized GBs, the GB strengths of $\Sigma3(112)$, $\Sigma5(210)$ are much lower than their metallic counterparts, except for the $\Sigma3(111)$ GB. The NiO/Ni metal-oxide interface is found to be very weak, indicating the metal-oxide interface could be favorable for crack initiation. For FCC Fe, a high-angle GB ($\Sigma5(210)$) was mainly focused. Similar to the Ni GB, we also found that the GB strength of the partially oxidized GB decreases with the increasing oxygen concentration at the GB.
- To study the SCC-induced intergranular fracture in polycrystalline Ni-based and Fe-based alloys, the finite-element-method (FEM) based cohesive zone model (CZM) that is based on the bilinear mixed mode traction separation law in the MOOSE framework (which is accessible by Grizzly) was used for modeling the SCC-induced intergranular fracture under a tensile load at the microstructural length scale. The Voronoi tessellation method was used to generate 20 grains in the simulation domain. To capture the oxidation-effect on the GB strength reduction, some GBs were set as weak/oxidized GBs. Informed by our DFT results mentioned above, the weak/oxidized GB strength was set to half of that for the pristine GBs for simplicity. In our modeling, different weak/oxidized paths were used, including both percolated and discontinuous paths. Overall, we found that the fracture prefers to occur at weak/oxidized GBs with orientations perpendicular to the loading direction. However, we also found that the fracture may not always occur along the weak/oxidized GBs. In some circumstances, fracture can occur at weak/oxidized GBs that are parallel to the loading direction through a shear sliding mechanism. In addition, some strong (pristine) GBs near triple junctions also can fracture. Regardless, the presence of weak (oxidized) GBs can facilitate the fracture initiation and propagation, as evident by the drop of fracture stress (sometimes can be 50%). We also found that the drop of fracture stress depends on the distribution of weak paths: percolated weak paths lead to a larger drop while discontinuous weak paths result in a smaller drop. Our results demonstrate that the reduction in GB strength due to oxidation is not the only factor that determines the fracture path. The fracture propagation is the interplay of the loading direction, GB strength, distribution of weak GBs, and interactions between neighboring grains.

Immersion tests were performed to expose specimens to BWR NWC (2000 ppb wt. DO, <100 nS/cm water conductivity, 288 ºC, and 10 MPa). Normal water chemistry was used to accelerate corrosion via high dissolved oxygen. Constant extension rate tests (CERTs) were performed at strain rates of 10^{-7} to 10^{-6} mm/mm/s. Tests typically took one to six weeks. Some specimens were pulled to failure. Both proton

irradiated specimens and unirradiated specimens were tested. Unirradiated specimens pulled to failure fractured in a manner suggesting SCC (based on facture surface topological analysis using optical microscopy) near the SA508-309L interface. We also examined the unirradiated regions of proton irradiated tensile specimens after immersion CERTs. Cracking was always confined to the irradiated region and never observed in the unirradiated regions of any specimen. Further, analysis of the fracture surface indicated an initial brittle crack propagation through the irradiated depth, followed ductile crack propagation behavior. The depth of the initially brittle cracking was confined to a depth of approximately 20 μm, consistent with damage depth of the proton irradiation.

Identification and analysis of cracking was complicated by extensive spinel formation on the wetted surfaces of the stainless steel alloys. This is a common issue for immersion testing of stainless steel alloys in autoclaves and chemical washing has been employed by others. Unfortunately, we found that these same chemical washes attacked the δ–γ phase boundaries of the duplex microstructure associated with recrystallization of the 308L and 309L weldment material. Other chemical washes were tried without success. We have reason to suspect the δ–γ phase boundaries played an important role in IASCC (see below). The attack by the chemical wash prohibited us from distinguishing cracking at the surface associated with IASCC from that associated with etching by the chemical wash. Attempts to use a mechanically polish routine were not successful. We therefore resorted to CERTs to failure, which led to extensive (and visible with optical microscopy) cracking in the 309L butter in the proton irradiated regions. This is consistent with the large tensile strains within the 309L quantified with neutron diffraction. We then performed FIB lift outs to study the local chemistry. The primary observations from the immersion testing are:

- A Cortest recirculating loop autoclave with a 50 kN load frame dedicated to the study of SCC was installed in July of 2018 and commissioned in September of 2018. Commissioning involved a series of immersion tests of unirradiated weldment tensile specimens in BWR NWC (290 °C, 2000 ppb wt. DO, <100 nS/cm, and 10 MPa) hot water under strain rates of order of 10^{-7} mm/mm/s. The effect of strain rate and DO was investigated. The largest DO (4000 ppb wt.) and slowest strain rate (7e-8 mm/mm/s) resulted in failure at yield (0.6%) that was attributed to SCC. The same strain rate with 2000 ppb wt. DO resulted in failure at a total strain of approximately 2% and is likely due to SCC as well. Dissolved oxygen level at a strain rate of 2e-7 mm/mm/s has no effect on failure; 2200 ppb wt. DO versus zero DO both failed at approximately 7%. Failure in the unirradiated weldment material always occurred at the SA508-309L butter interface and may be associated with the martensitic layer at this interface, the 309L dilution zone between the SA508 and the 309L butter, or the 309L butter duplex region.
- IASSC in BWR NWC conditions was investigated with proton irradiated tensile specimens. Failure in the irradiated tensile specimens occurred in the 309L butter. Extensive cracking was also confined to the 309L butter. Both observations indicate the large tensile residual stress and stress gradients present in the butter are contributing factors. Failure and cracking was only observed in the irradiated portion of the tensile specimens. We interpret this as direct evidence of irradiation-assisted cracking. SEM images of the failure surface showed brittle failure within 20 μm of the free surface, corresponding to the maximum proton range and associated dpa damage. Ductile failure was observed beyond that depth, characterized by a dimpled fracture surface.
- Cracking in the proton irradiated area of 309L initiated at γ–γ grain boundaries and δ–γ phase boundaries that intersected the free surface. We attribute this cracking to IASCC since crack initiation occurred at γ–γ grain boundaries and γ–δ phase boundaries where Cr depletion due to RIS

was observed. Oxide corrosion products were seen on the surfaces of these cracks, which is expected for cracks that initiate at the free surface during immersion testing. Cr depletion in 309L was quantified with STEM EDS at γ–γ grain boundaries and γ–δ phase boundaries within the specimen interior (but still within the proton irradiated depth of ~20 μm) and at the surface.

- A second type of cracking was associated with proton irradiated δ–γ phase boundaries below the free surface within the irradiated volume. $Cr_{23}C_6$ precipitates were observed at δ–γ phase boundaries in proton irradiated 309L with the duplex microstructure. The SAD pattern from these precipitates shows these particles have a commensurate interface with γ austenite and are $Cr_{23}C_6$. Our STEM analysis of this type of cracking appear to show initiation at δ–γ phase boundaries in the vicinity of the $Cr_{23}C_6$ precipitates. These cracks are thought to be a combination of residual tensile stress, applied tensile stress, and embrittlement. The embrittlement is likely a combination of dislocation loop formation and $Cr_{23}C_6$ precipitation. Corrosion products (oxides) were not observed on the surfaces of this crack type when confined to the irradiated bulk and not exposed to the BWR NWC hot water. However, some cracks grew under the applied tensile load and reached the free surface. Oxide corrosion products were then observed on the surfaces of these cracks. We do not attribute this cracking mechanism to SCC since corrosive attack did not occur. However, it is irradiation-assistant cracking since proton irradiation induced $Cr_{23}C_6$ precipitation. Embrittlement associated with dislocation loop formation was also a contributing factor although this was not characterized in this work. We are currently preparing manuscript for our observations associated with cracking under tensile stress in BWR NWC hot water.

Cracking under applied tensile load in BWR NWC conditions is observed to occur in the duplex region of the 309L butter of the SA508-304L weldment. Our work identifies several factors that influence cracking:

- The γ–δ phase boundary interfaces associated with the duplex microstructure of recrystallized 309L butter.
- Large residual tensile stress at the SA508-309L butter interface that is exacerbated by applied tensile load.
- Radiation-induced depletion of Cr at γ–γ grain boundaries and δ–γ phase boundaries intersecting the free surface that makes these interfaces susceptible to corrosive attack.
- $Cr_{23}C_6$ precipitation at γ–δ phase boundaries that may embrittle the region near these phase boundaries, serve as stress risers, or contribute to the overall lattice strain under applied load and large residual stress.
- While dislocation loop formation was not quantified it must have occurred during proton irradiation and the associated embrittlement would affect the response under applied tensile load and lead to IASCC.

The balance of this document is divided into the following sections:

1. Introduction and Background
2. Experimental methods, initial characterization of the as-received material including residual stress measurements using neutron diffraction, proton irradiation procedures, autoclave immersion testing, and microanalytical analysis procedures.
3. Experimental findings related to the as-irradiated specimens and the post-immersion evidence of SCC, IASCC, and irradiation-assisted cracking. These findings will include TEM, STEM-EDS, and APT.
4. Computational methods and results, including a comparison of elemental segregation and depletion at γ–γ grain boundaries resulting from RIS and the inverse Kirkendall effect using kinetic rate theory, DFT simulations of G phase interfacial energies, and the development of XFEM-based CZM capability.
5. Publications, technical presentations, acknowledgements, and lessons learned.

1. Introduction and Background

Water chemistry controls implemented in LWRs balance the response of high alloy core and piping components, the response of Zr-based cladding and channel boxes, and radiation fields. Hydrogen water chemistry (HWC) was introduced in boiling water reactors (BWRs) in the 1980s and 1990s to mitigate inter-granular SCC (IGSCC) of high alloy steels by reducing the electrochemical corrosion potential. While initial HWC levels led to extended life of out-of-core components, radiolysis-enhanced IGSCC of sensitized core internal components required greater hydrogen addition to the primary coolant, as well as Zn to stabilize CRUD with respect to Co-60 injection by forming a more stable spinel on stainless steel. Pressurized water reactors (PWRs) also use HWC, with Zn and Li injection to balance pH and mitigate cracking of primary side steam generator tubes.

Alloy 308/309 (Fe-Cr-Ni austenitic stainless steels) are widely used for core internals and piping systems in both PWRs and BWRs. While these alloys respond favorably to LWR environmental factors, weldments typically have high residual stress and composition gradients within the heat affected zone (HAZ). In particular, the redistribution of Cr, the element responsible for oxidation/corrosion resistance via chromia formation, can sensitize these alloys to SCC phenomenon. Tensile residual stress can locally exacerbate applied loads and induce crack propagation. When exposed to a chemically reactive environment, such as the water coolant in LWRs, these materials can be preferentially attacked at active paths such as grain and phase boundaries within the HAZ. Since an oxide typically has a lower fracture toughness than a fresh metal, the residual stress can initiate SCC.

IGSCC is closely coupled to grain boundary chemistry; for example, sensitized austenitic stainless steel via $Cr_{23}C_6$ carbide precipitation along grain boundaries, the local Cr concentration at grain boundaries is reduced, facilitating inter-granular corrosion. As a result, the sensitized steel is susceptible to SCC. Displacement cascade damage can further modify the grain boundary chemistry through radiation-induced segregation (RIS). In austenitic stainless steels, the oversized Cr typically becomes depleted from grain boundaries via RIS and SCC is more pronounced under irradiation. Weldments of high Cr-content alloys, such as 308/309 are more prone to SCC in LWR environments due to residual stress and composition gradients. In the US Nuclear Regulatory Commission Report on Expanded Materials Degradation Assessment (EMDA) [1], the susceptibility scores of these weldments are high in both PWR and BWR environments. Therefore, understanding SCC mechanisms that operate on weldments of these materials in the reactor-relevant environment is important for life extension. In addition, development of a predictive modeling capability, will allow the U.S. nuclear industry to be better informed of potential component failures. This knowledge is therefore important for the U.S. nuclear industry and the U.S. NRC to make appropriate decisions on the long-term safe operation of reactions.

2. Experimental Methods

Weldment Fabrication, Initial Weldment Microstructure Characterization, and FIB Sample Preparation

The SA508-304L weldment was fabricated by Electric Power Research Institute and is shown in Figure 1 [2]. The SA508 plate was 32 mm thick, while the 304L plate was 25 mm thick. The total cross sectional area of the weldment was approximately 1252 inches^2. This weldment was fabricated using the gas tungsten arc welding (GTAW) technique. A total of 54 bead lines of SS 309L butter were deposited in five layers on SA509 with the interpass temperature of 177 °C. The bevel angle was 60 degrees. The current average, voltage average, average travel speed were 215 A, 9.9 V, and 8.1 cm/min, respectively. A post-weld heat treatment (PWHT) was performed on the SA508 plate with 309L butter at 635 °C ± 10 °C for 1.5 hours. The heat-up and cool-down temperature ramp rate was below 70 °C/hr when the temperature was above 220 °C. The butter was then cut to a thickness of 1.5 cm. The 309L butter was welded to the 304L using

308L filler with bevel angle of 60 degrees. The 308L filler weld consisted of a total of 57 bead lines in 18 layers and the interpass temperature was 177 °C. The fit-up root opening was 0.32 cm and the fit-up width at the joint top was 3.2 cm. The current, voltage, and travel speed of the 308L groove weld were 240 A, 10.4 V, and 9.4 cm/min, respectively. A PWHT was not performed for the 308L groove weld, consistent with industry practice. The 308L filler material recrystallizes upon cooling into a mixed phase microstructure of δ ferrite and γ austenite. This microstructure is shown in Figure 2. The 308L-304L heat affected zone (HAZ)/fusion zone is shown in Figure 3. The δ-ferrite volume fraction (~10%) in 308L is consistent with the known Schaeffler diagram (see Figure 1 inset) [3, 4]. The location of the 309L butter used in this study is also close to the 10% A+F line but is not shown.

The δ phase precipitates into a skeletal microstructure. Cooling rate plays a critical role in the shape and morphology of δ ferrite in 308L filler. The microstructure of δ ferrite can have cellular structure, skeletal shape, and/or lathy morphology depending on the cooling rate [5]. A fast cooling rate yields a cellular structure of δ ferrite and a slow cooling rate leads to a skeletal morphology of δ ferrite. The cooling rate used for our weldment was below 70 °C/h, which is slow enough to generate skeletal δ ferrite; this morphology is observed here (Figure 2a). The composition of the weldment materials is given in Table 1.

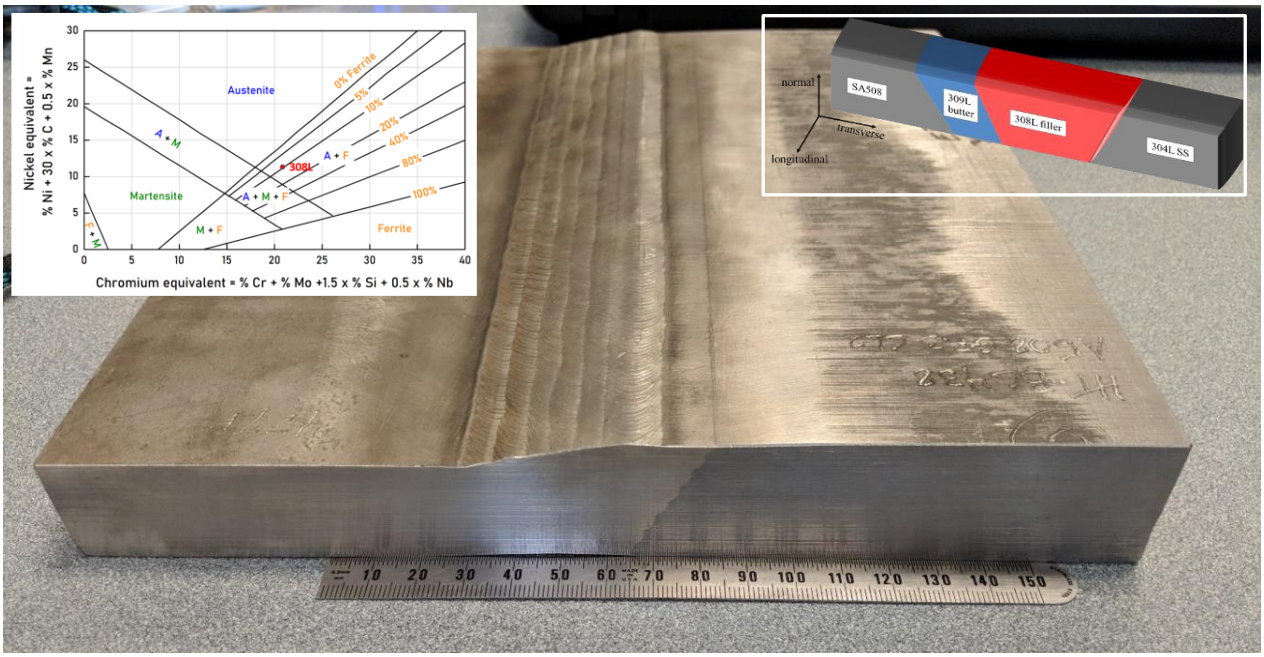

Figure 1. The SA508-304L weldment fabricated by EPRI used for this study. The SA508 on the right is thicker and the serrated interface between this material and the 309L butter is observable on the side of the weldment. This is one edge of the 309L dilution zone. Left inset: The Schaeffler diagram showing the location of the 308L filler. Right inset: Schematic illustration of the weldment showing the normal (N), longitudinal (L), and transverse (T) directions. The transverse direction is orthogonal to the weld (L) direction.

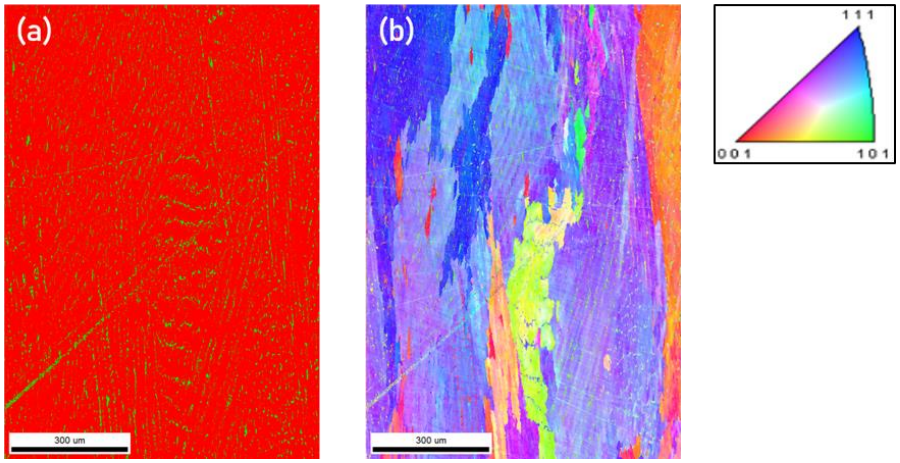

Figure 2. (a) EBSD phase map of the 308L filler weld joint, with the γ matrix rendered as red and the δ phase as blue, (b) Inverse pole orientation map of 308L filler weld joint.

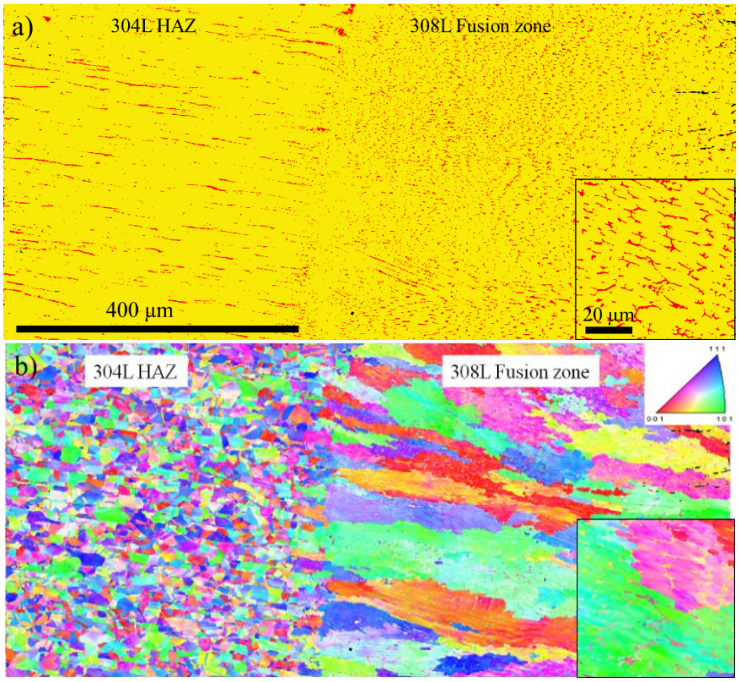

Figure 1. (a) EBSD phase map of austenitic matrix (yellow) and δ-ferritic precipitates (red), and (b) Inverse pole orientation map across the 304L-308L fusion boundary, with the inset of the larger magnification images from the 308L fusion zone. The presence of δ ferrite in rolled 304L plate (left portion of Figure 3a) is not unexpected [B. Sutton, EPRI, private communication].

Table 1. Specifications of SA508-304L DMW provided by EPRI.

Materials (at.%)	Cr	Ni	Mn	Mo	C	Cu	N	P	Si	Fe
SA508	0.18	0.76	1.38	0.47	1.01	0.08	NA	0.02	0.45	95.64
309L	24.38	12.80	1.60	0.04	0.05	0.09	NA	0.04	0.93	60.08
308L	21.07	9.69	1.99	0.09	0.07	0.24	NA	0.04	1.02	65.78
304L	19.23	7.53	1.73	0.19	0.09	0.38	0.27	0.05	0.55	69.96

The 309L butter exhibits two distinct microstructure morphologies; a non-uniform dilution zone with the width of approximately 1–4 mm adjacent to the fusion boundary of SA508-309L and a duplex zone away from the fusion boundary, as shown in the Figure 4a, with the inset showing the morphology of the duplex zone in 309L. The duplex zone of 309L has similar skeletal δ-ferrite morphology as 308L. The dilution zone is characterized by a single austenitic phase. Composition profiles across the different zones are shown in Figure 4c with reduced Cr and Ni composition in the dilution zone compared to the duplex zone. However, the absence of the ferrite phase in the dilute zone cannot simply attributed to the 3% Cr (as a ferrite-promoting element) reduction according to the WRC-1992 diagram [4]. We believed that carbon (as an austenite-promoting element) diffusion from the SA508 into the 309L butter could also contribute to the absence of δ-ferrite precipitates at the dilution zone. However, the carbon composition was not measured due to the low composition and the low sensitivity in the EDS measurement. An enlarge image at the fusion boundary is shown in Figure 4b, where a narrow martensitic zone with an irregular boundary is observed with the width of ~20 – 30 μm.

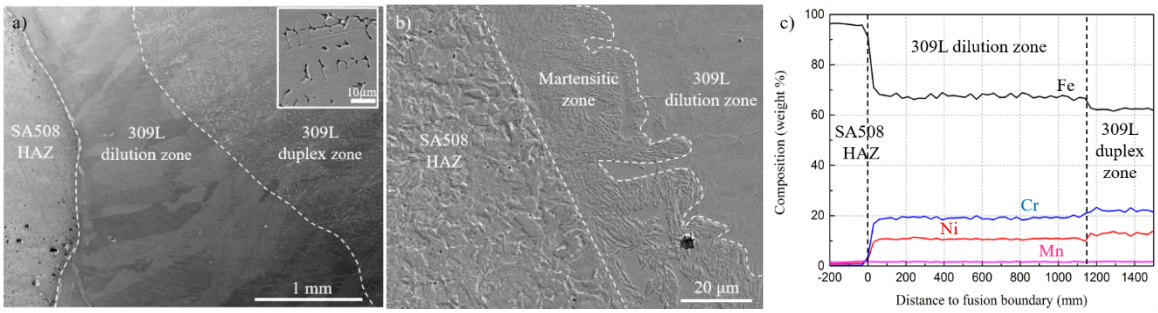

Figure 2. Microstructure of the fusion boundary of SA508-309L. (a) 309L demonstrates two morphologies (dilution zone and duplex zone) with the composition profiles shown in (c) and the inset showing the 309L duplex zone, (b) martensitic zone at the fusion boundary. The x axis label in (c) should be μm.

The complex structure of the martensitic zone at the SA508-309L fusion boundary is shown in Figure 5. Figures 5a-b show the phase distribution and the inverse pole figure (IPF) of the region near the fusion boundary. The interface of the martensite zone and the SA508 HAZ is not obvious from the IPF image. However, the width of the martensitic layer is approximately 20 – 30μm from SEM analysis (Figure 4). The grain morphology in proximity of the fusion boundary is complex and consists of refined grains, as shown in the IPF map in Figure 5b. Smaller grains size of irregular shape are present within 25 μm of the fusion boundary, which likely corresponds to the martensitic zone. Figures 5c-d show the STEM dark file image and the combined Cr/Ni maps at the fusion boundary, where the boundary was outlined. Cr-rich carbide precipitates with high number density were observed at the martensitic zone, which have an average size and a number density of 44.1 ± 16.9 nm and 1.5×10^{21} m^{-3} in proximity to the fusion boundary. Such high number density corresponds to a volume fraction of ~10%. In addition, Ni-rich regions were observed, as shown in Figure 5d. In contrast, no Ni- or Cr-rich precipitates were observed in the 309L dilution zone.

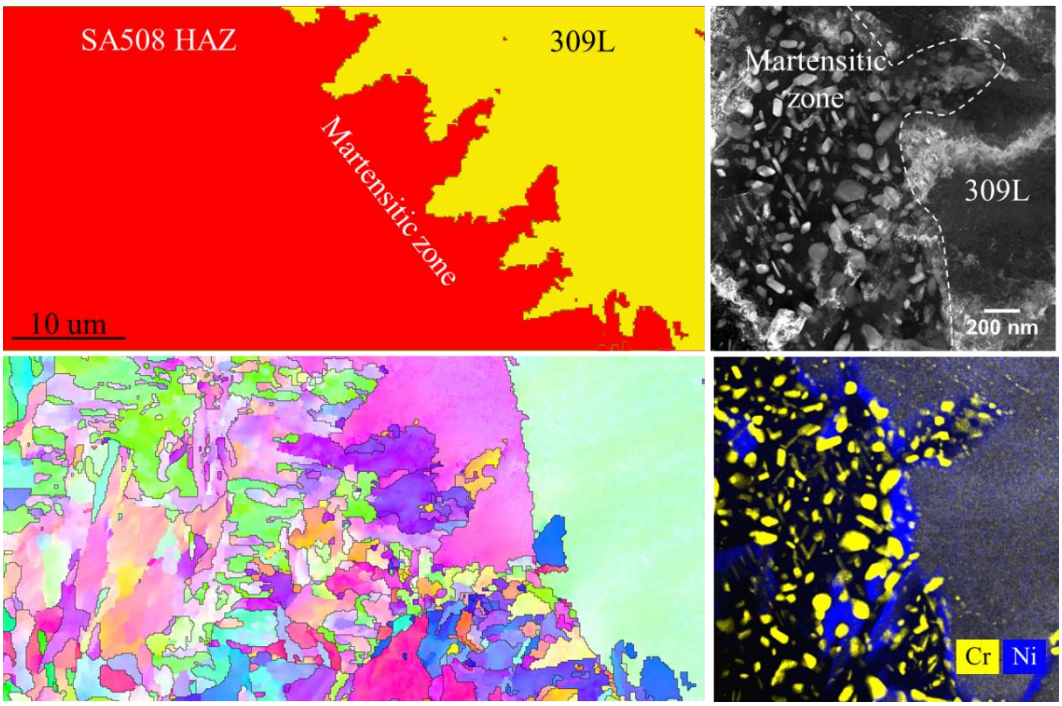

Figure 5. (a) Phase distribution of 309L (yellow) and SA508 HAZ (red), and (b) Inverse pole figure of the region near fusion boundary. (c) TEM dark field image and d) combined maps of Cr (yellow) and Ni (blue) at the fusion boundary of SA508-309L.

Figure 6 shows the Vickers hardness profile across the weldment. Vickers hardness measurements were performed at the SA508 and 304L base materials, with the hardness of 245.1 ± 5.4 HV1 and 190.9 ± 3.6 HV1 for the SA508 and 304L, respectively. Thermal cycling associated with the welding process increases the hardness of the HAZ of both ends, and the width of HAZ are 4 mm and 16 mm for SA 508 and 304L respectively. At the SA508 HAZ, a maximum hardness (319.0 ± 2.5 HV1) was observed at about 1.2 mm from the fusion boundary, and the hardness decreases toward the fusion boundary. We believe carbon diffusion from SA508 to 309L leads to carbon enrichment at 309L and thus the formation of a dilution zone. Such diffusion also leads to carbon depletion at SA508 HAZ near fusion boundary, which could contribute to reduce the hardness near the fusion boundary.

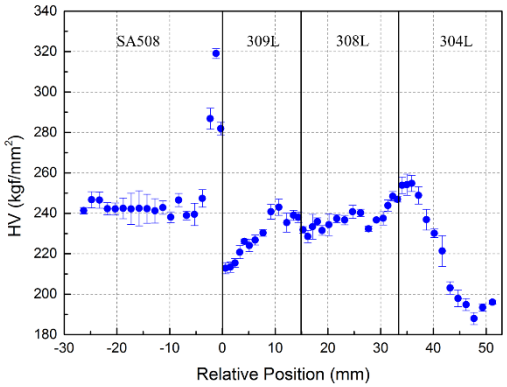

Figure 6. Vickers hardness across the weldment, showing that the widths of HAZ are 4mm and 16mm for SA508 and 304L respectively.

The residual stress across the weldment at top and bottom layers are shown in Figure 7. Residual stress in the base SA508 and 304L are uniformly small in three directions (mostly ≤ 50MPa in compression), while the residual stresses are complex within the weldment. The 308L fusion zone shows variations of residual stress ranging from 300MPa tensile stress to 200MPa compressive stress. Large gradients of residual stress are present in 309L, especially near the fusion boundary (up to ~750MPa in tension), while SA508 shows up to ~200MPa in compression in longitudinal and normal directions near the fusion boundary. Such high tensile residual stress at the 309L likely leads to high cracking, consistent with our observations presented in Section 2.

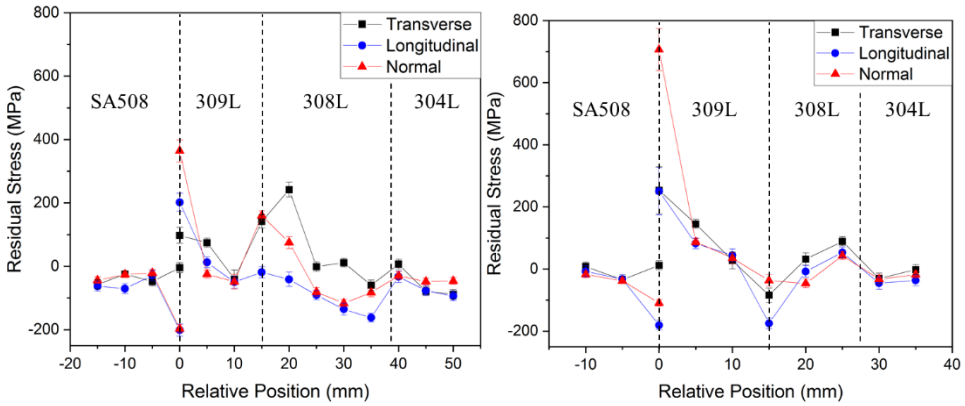

Figure 3. Residual stress across the weldment at the a) top layer, and b) bottom layer. Large tensile stress (up to 750MPa) is present at 309L while compressive stress (up to 200MPa) is present at SA508 near the fusion boundary of SA508-309L. Refer to the Figure-1 inset for identification of the T, L, and N directions.

Samples for proton irradiation where cut from the weldment using electrical discharge machining to avoid significant surface damage. The samples were mechanically polished and then electropolished to remove the damage layer from mechanical polishing. Electropolishing was done with a 90-10 methanol-perchloric electrolytic solution at -30 ºC. A potential of 40 V was applied between the electrolyte and the 308L specimen for 15 s. Figure 8a shows a slice of the weldment with tensile bars and TEM specimens removed. Figure 8b shows these samples mounted onto the proton irradiation sample stage (see the next section for proton irradiaton details).

Figure 8. (a) Location of tensile bars and TEM specimens from a slice of the SAS508-304L weldment and (b) tensile bars and TEM specimens mounted onto the ion accelerator sample stage.

Focused ion beam (FIB) lift outs were used to study various aspects of the microstructure with electron-based microanalytical analysis techniques. Thermo Scios2 Dual-Beam SEM/FIB was used to acquire SEM images and preparing lift-out TEM specimens. TEM specimens with a dimension of 10 µm by 10 µm were thinned with a Ga ion milling to less than 100 nm, which is a thickness that is transparent to electron beam. Three-dimensional chemical composition was collected from a needle-shaped FIB specimen by using Cameca Local Electrode Atom Probe (LEAP) 5000XS. APT (Atom Probe Tomography) specimens (tips) were fabricated using FIB with Thermo Scios2 SEM. Examples of FIB lift outs are shown in Figure 9. An APT tip before and after ion milling shown in Figure 10.

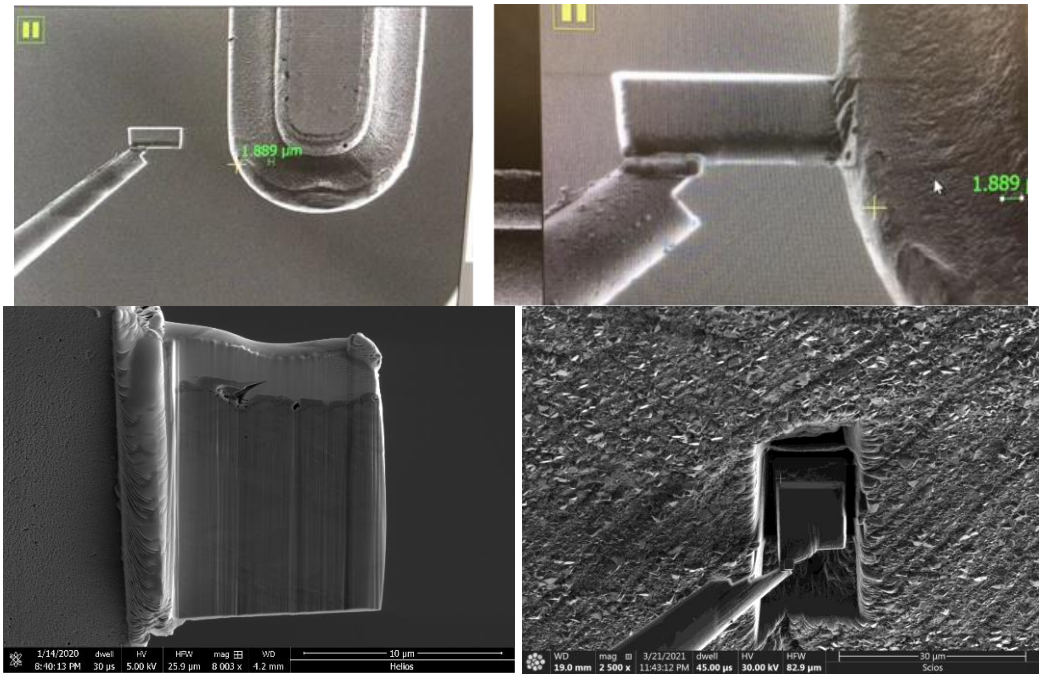

Figure 9. Clockwise from upper left: Lift out prior to joining to TEM grid; Joining of lift out to TEM grid; Trench and a second lift out; Lift out joined to TEM grid.

Figure 10. (left) FIB lift out mounted to a post prior to final ion milling to create an APT tip. (right) SEM image of the final APT tip after ion milling. The tip is atomically sharp.

Proton Irradiation

Three proton irradiation experiments were completed for the project at the Michigan Ion Beam Laboratory: November 2018, July 2019, and June 2021. Samples from the first irradiation exhibited oxide growth after proton irradiation. This set of samples was in the common vacuum of the accelerator during a SF_6 leakage event and this may have been responsible for the oxide growth. Each irradiation stage included four 2mm-wide stainless steel tensile samples and three 1.5mm TEM bars (denoted as SCC Table 2). Irradiation experiments were performed using the 3MV Pelletron accelerator with 2 MeV protons, a nominal sample temperature of 360 ºC, and an average current of 32 μA. The samples were irradiated to 5 dpa at 360°C with a dose rate of ~1×10^{-5} dpa/s (full cascade), requiring approximately 125 hours of continuous beam time. Indium foil was used for thermal contact between the samples and the sample stage.

Sample temperatures were monitored using a thermal imaging system during the irradiation. The temperature variations were kept within ±10ºC by adjusting the amount of heating and cooling received from a heater and an air-cooling loop. Figure 11a shows a thermal image of the stage during the third proton irradiation and temperature distribution of one of the first TEM bars is shown in Figure 11b. The average temperatures are given in Table 2. The targeted temperature was achieved. Figure 11c shows β-ray counts of the irradiated sample after eight days after the irradiation was completed. Uniformity of irradiation was also achieved based on the β-ray data. The irradiated samples were sent back to UIUC for SCC testing after the sample radioactivity was under the safety limit.

Table 2. Average sample temperatures for the third proton irradiation.

	SCC#1	TEM #1	SCC #2	TEM #2	SCC #3	TEM #3	SCC #4
Avg. T (°C)	359.8	360.3	359.7	359.6	361.1	359.8	360.5
2σ (°C)	69	7.7	8.3	7.0	7.2	9.1	8.6

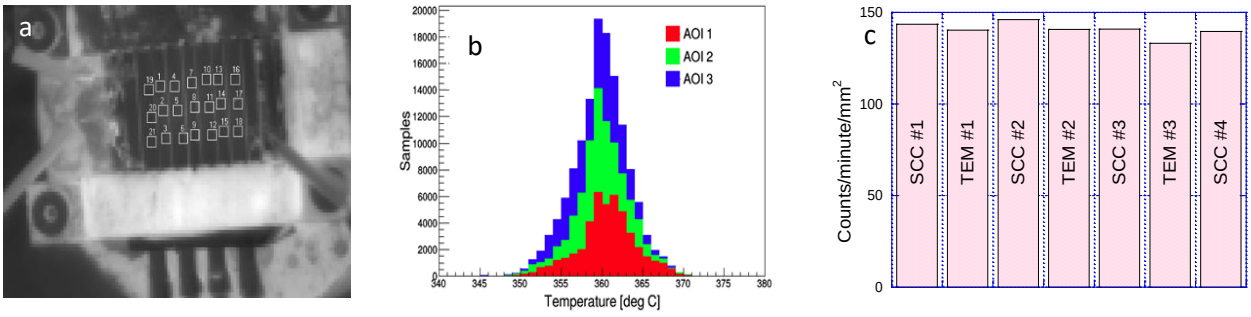

Figure 11. (a) Thermal image of the stage showing temperature measurement locations, (b) temperature distribution of the first TEM bar, and (c) β-ray counts after proton irradiation showing uniformity of irradiation.

The simulated differential energy to recoils for 2 MeV protons in 308L stainless steel using TRIM [6] is shown in Figure 12. The implantation profile follows the energy to recoils and is not shown. The energy to recoils is relatively flat over the first 10 μm. The Bragg peak (effectively the proton range that corresponds to the peak in the energy to recoils) is approximately 18 μm. The displacements per atom (dpa) at 60% of the peak depth (~18 μm) is 5 dpa. The free surface dpa a ~3 dpa, while the peak dpa is ~50 dpa, both assuming dpa scales linearly with the energy to recoils.

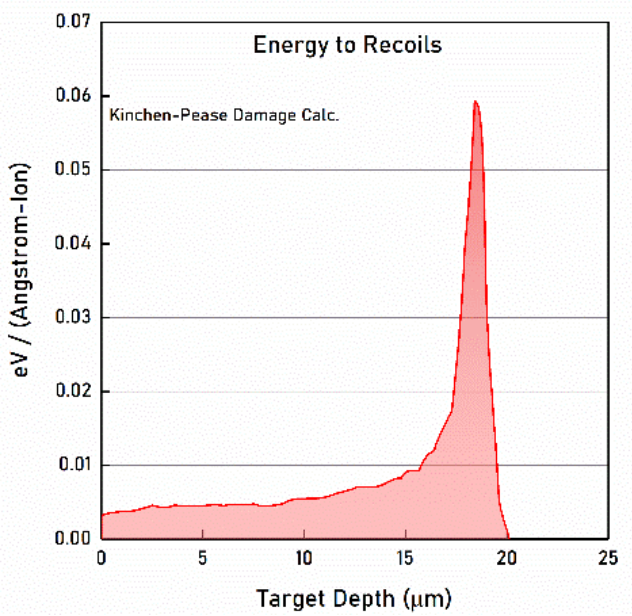

Figure 12. Simulated differential energy to recoils using the quick Kinchen-Pease model in TRIM for 2 MeV protons in 308L stainless steel.

Autoclave Immersion Testing

A recirculating loop autoclave with a 50 kN load frame was used to expose tensile bars and TEM specimens to simulated BWR NWC conditions is immersion tests. This autoclave is show in Figure 13 and had supply and return pH, dissolved oxygen, and water conductivity gauges (collectively called water analytics). Preheaters introduced hot water into the Inconel pressure vessel. The pressure vessel is rated at 600 °C and 30 MPa, maximum flow rate of 6 L/hr. The load frame is capable of 10^{-8} to 450^{-4} mm/mm/s strain rate range, has dual LVTD strain gauges, strain and load accuracies of 0.5 and 0.2%, respectively, and has a 10,000 lb. load cell. The water column has a gas sparging inlet to control dissolved oxygen by sparging, Ar, Ar+O_2, and H_2 gases. The graphical user interfaces (GUIs) shown in Figure 14 allowed control of the load frame and showed real time water analytics information and overall loop flow information. This autoclave was procured with NEUP GSI funds from the 2017 competition and coincided with the initiation of this contract.

Boiling water reactor normal water chemistry was used for the immersion testing. The typical BWR NWC conditions were: 288 ºC, 10 MPa, 2000 ppb wt. DO, neutral pH, and <100 nS/cm conductivity. The dissolved oxygen level was controlled by continuously sparging a mixture of Ar plus 5% O_2 gas in the water column. The conductivity of the water was controlled by continuously filtering with a de-ionizing cartridge. The water temperature in the pressure vessel was controlled to ±0.1 ºC. Strain rates between 10^{-7} and 10^{-5} mm/mm/s were used. Stress as a function of strain was acquired, as was load versus time and strain versus time. Immersion tests typically ran for one to five weeks.

Figure 13. Left to Right: Tensile specimen (not a SCC tensile bar) mounted on the autoclave load frame grips; load frame strain gauges and load cell below the autoclave pressure vessel; autoclave loop hardware and preheaters (foreground); front of the loop stand with the water column, showing water flow control valves, high pressure pump, high pressure control valve (blue), and water analytics.

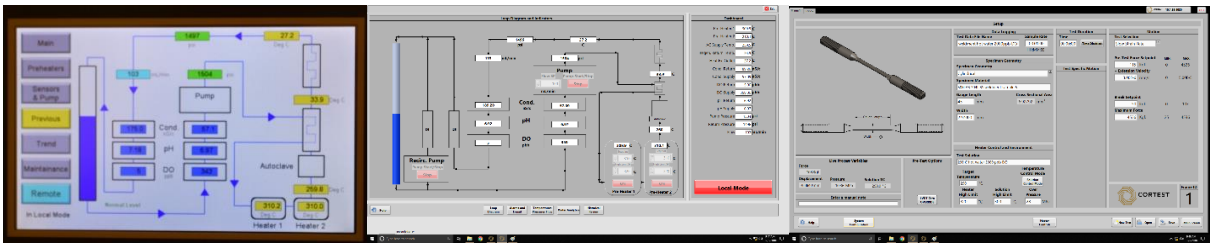

Figure 14. Left to Right: GUI of loop stand overview; GUI of water analytics overview; GUI of load frame overview.

Microanalytical Analysis Techniques

Scanning transmission electron microscopy (STEM), transmission electron microscopy (TEM), scanning electron microscopy (SEM), electron dispersive spectroscopy (EDS), selected area diffraction (SAD) analysis, neutron diffraction, and atom probe tomography (APT) were all used to study the as-received, post-irradiated, and post-immersion tested sample materials. Focused ion beam (FIB) methods were used to perform lift out specimens for the electron-based analysis techniques and for APT analysis, as described above. All electron-based analysis, APT analysis, and FIB sample preparation was performed at the UIUC MRL. The neutron diffraction measurements were performed on the VULCAN instrument at the Spallation Neutron Source at ORNL.

STEM-EDS were performed on Thermo Scios2 TEM lift out specimens with FEI Themis Z Advanced Probe Aberration Corrected Analytical TEM/STEM at 300 k with a 4-crystal EDS detection system. FEI Themis Z Advanced Probe Aberration Corrected Analytical TEM/STEM was used for obtaining high-angle annular dark-field (HAADF) and atomic resolution STEM micrographs as well.

Three-dimensional chemical composition was collected from a needle-shaped specimen by using Cameca Local Electrode Atom Probe (LEAP) 5000XS. APT tip specimens were fibbed out with Thermo Scios2 SEM; an example was shown above. The diameter of the bottom of the APT tips were around 350 nm. Typically, between 80 and 100M atoms were counted. The IVAS software package was used to analyze the APT data.

Electron backscatter diffraction (EBSD) analysis presented above was performed with Thermo Scios2 Dual-Beam SEM/FIB, which has a Hikari Super EBSD detector. The EBSD analysis was performed using the Analysis OIM (orientation imaging microscopy) software for phase distribution, inverse pole figure (IPF), grain boundary character, and kernel average mis-orientation (KAM). Specimens for EBSD were mechanically polished with 4000 grit SiC and then vibration polished using 0.05 μm Al_2O_3 solution. An EBSD step size of 1 μm was used to have a global picture of the microstructure of 308L filler. In addition, Thermo Scios2 Dual-Beam SEM/FIB was used to acquire SEM images and preparing lift-out TEM specimens.

Neutron diffraction was used to characterize the residual stresses of the DMW using the VULCAN engineering materials diffractometer at the Spallation Neutron Source (SNS) at Oak Ridge National Laboratory [7]. These measurements were described above as part of the characterization of the as-received material. The SNS is a pulsed neutron source and all neutron detection events are recorded as discrete events in both time (energy) and scattering angle. The time-of-flight VULCAN diffractometer enables measuring lattice strain in multiphase materials simultaneously. Two detector banks define two wavevector transfer directions, Q1 and Q2 which allow lattice strains to be simultaneously measured in two directions. A 90° rotation of the sample about the transverse direction is required to measure the lattice spacing in the third direction for the residual stress calculation. A nominal $2\times3\times2$ mm^3 neutron gauge volume was used for the all the measurements. The lattice spacing of specific (hkl) lattice planes was determined by fitting the diffraction neutron spectra using VULCAN Data Reduction and Interactive Visualization (VDRIVE) software. A reference comb sample was used for the strain free d_o measurements.

3. Experimental Findings Related to Post-Irradiated and Post-Immersion Testing

Autoclave Commissioning, SCC of SAS508-304L Weldment Material

Commissioning of the autoclave involved stress-strain measurements of *unirradiated* tensile specimens taken from the as-received SA508-304L weldment orthogonal to the weld direction (the transverse direction in the Figure-1 inset) under different dissolved oxygen values and two different strain rates. These data are shown in Figure 15, which includes an open air test. The open-air sample was not pulled to failure. The stress-strain curves do not begin at the origin because of the initial force on the load cell associated with the water pressure (10 MPa). This results in an initial stress of approximately 150 MPa. The initial stress value is dependent on the gauge cross sectional area.

The Figure-15 data demonstrate that strain rate and DO have an effect on failure. Failure was always observed at the SA508-309L butter interface and may be coupled to the large residual stresses in this region (Figure 7) and/or the martensitic layer (Figures 4 and 5). Sample 5 was exposed to the most severe conditions (slowest strain rate and therefore longer exposure times, and highest DO, in excess of BWR-NWC DO conditions) and failed at yield. Sample 6 also was exposed to the lowest strain rate and BWR-NWC DO (2000 ppb wt.) and failed at strains much less than the samples 3 and 4. A comparison of samples 4 and 6 (same DO) demonstrates that strain rate has a strong influence on total strain to failure. Likewise, a comparison of samples 5 and 6 (same strain rate) demonstrates that DO has a strong influence on total strain to failure. These data demonstrate SCC, not IASCC since radiation damage was not present. The location of the failure surface, at the SA508-309L butter interface, is not unexpected, given the large residual tensile stress and the presence of the martensitic layer.

The yield point for the open air, ambient temperature test (sample 2, ~480 MPa) is significantly larger than those of stainless steel alloys at ambient temperature (~200 MPa/304L, ~380 MPa/309L, ~415 MPa/308L), but similar to that of SA508. This might seem to be unexpected since the yield point should be determined by the weakest material in the weld, not the strongest. However, the gauge length of the open air sample did not contain 304L. Further, the 308L and 309L were in the recrystallized state with a δ–γ duplex microstructure. This certainly induced significant degree of precipitate hardening.

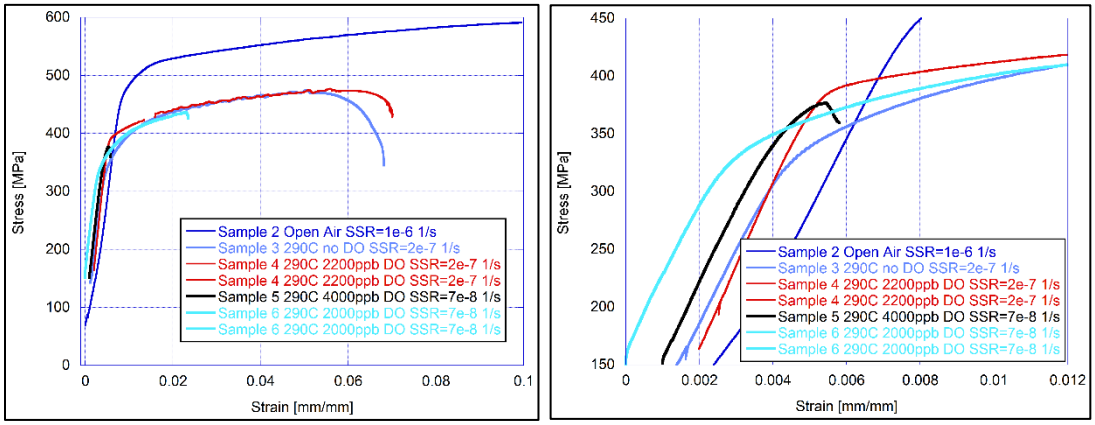

Figure 15. Effect of water chemistry (dissolved oxygen) and strain rate on failure of tensile specimens taken across the unirradiated SA508-304L weldment. The open air sample was not pulled to failure. All samples were unirradiated and in the as-received condition. The right-hand figure is a closer view of the low strain region. The unit of strain rate are mm/mm/s. For reference a total strain of 0.02 mm/mm required 3.3 days of exposure at a strain rate of 7e-8 mm/mm/s.

The expected effect of temperature on yield is also evident in Figure 15; the 290 °C yield point is reduced by approximately 120 MPa compared to the ambient open air temperature measurement.

We performed optical microscopy of the fracture surface of sample 4 and this is shown in Figure 16. This sample was exposed to BWR NWC conditions for approximately four days. Initial failure was associated with surface cracking. These initial crack surfaces were exposed to the autoclave environment and spinel growth is observed. Subsequent crack propagation occurred rapidly and the surface is typical of ductile tearing, similar to that of a K_{IC} measurement surface. We did not attempt to identify the precise location of initial failure (the martensitic layer, for example).

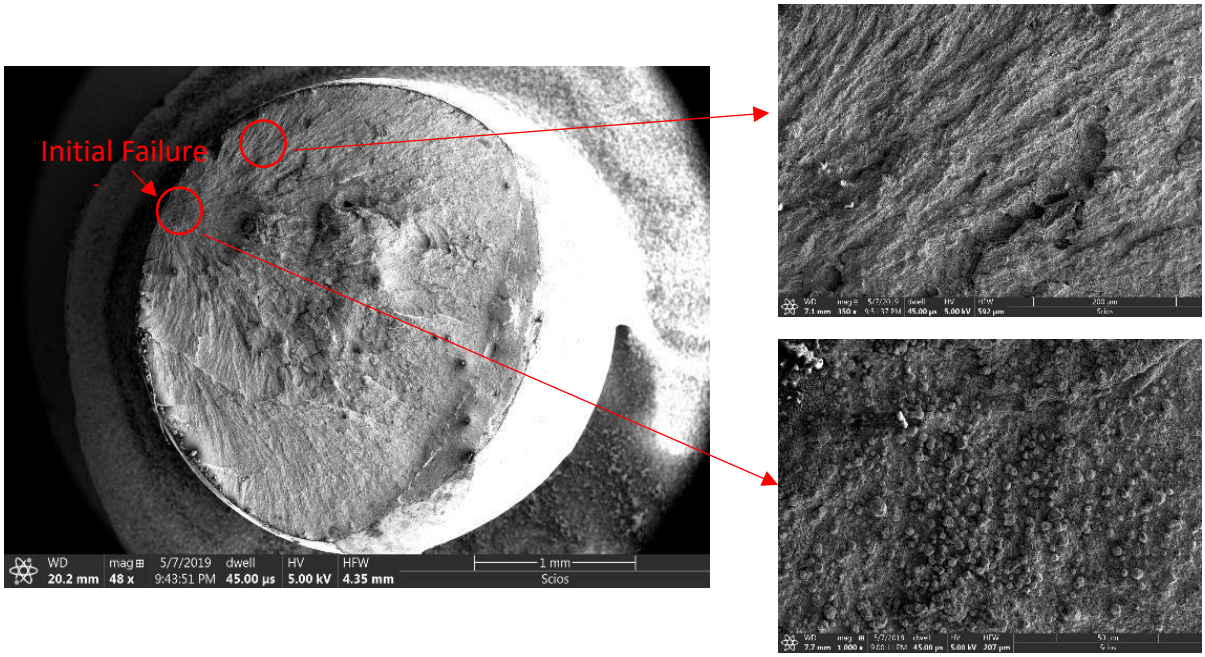

Figure 16. Fracture surface of sample 4 showing the suspected initial failure location. This region is shown at higher magnification at lower right and exhibits spinel formation, indicating this surface was exposed to the autoclave hot water. The majority of the surface (upper right) represents rapid propagation as the sample failed and was not exposed to the autoclave hot water for a significant amount of time.

Microstructure Associated with Proton Irradiation of 308L Groove Filler Material

The microstructural changes induced by proton irradiation in 308L were investigated with electron-based microcopy techniques [8] and APT [9]. These are described below.

Figure 17 is a STEM-HAADF image and a series of STEM-EDS images of a lift-out specimen with the upper portion near the free surface of proton irradiated 308L. This set of images shows a δ ferrite grain extending downward in the middle of the imaged region. Based on the STEM-EDS maps in Figure 17, the BCC δ ferrite is rich in Cr and poor in Ni. In contrast, FCC γ austenite is rich in Ni, which is an FCC crystal stabilizer. The precipitates observed in Figure 17 are best seen in Figure 17d (the Ni map) as small dots within the elongated δ grain, indicating the precipitates contain Ni. Figure 17d demonstrates that these precipitates are uniformly distributed from the surface to a depth of approximately 10 µm within the irradiated δ ferrite. Moreover, no obvious evidence exists that same type of precipitates are seen in

irradiated γ austenite. It seems that these precipitates are favored to precipitate in proton irradiated δ ferrite rather than γ austenite. We provide a physical basis for this observation in the computational section based on first principles computations.

Figure 18a is an HAADF image that includes two γ austenite grains and two δ ferrite grains of irradiated 308L filler material at a depth approximately 10 μm below the irradiated free surface. Voids are observed in the irradiated γ-austenite, indicated in Figure 18a. Figure 18b is a STEM-EDS elemental line scan between the γ austenite grains along the cyan arrow in Figure 18a. Figures 18c-g are EDS elemental maps from the rectangular region indicated in Figure 18a. This region contains a γ–γ grain boundary and several twin boundaries. Cr depletion can be seen along the γ-γ grain boundary (Figure 18b) and along twin boundaries inclined approximately 45 degree to the γ-γ grain boundary in Figure 18d. Ni enrichment is observed at these same boundaries in Figure 18e. Cr depletion, Ni and Si enrichment is more prominent in the STEM-EDS line scan profile in Figure 18b and the right-most Figure-18 in absolute units. We compare these RIS data to simulations based on kinetic rate theory and the inverse Kirkendall effect in Section 4. In summary, the γ-γ grain boundaries are depleted in Cr and Mn and enriched in Ni and Si. This observation is consistent the inverse Kirkendall effect. Ni-, Si-, and Mn-rich particles are detected in δ ferrite grains; these are evident from Figs. 18e, 8f and 8g. These precipitates are identified as G-phase precipitates based on STEM-EDS, HR-STEM and TEM-SAD.

Figure 19a is a higher magnification HAADF image acquired in an irradiated δ ferrite grain showing cuboid 20 nm G-phase precipitates enriched in Ni, Si, and Mn, as Figs. 19d-f demonstrate. These precipitates are also poor in Fe and Cr (Figs. 19b and c). It is interesting that these precipitates, which are Ni rich, exist in the Ni-poor δ ferrite phase. Clearly enhanced diffusivity of Ni must exist during irradiation to facilitate precipitate growth. Lattice structure (black lines) of δ ferrite can be clearly seen in the HAADF image (Figure 19a). The δ ferrite lattice shows significant strain near the G-phase and it is clear that the two lattices are distinct.

High resolution STEM micrographs are shown in Figure 20. These images show the structural correlation between the G-phase and host δ ferrite lattice. The $Mn_6Ni_{16}Si_7$ G-phase has a cubic structure (space group: $Fm\bar{3}m$). Inset of Figure 18a indicates that [001]G//[001]δ correlation exists. Figure 20b is a small section from Figure 20a at higher magnification. STEM micrographs have mass contract, with heavier elements appearing brighter. This allows us to distinguish different elements in the high resolution micrographs and overlay the G-phase and δ ferrite [001] lattice planes in Figures 20b and 20c. It is clear that both phases are commensurate with a lattice parameter ratio very close to 4:1.

Figure 21a is a bright field TEM micrograph imaged from the proton irradiated 308L filler at a depth of approximately 10 μm showing both δ ferrite and γ austenite grains. G-phase precipitates (tiny black dots) are observed in the δ ferrite grains. The parallel bands in γ austenite grains are twin boundaries. Two commensurate sets of diffraction patterns are observed in Figure 21b. The diffraction patterns of the δ ferrite (yellow dashed box) and G-phases $Mn_6Ni_{16}Si_7$ (cyan dashed box) showed a lattice ratio of 4:1 along the [113] zone axis of the micrograph. This agrees with our observation in Figure 20 and allows us to conclude the precipitates in proton irradiated δ ferrite is G phase ($Mn_6Ni_{16}Si_7$). Note these are matrix G phase precipitates, not grain boundary precipitates. Early observations of G phase particles indicated intergranular precipitation and hence "G" phase.

We confirm G phase precipitation in δ ferrite with DFT computations in the next section. We also compare the quantitative elemental segregation and depletion at the γ–γ grain boundary measured with STEM-EDS (Figure 18d) to simulations based on kinetic rate theory in the next section.

Voids are observed in proton irradiated γ austenite, as shown in Figure 22a. STEM-EDS line scan was performed across a void, as indicated in the bottom left inset of Figure 22a. The line scan map in the top left inset of Figure 22a shows that all the elements in the void region (around 30 μm) are depleted, as expected. In addition, the Ni and Si signals peak at the edge of voids. The STEM-EDS map in Figure 22b-22f demonstrate that all elements are absent from the regions attributed to voids, again as expected. These maps also show Ni and Si enrichment around the periphery of the voids, indicating the void-matrix boundaries are energetically favorable to Ni and Si segregation.

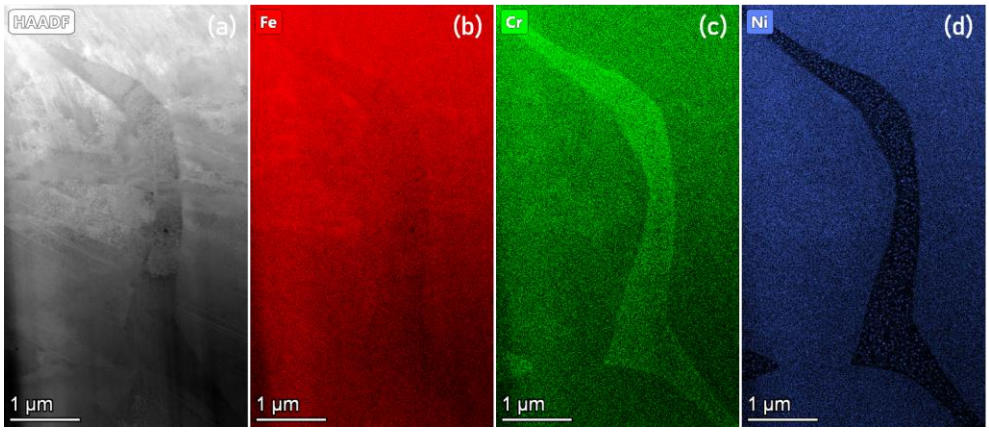

Figure 17. (a) STEM HAADF micrograph proton irradiated 308L filler material, the upper portion is close to the free surface. (b) STEM-EDS Fe map, (c) STEM-EDS Cr map, (d) STEM-EDS Ni map. Ni enriched dots (precipitates) are clearly seen in the δ ferrite grain running from the upper left, down through the center of the micrograph, to the lower right.

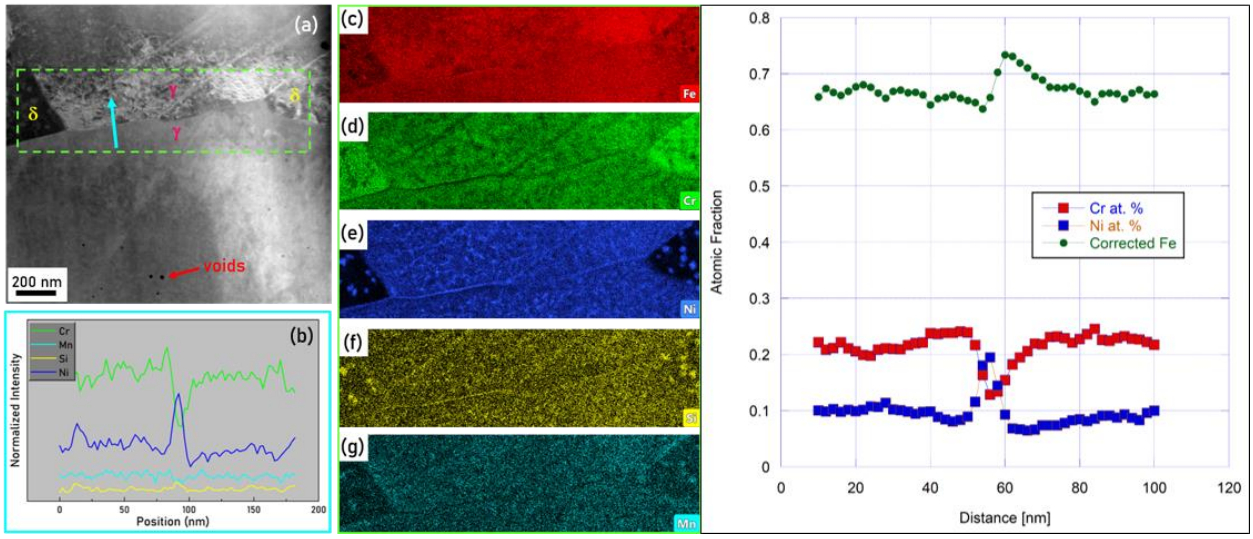

Figure 18. (a) HAADF image of proton irradiated 308L filler showing several phase boundaries at a depth of approximately 10 μm, (b) STEM-EDS line scan profile, (c) STEM-EDS Fe map, (d) STEM-EDS Cr map, (e) STEM-EDS Ni map, (f) STEM-EDS Si map, (g) STEM-EDS Mn map. The elemental maps are from the rectangular box in Figure 18a. The line scan in Figure 18b is along the upward arrow in Figure 8a. Voids that formed in γ austenite are identified in Figure 18a. The right-most image shows the elemental line profiles in absolute concentration and included a larger area than Figure 18b. The asymmetry of Fe at the grain boundary is an artifact due to the Cr and Ni profiles; Fe is calculated as the balance of all elements against a concentration of one and is denoted as "corrected" Fe.

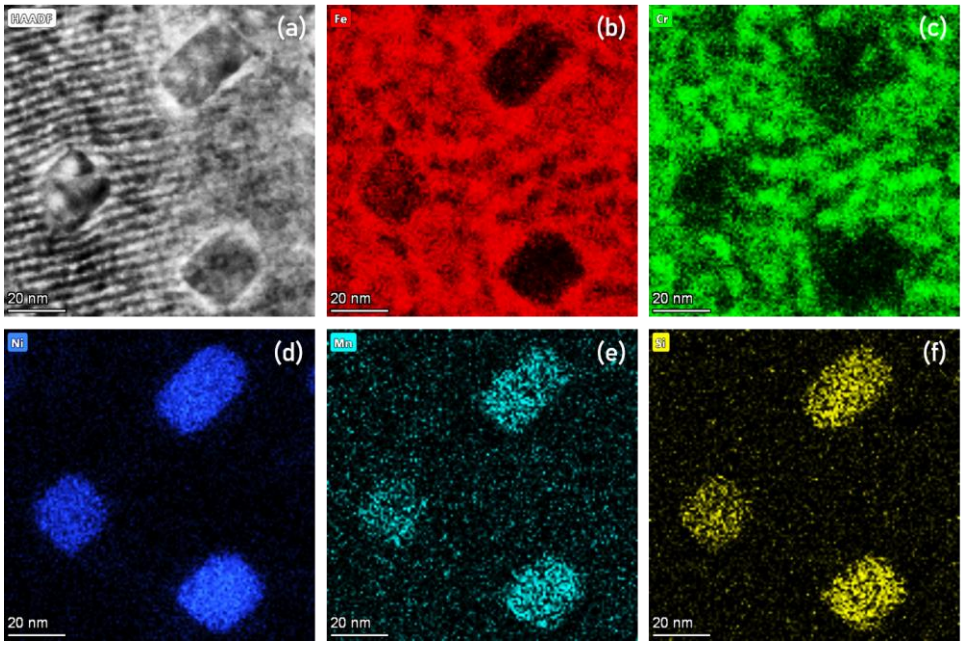

Figure 19. (a) HAADF image of δ ferrite with cuboid matrix G phase precipitates at a depth 10 micrometers below the free surface in 308L. The fringes are resolved lattice planes of δ ferrite, (b) STEM-EDS Fe map, (c) STEM-EDS Cr map, (d) STEM-EDS Ni map, (e) STEM-EDS Mn map, (f) STEM-EDS Si map.

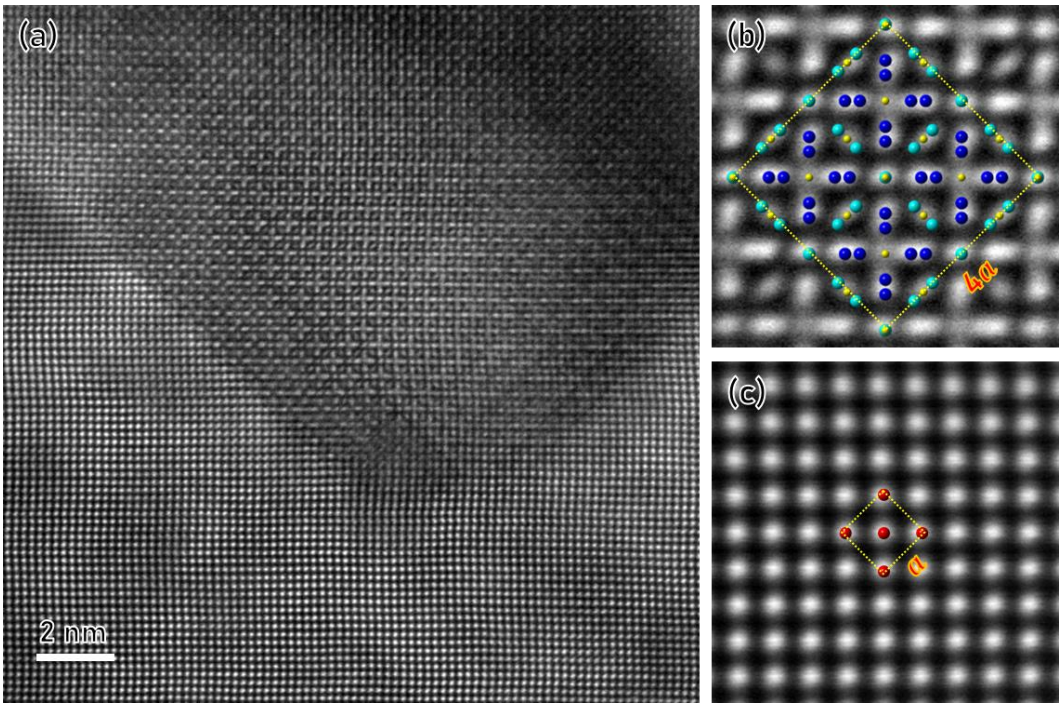

Figure. 20. (a) STEM HR micrograph of G-phase precipitates in proton irradiated δ ferrite from the 308L filler material, (b) lattice structure of G-phase precipitate at higher magnification with an overlay of Ni (blue), Si (yellow), and Mn (cyan) G-phase, (c) lattice structure of δ ferrite at higher magnification with an overlay of Fe (red). The zone axis for Figures 20b and c is [001].

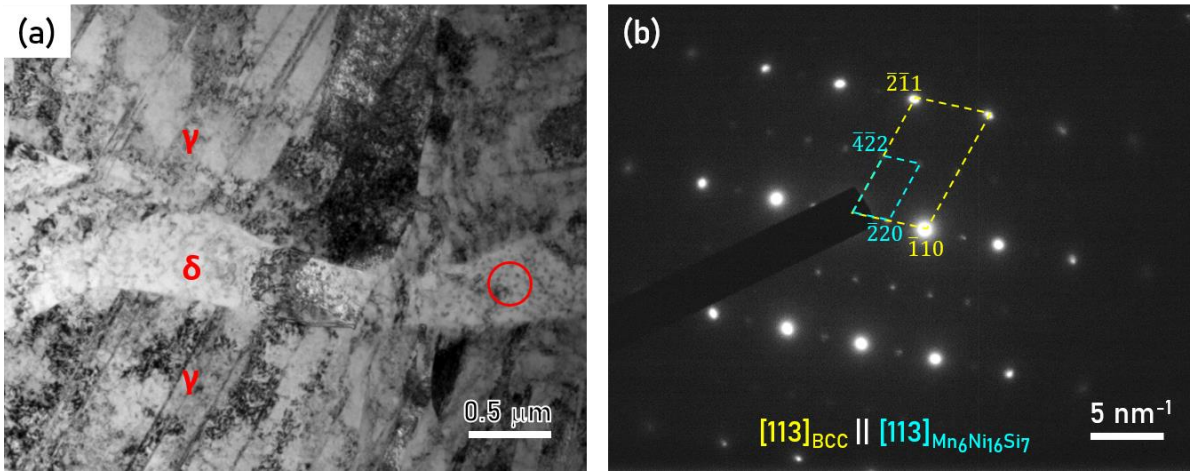

Figure 21. (a) Bright field TEM micrograph of proton irradiated 308L filler material with ferrite and austenite grains labeled. Black dots are G-phase precipitates in δ ferrite. Twinning is observed in the austenite grains, (b) selected area diffraction pattern from δ ferrite and G-phase $Mn_6Ni_{16}Si_7$ precipitates: yellow dotted box is the diffraction pattern of δ ferrite and cyan dotted box is the diffraction pattern of G-phase. The red circle in (a) is the SAD region for (b).

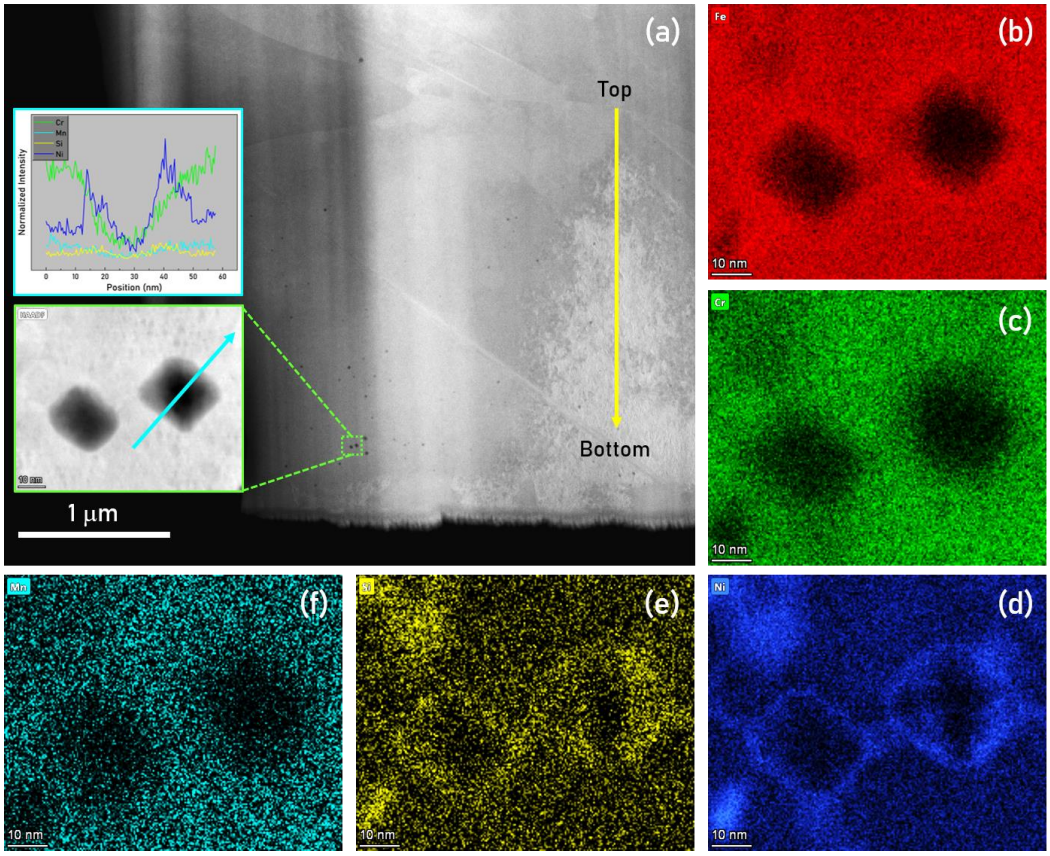

Figure 22. Analysis of irradiated duplex 308L material. (a) HAADF image of a proton irradiated γ austenite grain exhibiting voids at a depth of approximately 10 μm; inset is a STEM-EDS line scan profile cross void as shown, (b) STEM-EDS Fe map, (c) STEM-EDS Cr map, (d) STEM-EDS Ni map, (e) STEM-EDS Si map, (f) STEM-EDS Mn map. The Ni and Si maps indicate an enrichment at void boundary.

Nickel and Si clustering is evident in Figures 18e and 18f in 308L groove filler material. We investigated this clustering with APT in 308L. In addition, G phase particles and a γ–δ phase boundary was studied with APT in 308L. Atom probe tomography facilitates analysis unique to this characterization technique. Here we use cylinders with diameter of 2 nm (smaller than the dimension of G phase particles and Ni-Si clusters) analyze the concentration profiles associated with the 15 at. % Ni iso-surfaces of the G phase, the δ-γ phase boundary, and the Ni-Si clusters. This analysis is shown in Figure 23. Elemental line-scan profiles (determined by averaging within the analysis cylinder) between G phase and bulk δ ferrite demonstrates that significant elemental variation is exists in two different phases, as indicated in Figure 23b. As expected, the G phase is rich in Ni, Si and Mn. Fe concentration changed from 65 at. % in δ ferrite to as low as 10 at. % in G phase, Cr from 30 at. % to 5 at. %. Ni concentration in G phase can reach as high as 55 at. %, while in δ ferrite Ni is lower than 5 at. %. In addition, Si and Mn concentration in G phase can be as high as 25 at. % and 15 at. %, respectively. In contrast, the variation of elements between Ni-Si cluster and γ austenite in Figure 23d is smaller, as shown in Figure 23d. Ni and Si enrichment is seen in Ni-Si clusters (spots 1 and 2 in Figure 23a), while Mn is not enriched at either location. Fe and Cr concentration differences between Ni-Si clusters and γ austenite are lower compared to those between G phase and δ ferrite. Ni concentration in Ni-Si clusters is as high as 35 at. % and Si concentration in spots 1 and 2 reached 10 at. %. Fe concentration changed from 65 at. % in γ austenite to 55 at. % in Ni-Si cluster, Cr from 20 at. % in γ austenite to 10 at. %. δ-γ phase boundary in Figure 23c is around 4 nanometers thick. The δ-γ phase boundary line-scan profile in Figure 23c can be divided into two regions: a Cr depletion and Fe enrichment region close to the proton irradiated δ grain and a Ni/Si enrichment and Fe depletion region adjacent to the proton irradiated γ grain.

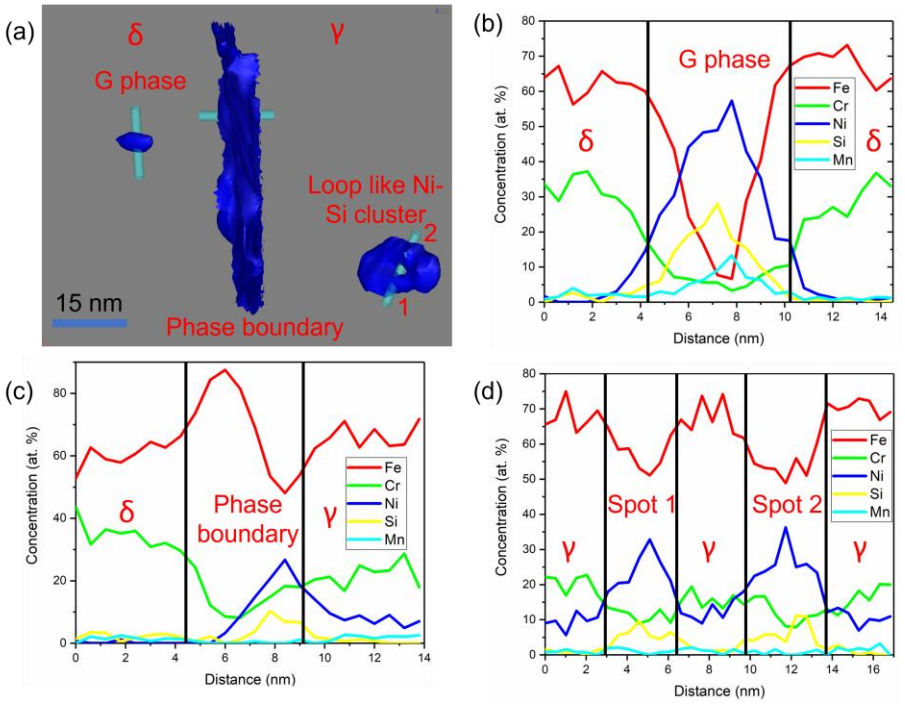

Figure 23. (a) 15 at. % Ni iso-concentration surfaces showing the location of analysis cylinders with diameter of 2 nm for a G phase in proton irradiated δ ferrite grain, a δ-γ grain boundary between proton irradiated δ ferrite and γ austenite grains, and a loop-like Ni-Si cluster; (b) elemental line scan profile of G phase (Mn6Ni16Si7) in proton irradiated δ ferrite grain; (c) elemental line scan profile of δ-γ grain boundary; and (d) elemental line scan profile of Ni-Si cluster in proton irradiated γ austenite grain.

Iso-concentration surfaces (iso-surfaces) at a concentration of 15 at. % Ni, 6.6 at. % Si, and 5.6 at. % Mn (the same atomic ratio of Ni, Si and Mn as the G phase) are shown in Figure 24. This rendering reveals the G phase particles and the Ni-Si clusters in the proton irradiated δ ferrite grain and γ austenite grain, respectively. The G phase precipitates in δ ferrite grain at the free surface have spherical or cuboid morphology. As shown in Figure 24, Ni and Si are observed to segregate to the δ/γ phase boundary. In addition, Ni-Si enriched clusters with line and loop morphologies are observed in proton irradiated γ austenite grains. These features were detected with STEM-EDS in Figure 18, but the APT reconstructed renders these features in three dimensions. We believe some clusters decorate Frank loops induced by radiation damage.

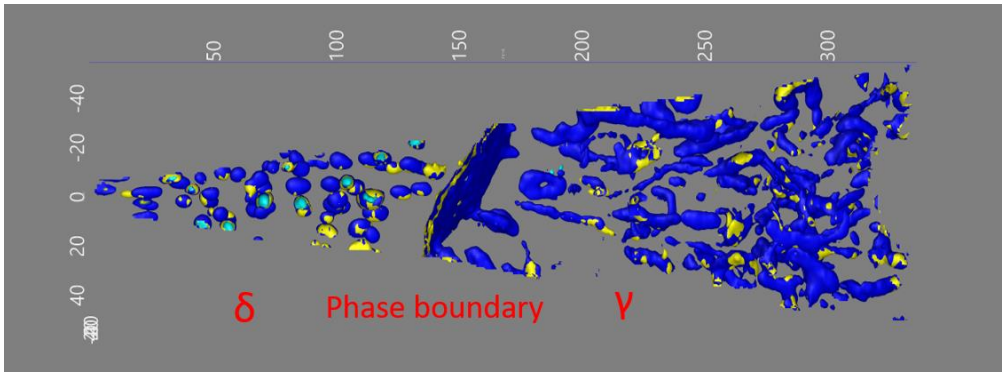

Figure 24. Ni, Si and Mn iso- surfaces in an APT reconstructed tip. The reconstructed tip was fabricated from a FIB lift out at the free surface. The total length of the tip was approximately 350 nm. 15 at. % Ni (blue), 6.6 at. % Si (yellow) and 5.6 at. % Mn (cyan) iso-concentration surfaces were selected to reveal the G phase particles and Ni-Si enriched clusters in proton irradiated δ ferrite grain and γ grains, respectively. This specimen included a phase boundary near the middle of the tip. Approximately 84 million atoms were detected for this specimen.

The TRIM simulation shown in Figure 12 demonstrates the differential damage of protons in 308L increases to a peak at a depth of approximately 18 μm. The TEM specimens were lifted out at depths of approximately 10 and 18 μm, respectively. The APT specimen was taken from the free surface. The corresponding displacements per atom (dpa) increases from approximately 3 dpa at the free surface, to 5 dpa at 12 μm (this depth corresponds to 60% of the peak depth), to approximately 50 dpa at a depth of 18 μm corresponding to the peak in Figure 12. This assumes dpa scales linearly with the TRIM calculated differential energy to recoils and displacements per Å.

We assume a spherical morphology for the G phase particles to determine particle density and volume fraction, both tabulated versus depth in Table 3. Histograms are shown in Figure 25. Histogram in Figure 25d is generated after processing 59 G phase particles in a 50 nm by 150 nm APT Ni iso-surface map (Figure 25a) with a Ni concentration of 28 at. %. The APT data is a three-dimensional profile, but we analyzed the G phase particles using a two-dimensional projection by ImagJ. In addition, the largest diameter at the tip-end of δ ferrite grain, seen in Figure 25a, is less than 50 nm, which is two times thinner than our TEM sample (around 100 nm). Over 70 % of the G phase particles have the diameter between 3 to 6 nm in Figure 25d. After analyzing a total of 49 G phase particles in a 500 nm by 500 nm TEM bright field micrograph (Figure 25b) captured at a depth of 10 μm, histogram in Figure 25e indicates that 60 % of

the 49 G phase particles have the diameter ranging from 15 µm to 30 µm. In addition, histogram in Figure 25f is produced after processing 72 G phase particles in a 300 nm by 300 nm TEM bright field micrograph (Figure 25c). Around 80 % of the 72 G phase particles have the diameter in the range of 20 to 35 µm. The histograms presented in Figure 25 demonstrate that G phase precipitate size increases with depth.

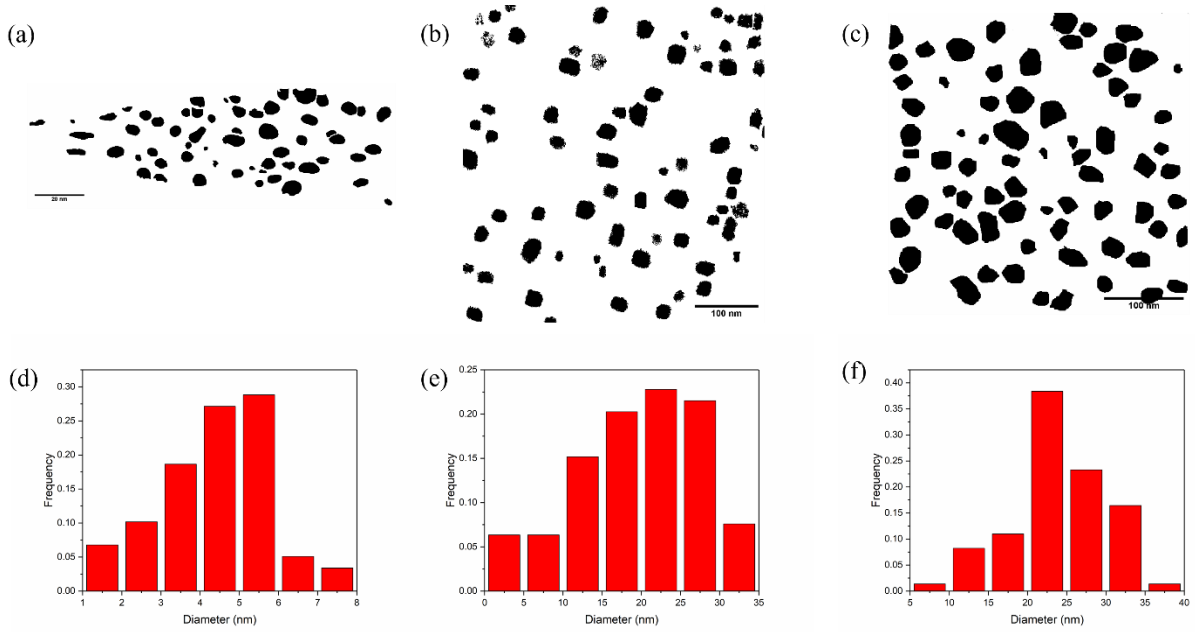

Figure 25. (a) Reconstructed APT image of G phase precipitates in proton irradiated δ ferrite at a depth of 100 nm processed by ImageJ, (b) TEM image of G phase precipitates in proton irradiated δ ferrite at a depth of 10 µm processed by ImageJ, (c) TEM image of G phase precipitates in proton irradiated δ ferrite at a depth of 18 µm processed by ImageJ, (d) Histogram of size distribution of G phases in proton irradiated δ ferrite grain from the reconstructed APT micrograph at 10 nm, (e) Histogram of size distribution of G phases in proton irradiated δ ferrite grain from the TEM micrograph at 10 µm, and (f) Histogram of size distribution of G phases in proton irradiated δ ferrite grain from the TEM micrograph at 18 µm.

Table 3. G phase density and volume fraction in 308L δ ferrite obtained from TEM and APT.

Depth (µm)	dpa	Density ($1/m^3$)	Volume Fraction
0.1	3	7.5×10^{23}	0.04
10	5	0.2×10^{21}	0.001
18	50	5.3×10^{21}	0.05

Since the volume of the APT tip is known and the thickness of TEM specimen at 10 and 18 μm was measured by EELS, the G phase density at free surface and at depths of 10 and 18 μm can be determined: 1.6×10^{23}, 0.2×10^{21}, and 5.3×10^{21} m^{-3} at the free surface, and at depths of 10 and 18 μm, respectively.

As seen in Table 3 volume fraction (total volume of G phase particles divided by the total volume of the analyzed δ ferrite region) at different depth are tabulated. At 10 μm, the volume fraction of G phase particles is 0.001, while that at 18 μm is 0.05. The dpa from proton irradiation increases from 5 dpa to around 50 dpa and the G phase volume fraction scales with dpa. However, the volume fraction of G phase at the free surface from APT analysis is large (0.04) and does not scale with dpa. One possible explanation is that the free surface, which is an unbiased since, induces a flow of point defects during proton irradiation. This defect flow then induces greater G phase density and volume fraction than would otherwise be expected based on the free surface dpa value.

In addition to G phase precipitates and Ni-Si clusters shown above, void formation in the proton irradiated γ austenite is shown in Figure 26. STEM images of voids at 12, 16, and 18 μm below the free surface are shown in Figure 26. Density of these voids versus depth is calculated from number of voids in a 575 nm by 575 nm STEM micrograph cross section with the thickness determined by EELS analysis. The thicknesses determined with EELS at depths of 12, 16, and 18 μm are 246, 190, and 152 nm, respectively, using an inelastic mean free path of 114 nm for 308 γ austenite [10]. Using these thickness values and the STEM micrograph void count (46, 90, and 130 voids were identified in Figure 26c, 26b and 26a, respectively), the corresponding void densities are 0.6×10^{21}, 1.4×10^{21}, 2.6×10^{21} $1/nm^3$ at depths of 12, 16, and 18 μm, respectively.

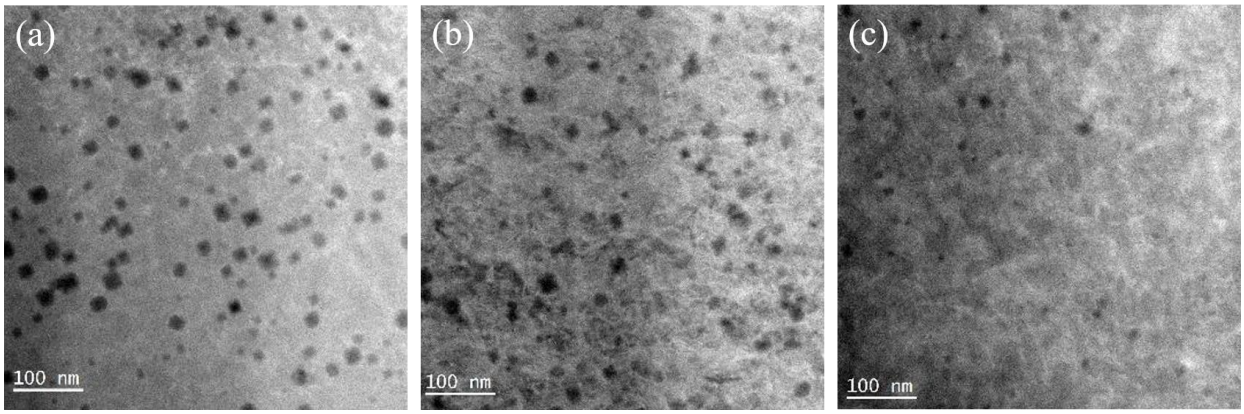

Figure 26. STEM micrographs of proton irradiation induced voids in γ austenite at depths of (a) 18 (b) 16 μm, and (c) 12 μm.

We overlay the calculated G phase particle and void densities at 10 and 18 μm on the TRIM damage profile in Figure 27. Overall, both the G phase particle and void densities scale with dpa damage, with the exception of the near-surface G phase particle density from analysis of the APT data, as explained above.

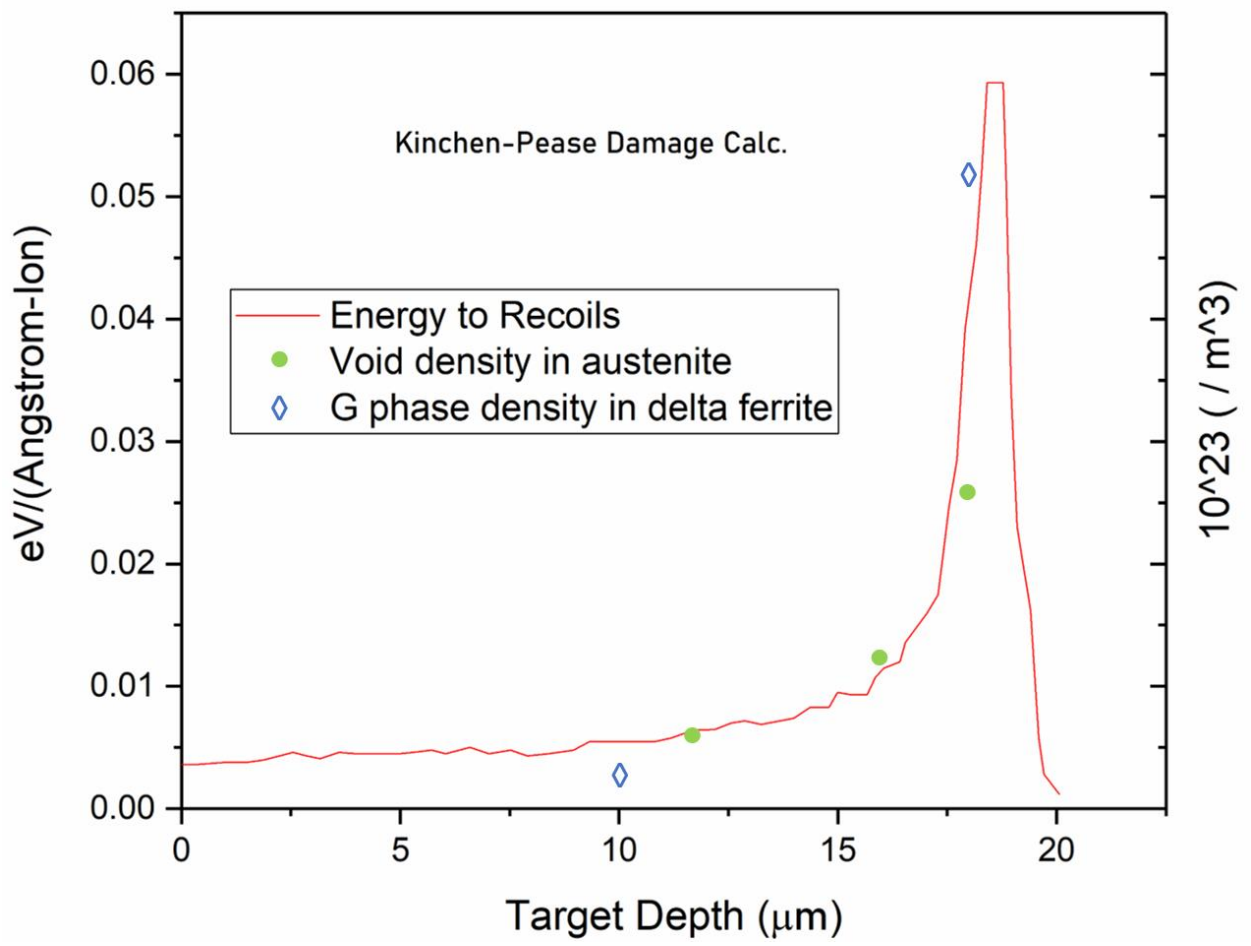

Figure 27. Void and G phase particle densities in proton irradiated γ austenite and δ ferrite, respectively, as a function of depth overlaid with proton irradiation damage profile in 308L simulated by TRIM. The y axis on the left of the figure is the damage profile and on the right of the figure is density.

Microstructure Associated with Proton Irradiation of 309L Butter

The microstructure of the 309L butter material is different than that of the 308L groove filler material even though the compositions are similar (see Table 1). The most significant difference in the 309L butter are the higher Cr and Ni concentrations. We note the DFT analysis presented in Section 4 is independent of these composition differences since only BCC and FCC iron are considered. A dilution zone formed at the SA508-309L butter interface (see Figure 4). The dilution zone is single phase γ austenite; carbon diffusion (an austenitic stabilizer) from SA508 into the 309L butter during the welding process (and possibly the PWHT) promoted the formation of the 1-4 mm thick dilution zone. The 309L butter beyond the dilution zone has a δ–γ duplex microstructure and this is shown in Figure 28 for the proton irradiated material.

A distinct evolution in the *irradiated* 309L microstructure is observed in Figure 28 versus distance from the SA508-309L interface. The first 4 mm were irradiated with 2 MeV protons, while the last 4 mm were unirradiated. Enlarged regions at 2, 4, and 7 mm are shown in Figure 29. Intergranular precipitation on the γ–δ phase boundaries is observed within the irradiated portion of the duplex region of 309L. The 7-

mm material was unirradiated and no precipitation is observed. The intergranular precipitates are rich in Cr and are identified as $Cr_{23}C_6$ carbides below.

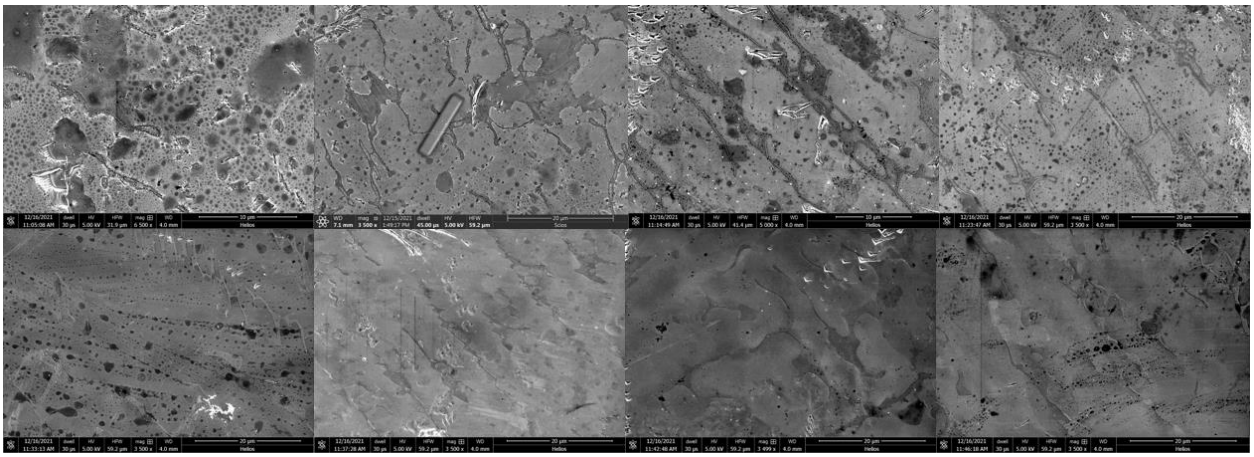

Figure 28. SEM images of proton irradiated 309L butter relative to the SA508-309L butter interface. Clockwise from upper left: 1 mm from the interface to 8 mm from the interface in 1 mm increments, moving into the 309L butter. The δ–γ duplex microstructure is observed and a Pt capping layer for a FIB lift out has been placed over this microstructure at 2 mm. The first 4 mm from the interface were irradiated with 2 MeV protons.

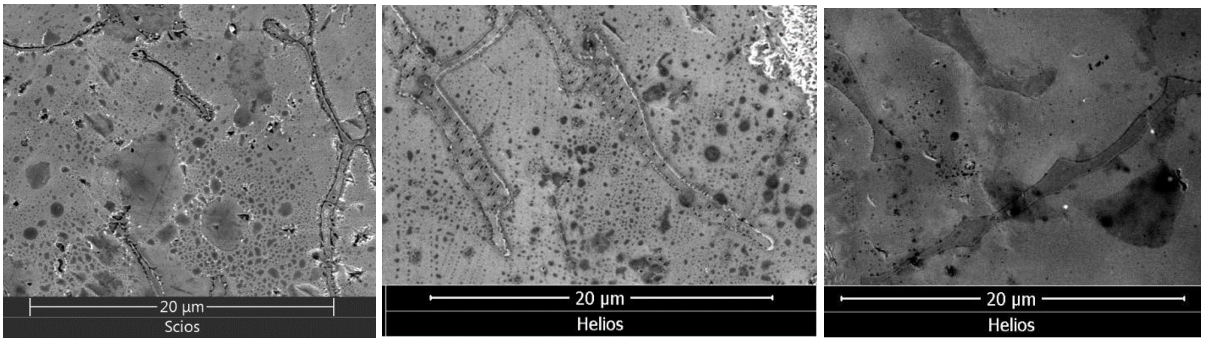

Figure 29. Changing precipitation morphology in the δ ferrite phase of the 309L duplex microstructure versus distance from the SA508-309L interface. (left to right) 2 mm/intergranular precipitation; 4 mm/intergranular precipitation; 7 mm/no precipitation

A FIB lift out in the 309L butter was performed approximately 1 mm from the SA508-309L interface and is shown in Figure 30. This lift out capture a γ–γ grain boundary intersecting the free surface and a δ ferrite particle embedded in the γ matrix below the free surface. STEM-EDS was used to map the relevant elements associated with the γ–γ grain boundary at the free surface and these maps are shown in Figure 30. Chromium depletion and Ni segregation is observed at the γ–γ grain boundary (Figure 30c and 30d), consistent with proton irradiation induced RIS, similar to that shown above in Figure 18. Further, a Cr-rich oxide (Figure 30g is the oxygen map) and a Cr depletion layer are observed at the free surface. The surface of this sample was etched after irradiation to provide microstructural contrast. This etching preferentially attacked the γ–γ grain boundary at the intersection with the free surface where Cr depletion occurred.

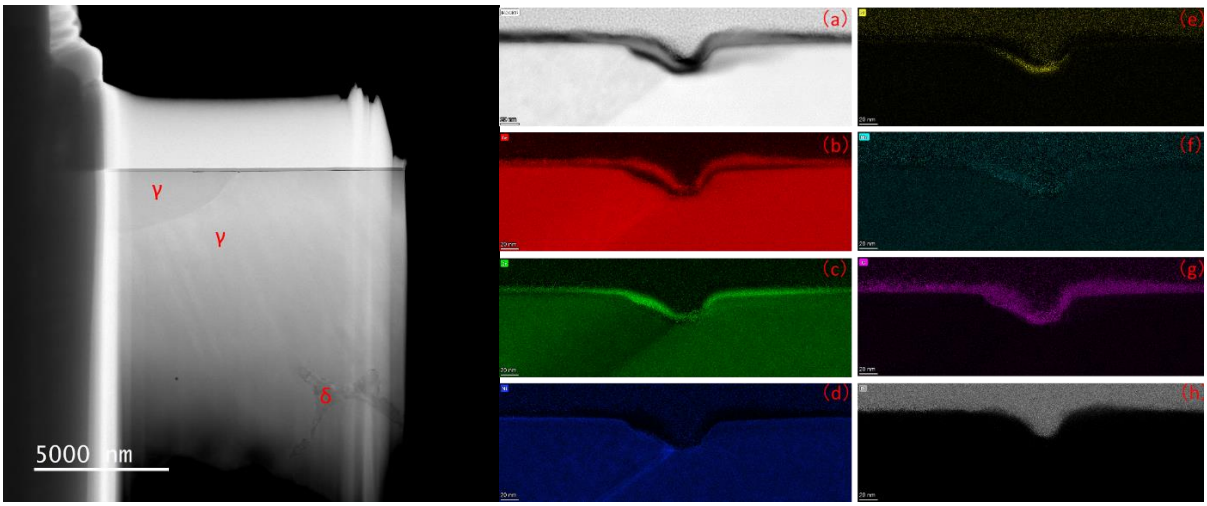

Figure 30. (left) SEM image of a FIB lift out that captured a γ–γ grain boundary and a δ ferrite particle embedded in the γ matrix below the free surface. (right) HAADF micrograph and STEM-EDS elemental maps of the γ–γ grain boundary region.

Analysis of the Figure 30 STEM-EDS data is shown in Figure 31. The line scan profile at the free surface shows the oxide and possibly RIS. Note the peak in the Ni signal; this likely would not have occurred if the only perturbing effect was Cr oxide formation. We therefore believe the depletion of Cr just below the oxide is due, at least in part, to RIS, as is the enhancement of Ni. The case for RIS at the γ–γ grain boundary is less clear. Chromium depletion and Ni enrichment is observed at the grain boundary, but the EDS map dimensions are constrained and a larger map extending to downward is required.

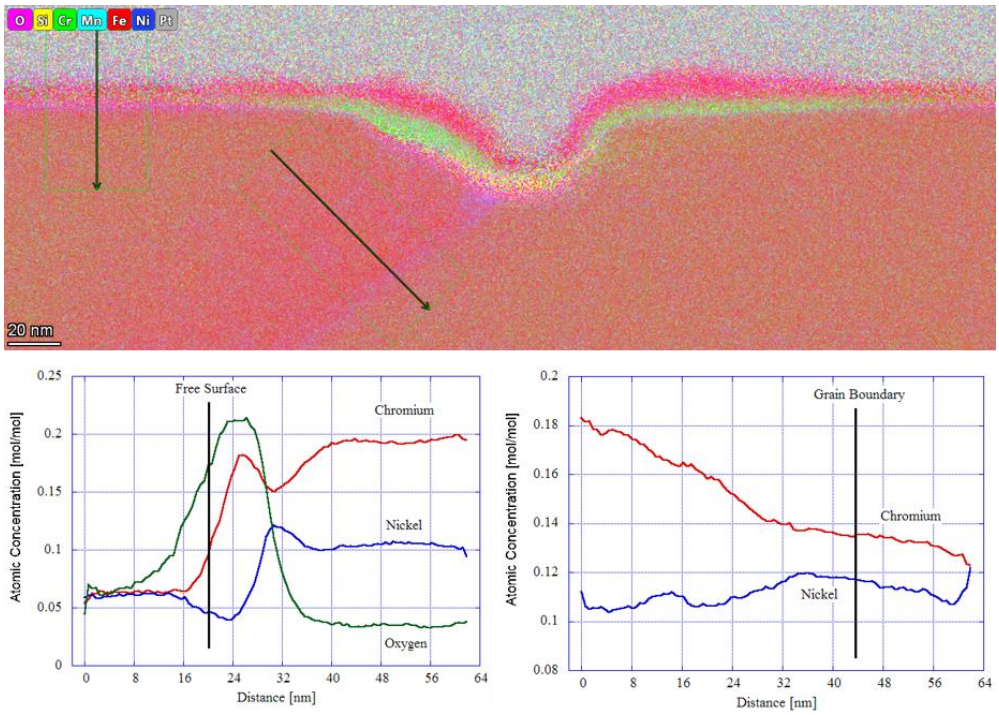

Figure 31. (top) Composite STEM-EDS map of the γ–γ grain boundary intersection at the free surface in proton irradiated 309L (composite image is merged data from Figures 30b to h). Line profile scan boxes and directions are identified. (bottom left) Line scan profiles at the free surface. (bottom right) Line scan profiles at the γ–γ grain boundary.

The STEM-EDS elemental map of the embedded δ ferrite particle is shown in Figure 32. This is the same γ ferrite particle embedded in the γ matrix in the lower portion of Figure 30 left. We have identified the intergranular precipitates as $C_{23}C_6$ based on SAD indexing using the known lattice parameters [11, 12] shown in Figure 33. The $C_{23}C_6$ precipitates are commensurate with γ austenite, as demonstrated by Figure 34. This carbide phase nucleated at the γ–δ phase boundary in Figure 32 and grew into the δ phase. It is important to note that the intergranular $Cr_{23}C_6$ precipitation is only observed in the proton irradiated regions of the 309L butter and is therefore the effect of irradiation. This is demonstrated in Figure 28 and 29; precipitation is not observed beyond 4 mm from the interface, which is outside of the irradiated region. This also demonstrated in Reference 2 and Figure 4a of the as-received 309L material; $M_{23}C_6$ precipitation was observed in the duplex region near the dilution zone.

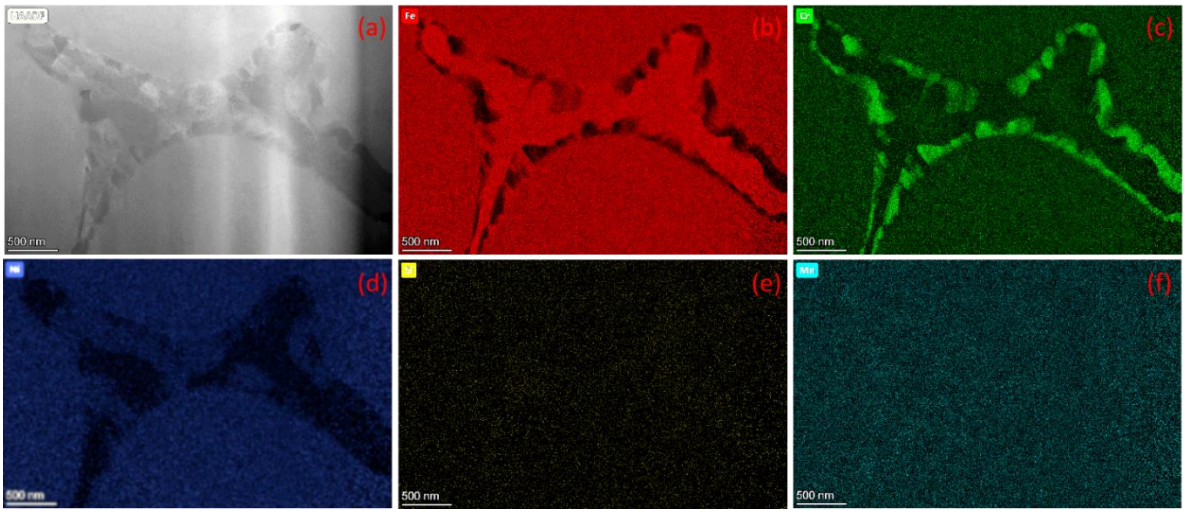

Figure 32. HAADF micrograph and STEM-EDS elemental maps of the embedded δ ferrite particle shown in SEM image of Figure 30. $Cr_{23}C_6$ intergranular precipitation is observed within the δ ferrite particle at the phase boundary.

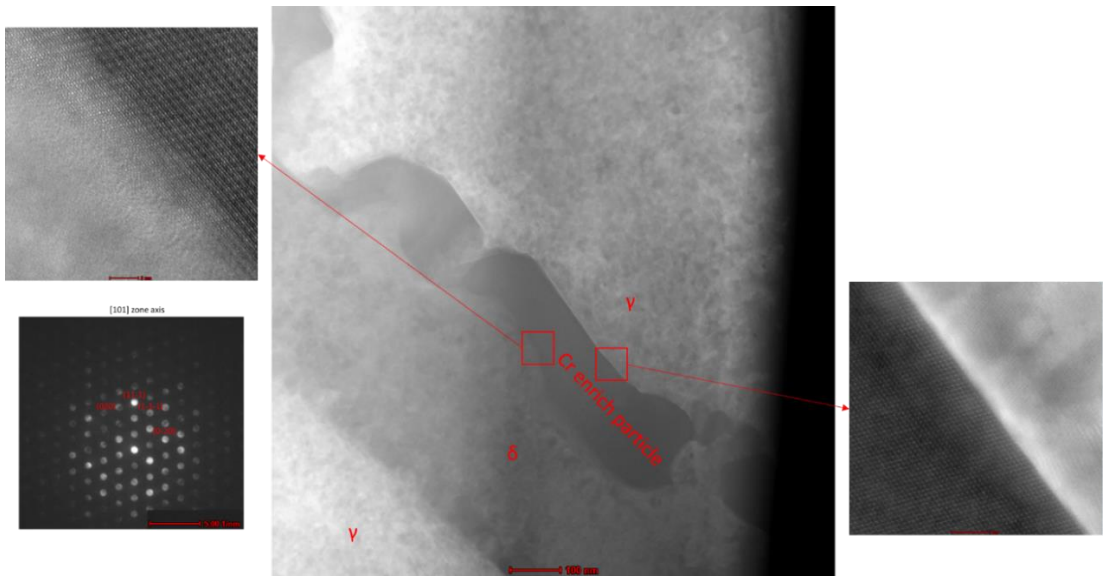

Figure 33. TEM analysis of the Cr-rich precipitates identified in Figure 32. The SAD patter (lower left) is indexed as *Fm3m* $Cr_{23}C_6$ [12]. The precipitates have commensurate interfaces with γ austenite.

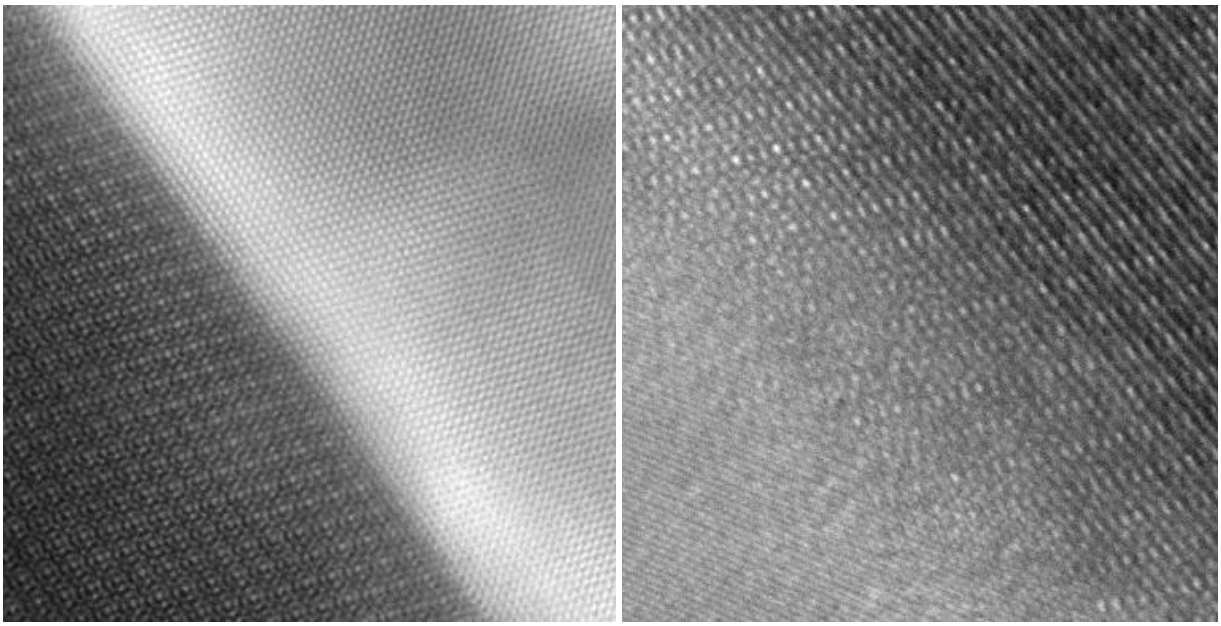

Figure 34. (left) HR TEM of the $Cr_{23}C_6$-γ austenite phase boundary showing the two lattices are commensurate. The $Cr_{23}C_6$ is to the left and γ austenite is to the right in this micrograph. (right) HR TEM of the $Cr_{23}C_6$-δ ferrite phase boundary with δ at the bottom—the lattices are not commensurate.

The most surprising observation of proton irradiated 309L is the lack of matrix G phase precipitation and Ni-Si cluster within the duplex region. Both microstructure features were observed in proton irradiated 308L. (The important distinction between the two alloys was $Cr_{23}C_6$ carbide precipitation induced by proton irradiation of 309L but not 308L, as discussed above.) A FIB lift out was performed at a location 4 mm from the SA508-309L interface within the proton irradiated region shown in Figure 35. The HAADF micrograph of this lift out is shown in Figure 36; two δ ferrite particles embedded in the γ matrix, one intersecting the free surface, are visible. STEM EDS elemental mapping at the two locations identified in Figure 36 are shown in Figures 37 and 38. Cr-rich precipitates are observable; these are presumably $Cr_{23}C_6$ carbides based on the above analysis. No G phase precipitation or Ni-Si clustering is observed in the proton irradiated 309L. Figures 39 and 40 show an enlarged region of the lower δ ferrite particle, further demonstrating the lack of G phase precipitation and Ni-Si clustering.

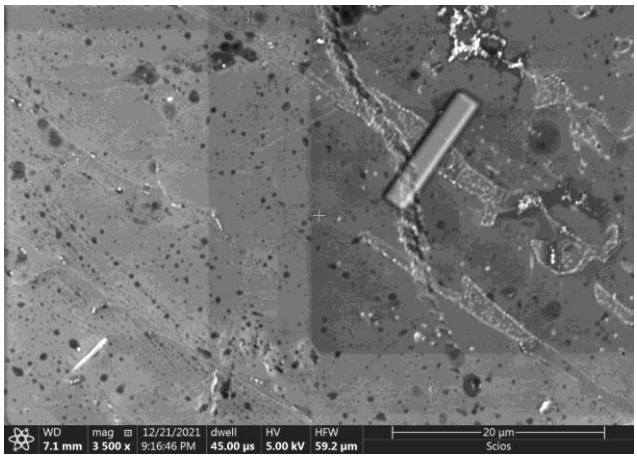

Figure 35. SEM image of the proton irradiated 309L duplex region showing the Pt capping layer used for the FIB lift out. The capping layer is over a δ ferrite particle.

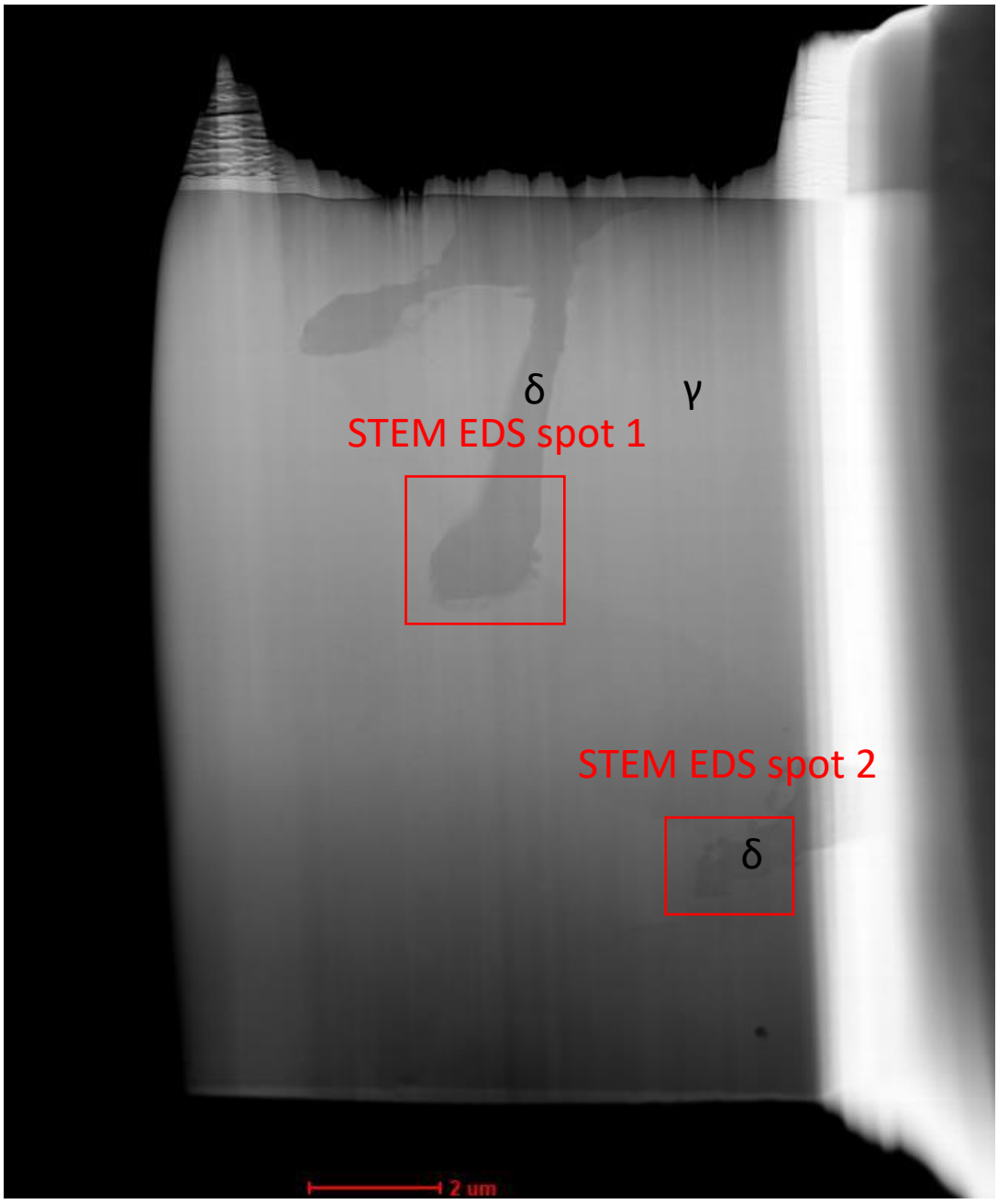

Figure 36. HAADF micrograph of the FIB lift out of proton irradiated 309L corresponding to the Pt capping layer in Figure 35. Two embedded δ ferrite particle are identified, one intersecting the free surface. Two locations of EDS mapping are shown.

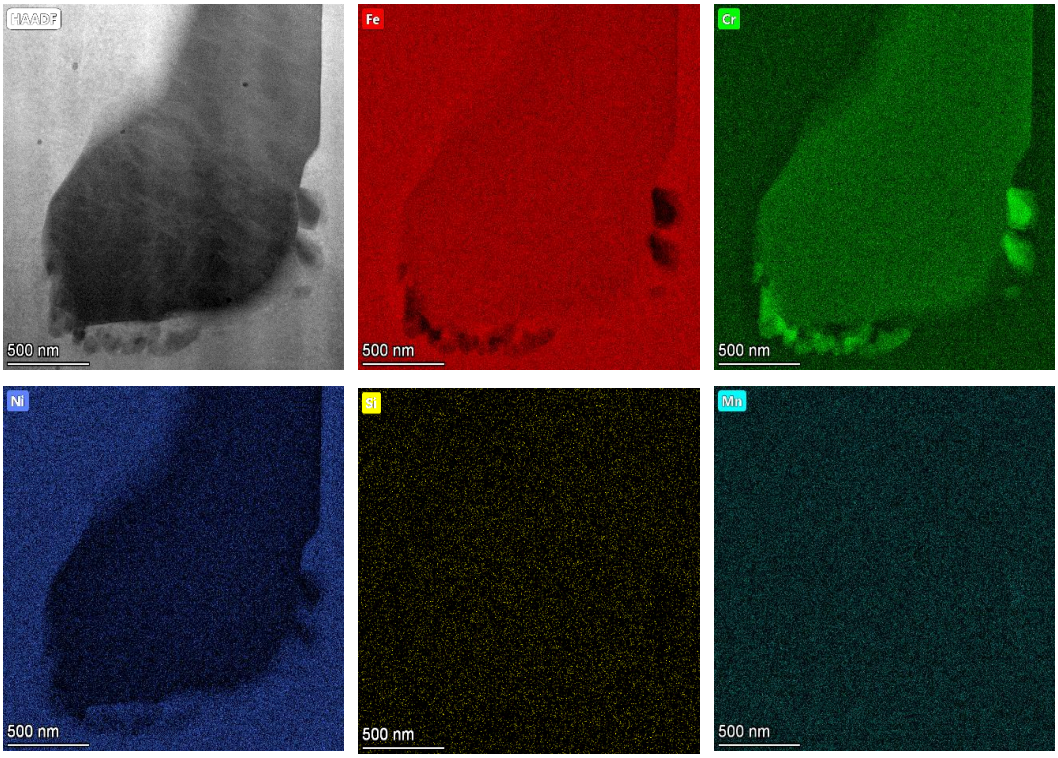

Figure 37. STEM EDS elemental maps of location 1 in Figure 36. Cr-rich precipitation is observed at the γ–δ phase boundary.

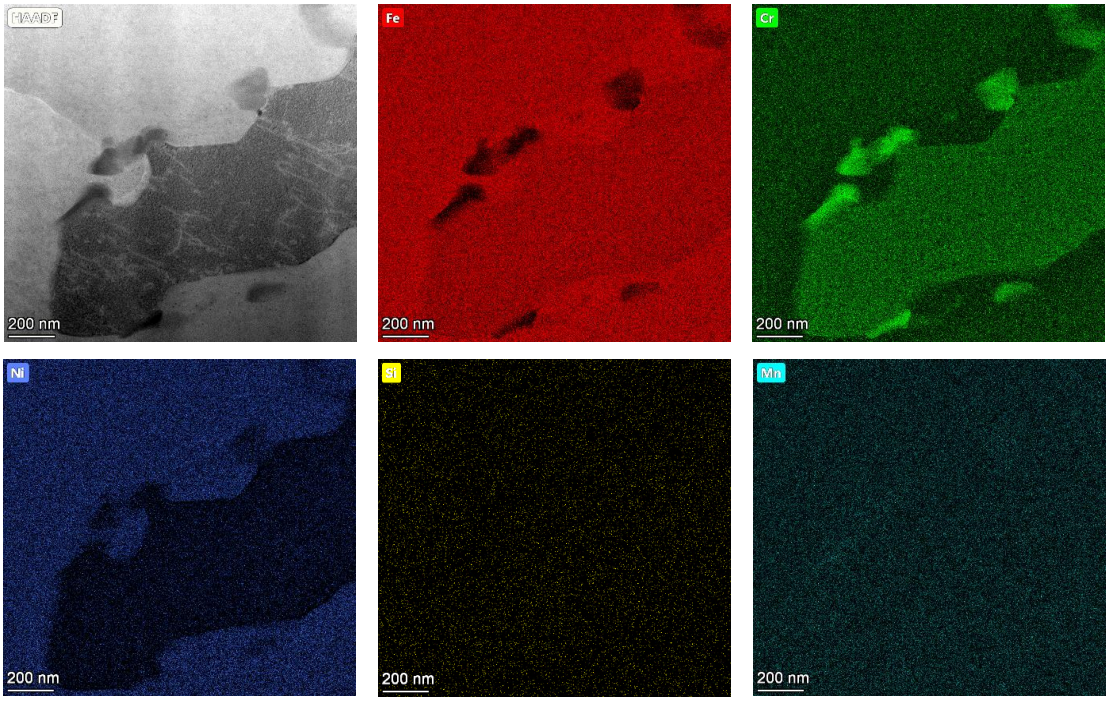

Figure 38. STEM EDS elemental maps of location 2 in Figure 36. Cr-rich precipitation is observed at the γ–δ phase boundary.

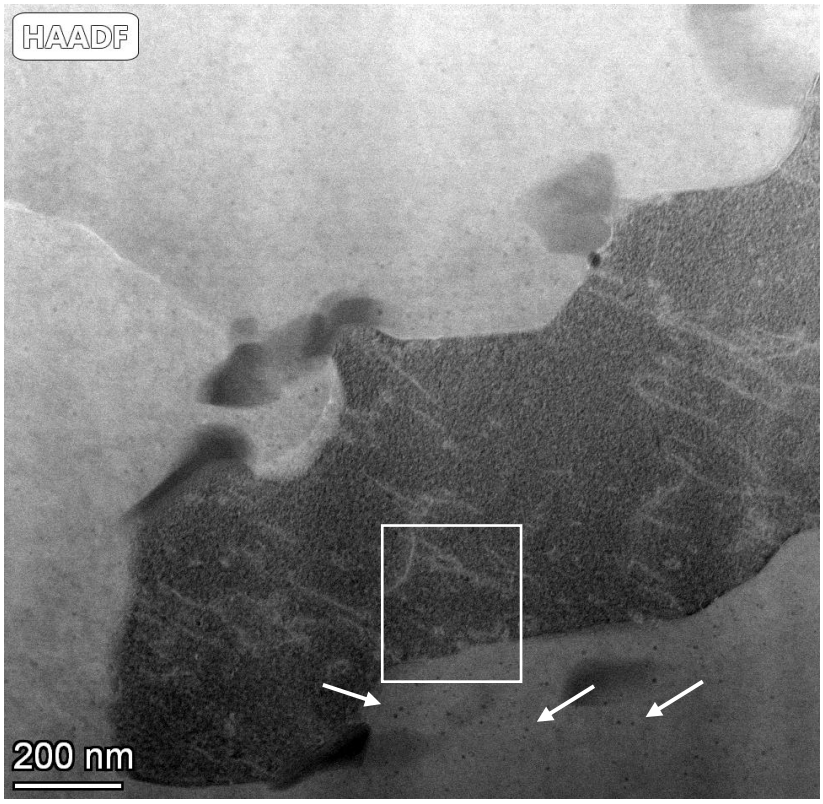

Figure 39. HAADF image showing enlarged region of the lower δ ferrite particle in Figure 36. The white box identifies the location of an EDS map and the white arrows show the location of voids in the proton irradiated 309L.

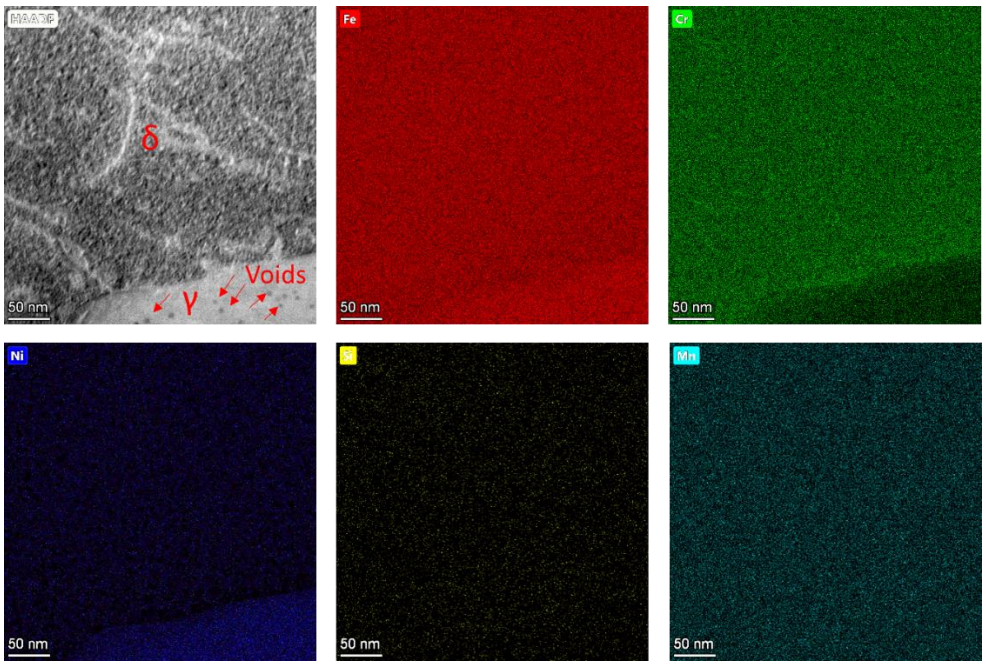

Figure 40. HAADF and STEM EDS elemental maps of the proton irradiated region of 309L identified in Figure 39. Voids are observed γ austenite. No G phase precipitation is observed. This is best seen by the Ni map compared to Figures 18e and 19d.

SCC and IASCC of SA508-304L Weldment

Proton irradiation was used to mimic displacement cascade damage associated with fast neutron bombardment. The dpa rate for these irradiations was approximately 10^{-5} 1/s. Tensile specimens and TEM bars were irradiated at 360 °C. This temperature corresponds to BWR temperature (290 °C) based on Mansur's invariant theory [13]. Proton irradiated samples were exposed to BWR NWC conditions for periods of one to six weeks. Samples were pulled to strain values of 4 to 7% or to failure.

A tensile specimen pulled to failure in the BWR NWC autoclave environment is shown in Figure 41. Approximately 8 mm of this tensile specimen was proton irradiated, centered on the SA508/309L interface. All cracking was observed within the proton irradiated region of the 309L butter. The failure surface was located within the 309L irradiated region was well. No evidence of cracking was observed beyond the proton irradiated region of either the SA509 or 309L. Further, all the cracks are within approximately 0.5 mm from the failure surface, as shown in Figure 41b. Extensive slip bands are seen in Figure 41 on both sides of the fracture surface.

SEM analysis of the facture surface shown in Figure 42 revels brittle crack propagation within near surface region corresponding to the range of the incident 2 MeV protons. At greater depths, a ductile facture surface is observed with characteristic dimpling associated with micro-void coalescence.

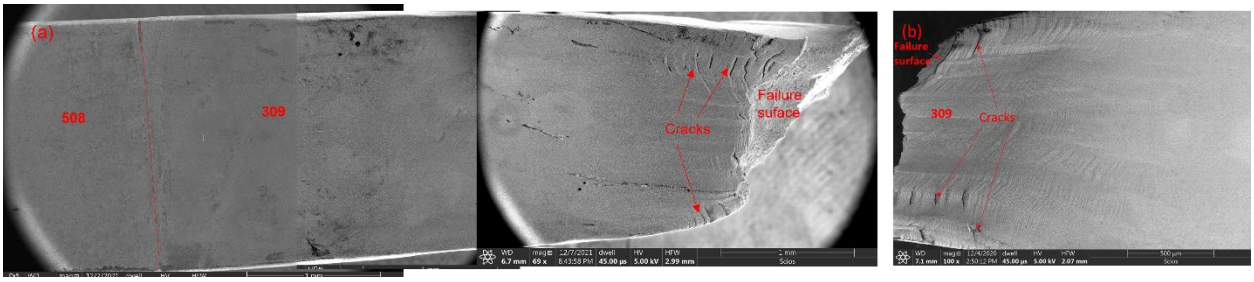

Figure 41. (a) Mosaic of the SAS508-309L interface. The unmarked interface near the middle of this image is an artifact of creating the mosaic. The middle portion of this image shows cracking on the irradiated surface near the SA508-309L interface, with the fracture surface as shown. (b) Cracking and slip bands within 309L on the irradiated surface opposite of that shown in the middle figure.

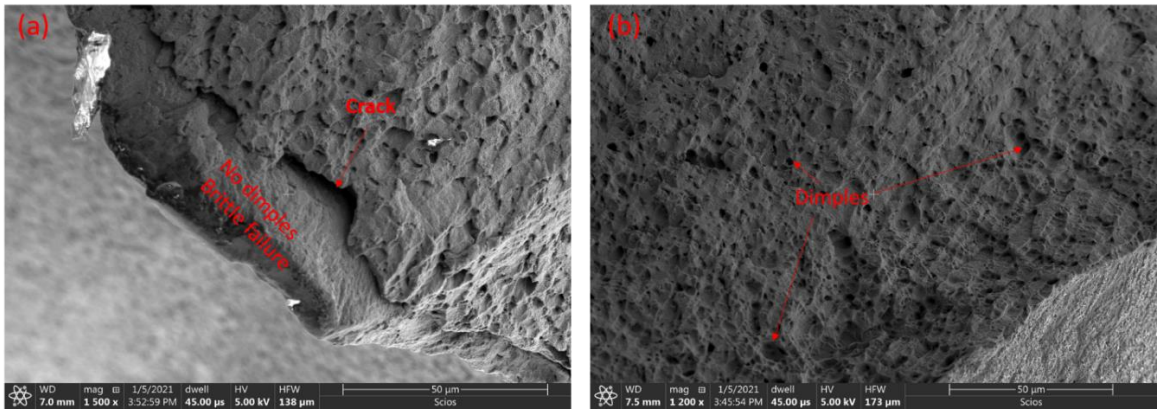

Figure 42. SEM micrographs of the facture surface. (a) Image of the fracture surface showing both brittle and ductile crack propagation, with the former within the proton irradiated region. (b) Image of the ductile fracture surface within the non-irradiated region below approximately 20 μm.

Two types of cracks have been observed in the proton irradiated 309L portion of tensile specimens pulled to failure in BWR NWC hot water. First, external cracks that are clear in SEM images of the free surface such as Figure 41. We associate these cracks with IASCC since we believe they initiate at the free surface. The second type of crack are internal and associated with γ–δ phase boundaries and $Cr_{23}C_6$ precipitation. These cracks cannot be due to corrosive attack. We believe these internal cracks are a consequence of residual stress, the applied tensile load, and intergranular $Cr_{23}C_6$ carbide precipitates at the γ–δ phase boundaries. We analyze both types of cracks below.

A FIB lift out in the vicinity of a surface crack in the irradiated portion of the 309L butter is shown in Figure 43. This lift out was taken from the region in left-most region of Figure 41b where extensive cracking and slip band formation occurred. This crack has been partially filled with redeposited Pt during the FIB lift out procedure. Secondary cracks are also evident and analyzed below. This region of the irradiated butter has a duplex microstructure.

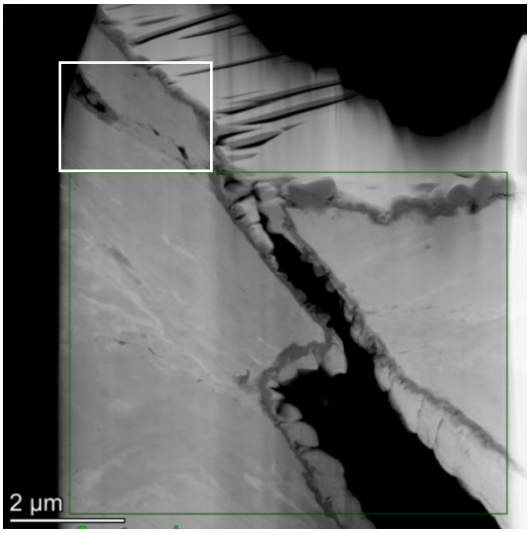

Figure 43. STEM-HAADF image of a FIB lift out of a surface crack in irradiated 309L. The crack has been partially filled with redeposited material during the FIB procedure. The Pt capping layer is seen along the free surface. The red box outlines the STEM-EDS elemental mapping that was performed. The white box outlines a secondary crack analyzed below.

STEM-EDS has been performed to map the elemental distribution associated with the crack shown in Figure 43 and are shown in Figure 44. The phases are labeled in Figure 44c, the Cr map, and both γ and δ phases are identified. This region of the irradiated 309L butter therefore has a duplex microstructure. The primary crack in this image is along the δ–δ grain boundary that intersects the free surface. STEM EDS analysis of the post-irradiated 309L butter presented above indicates Cr depletion these grain boundaries. Secondary cracking is observed along internal γ–δ phase boundaries. We analyze secondary cracking below. A few observations can be made regarding the primary crack. First, extensive re-deposition occurred. This is clearly identified by the Pt layer on the crack surface. The only way this element can reach the crack surface is by re-deposition during FIB thinning. The re-deposition of Cr and Fe also occurred and is part of the Pt-containing layer coating the crack surface. The original crack nucleation site is presumed to be a δ–δ grain boundary that intersected the free surface, although Figure 44 is not proof of this. In fact, it is possible the crack initiated below the free surface since the larger crack opening is further from the free surface. However, this could be a consequence of the orientation of the crack relative to the FIB lift out.

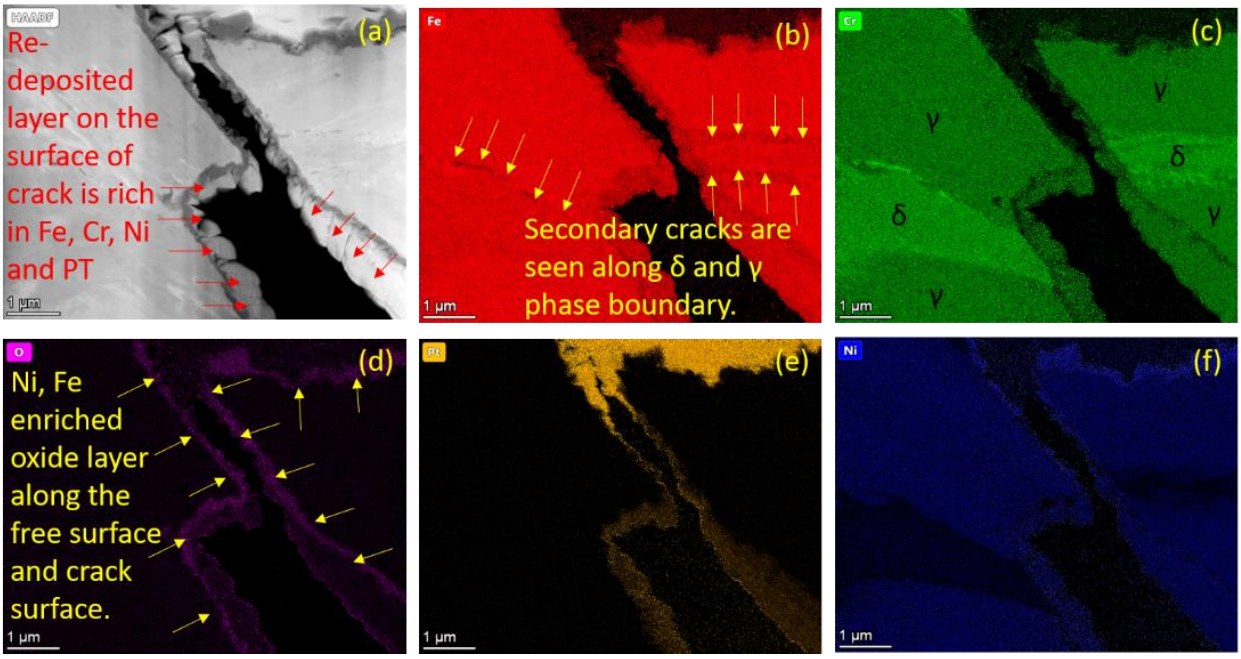

Figure 44. (a) STEM-HAADF micrograph of region identified in Figure 43; (b) Fe map; (c) Cr map; (d) O map; (e) Pt map; (f) Ni map. This crack intersected the free surface and re-deposition occurred during FIB thinning. Secondary cracking along γ–δ phase boundaries are observed and appear to be associated with $Cr_{23}C_6$ precipitates.

Secondary cracking is identified in Figure 44b. We isolate one set of these secondary cracks in Figure 45. The location of this map is shown as the white box in Figure 43. STEM EDS analysis shows that two secondary cracks propagated along the γ–δ phase boundaries of a δ particle embedded within a γ grain. Chromium rich precipitates are observed along these phase boundaries.

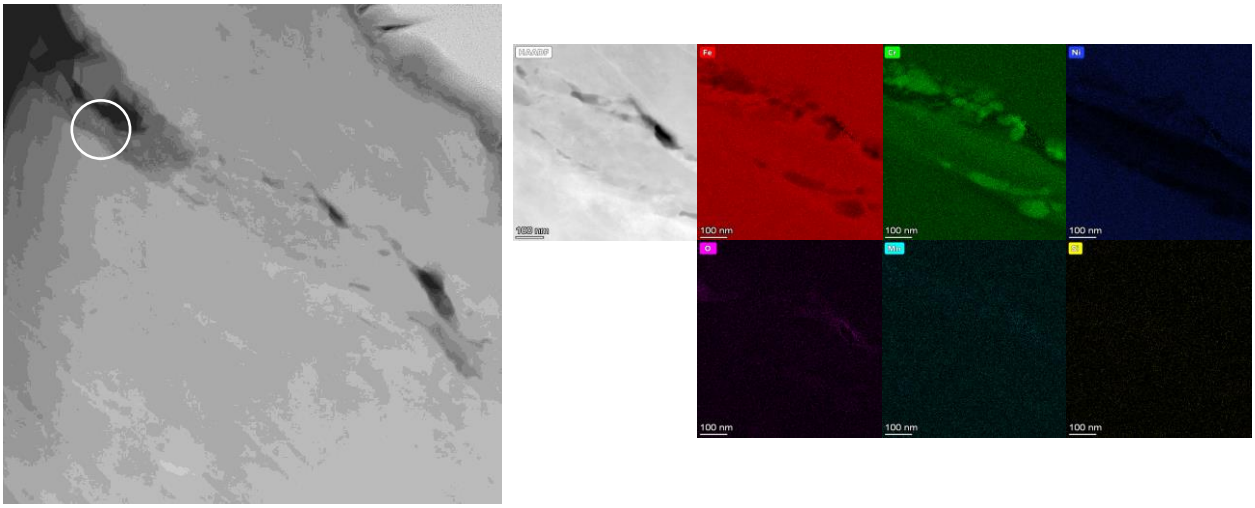

Figure 45. (left) HAADF image of the secondary crack identified in Figure 43. This secondary crack branched off of the primary crack and intersected the free surface. As a consequence oxides formed from exposure to the autoclave BWR NWC environment. No re-deposition occurred at this crack during FIB thinning. (right) STEM EDS element maps of the central portion of the secondary crack.

Line scans have been performed to analyze the local chemistry associated with the secondary cracks. We note the re-deposition of elements during FIB thinning prevents accurate STEM EDS elemental mapping of the primary crack. STEM EDS mapping of the region identified in Figure 45 by the white circle is shown in Figure 46. This analysis shows a layer on the crack surface that is composed of two oxides. The inner oxide layer is rich in Cr, while the outer oxide layer is rich in Fe and Ni and could be a spinel. The line scan profile indicates the inner oxide layer is thinner than the outer oxide layer. A second region of this secondary crack was analyzed and this is shown in Figure 47.

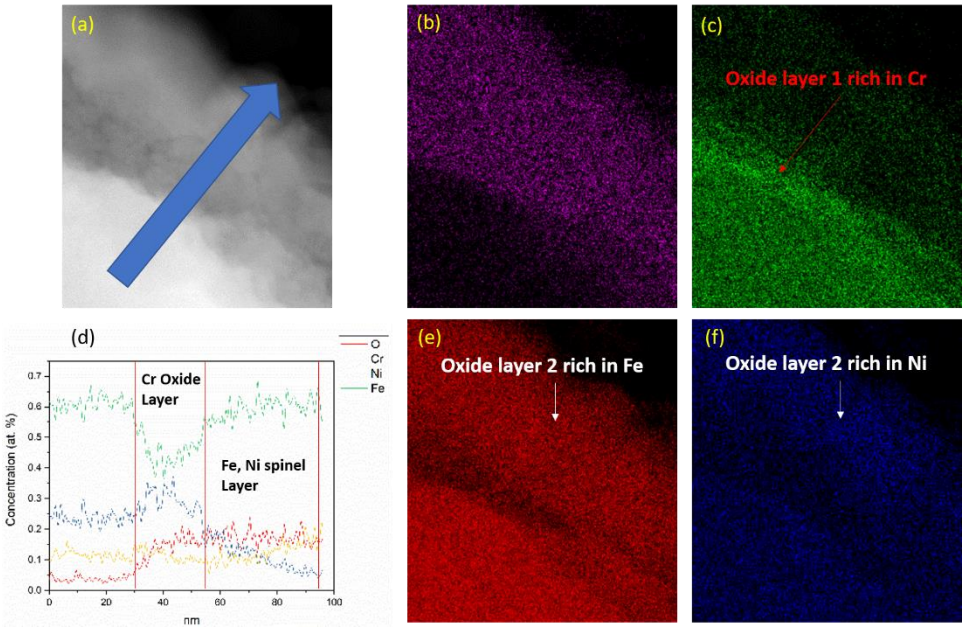

Figure 46. (a) STEM-HAADF of coating layer on the crack surface at higher magnification showing the line scan direction, (b) O map, (c) Cr map, (d) concentration profile along the line scan direction, (e) Fe map, (f) Ni map. The location of these maps is the white circle in Figure 45.

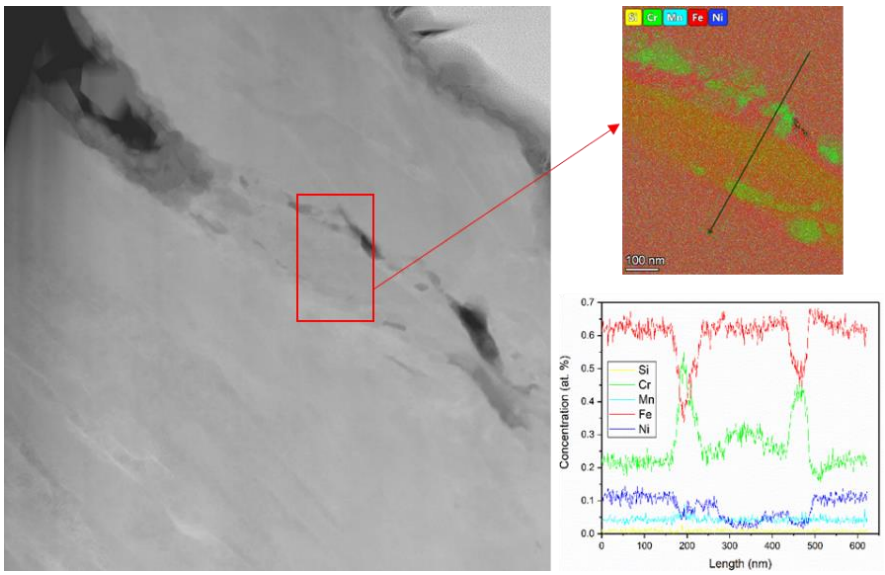

Figure 47. Line scan elemental profile across the two secondary cracks associated with the embedded δ particle.

Figure 48 captures the δ particle in the lower portion of Figure 44c. This δ particle is embedded in the γ matrix with phase boundary cracking that branches off of the primary crack. Intergranular $Cr_{23}C_6$ carbide precipitates are observed in the vicinity of the cracking. We believe this cracking may represent IASCC since the phase boundary intersects the large primary crack that then led to exposure to the autoclave BWR NWC environment.

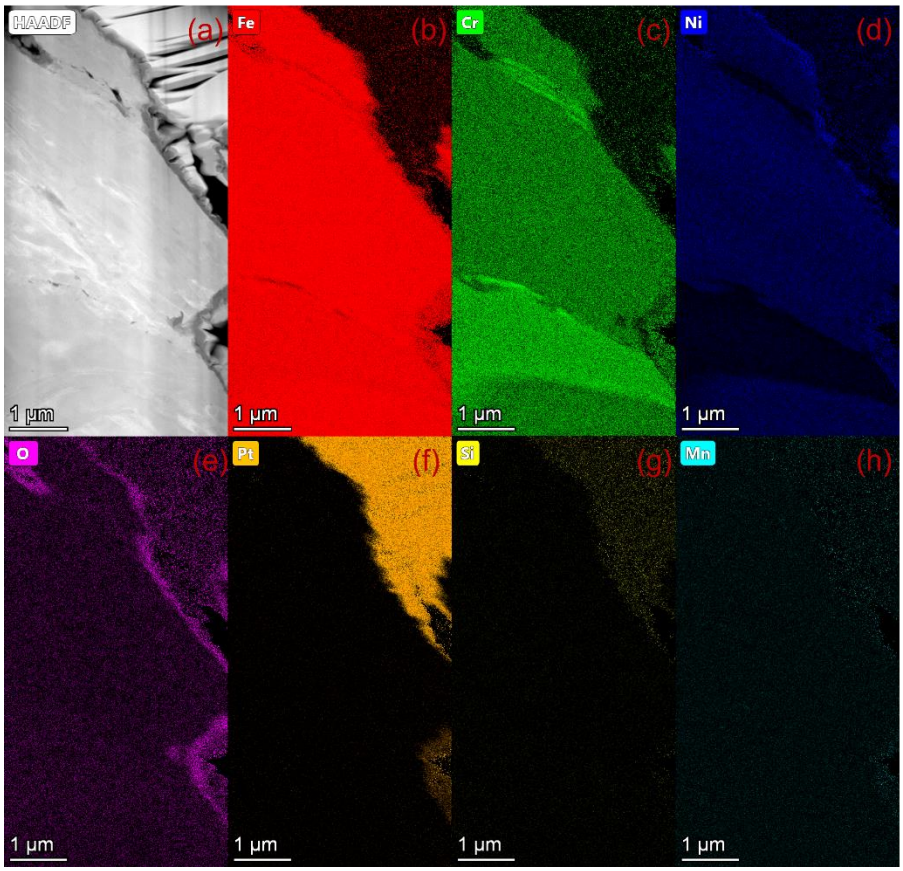

Figure 48. (a) STEM-HAADF micrograph of crack 309L butter, (b) Fe map, (c) Cr map, (d) Ni map, (e) O map, (f) Pt map, (g) Si map and (h) Mn map.

The second type of cracking observed in the 309L butter is within the proton irradiated region below the free surface—internal cracking we believe is associated with γ–δ phase boundaries and the $Cr_{23}C_6$ precipitates. This type of cracking, which cannot be attributed to corrosive attack since hot water exposure did not occur, is seen in Figure 49. STEM EDS elemental mapping of these cracks is shown in Figure 50. The large crack, while intragranular since it traverses the δ grain, likely initiated at the phase boundary where the $Cr_{23}C_6$ precipitates are seen.

We analyze the $Cr_{23}C_6$ precipitates in Figure 50 in Figures 51 and 12. High resolution TEM is used to calculate the diffraction patterns for both γ austenite and $Cr_{23}C_6$ precipitate. The known lattice parameters have a ratio of nearly three (1.066 nm $Cr_{23}C_6$ and 0.361 nm for γ austenite) and the FFT-generated diffraction patterns are consistent with this ratio.

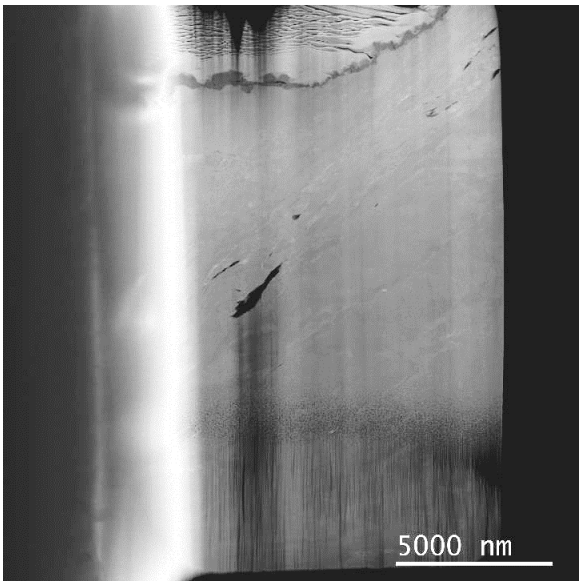

Figure 49. STEM-HAADF image of proton irradiated 309L area showing cracks initiated beneath the free surface.

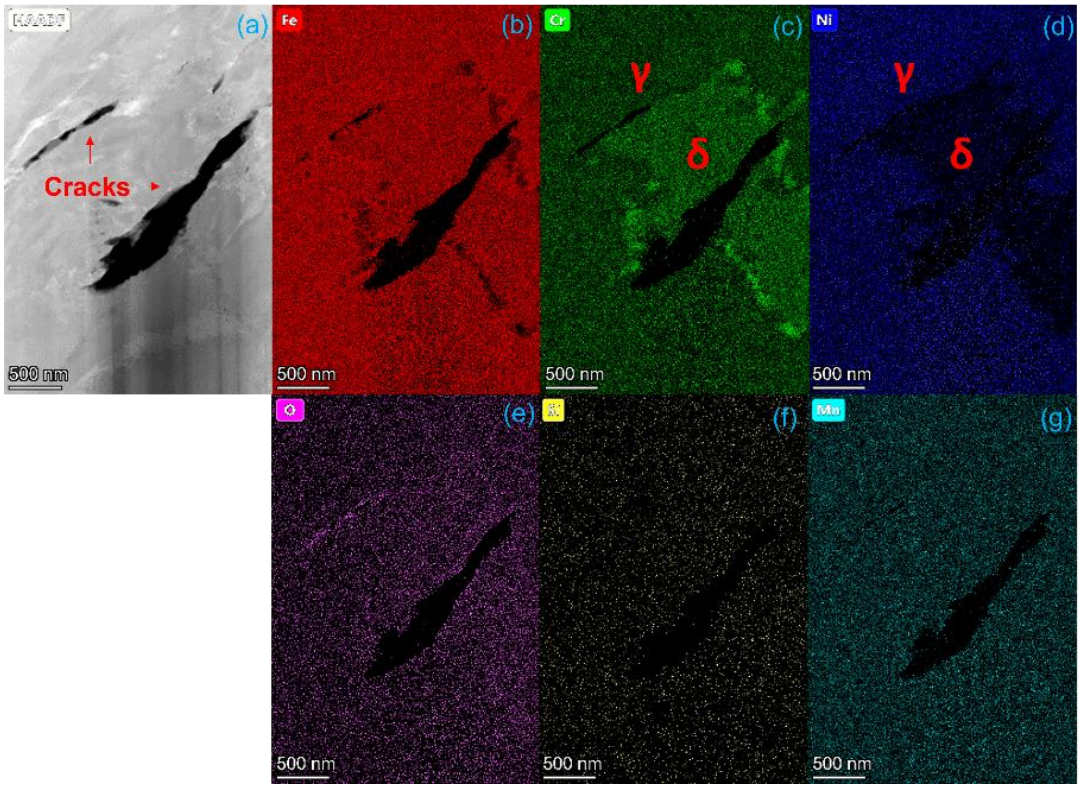

Figure 50. (a) STEM-HAADF micrograph of crack in 309L butter duplex region, (b) Fe map, (c) Cr map, (d) Ni map, (e) O map, (f) Si map and (h) Mn map. Cr-rich regions are observed along the γ–δ phase boundary. Note the lack of oxygen in (e).

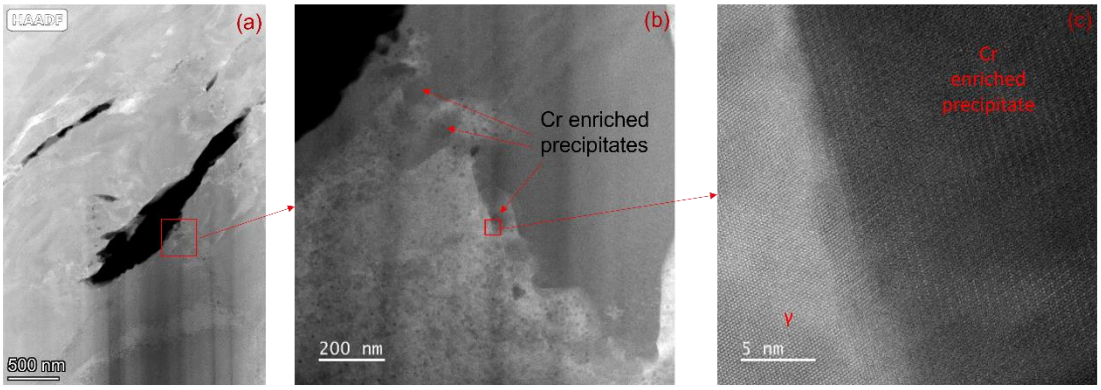

Figure 51. (a) STEM-HAADF micrograph of the same crack in Figure 50 but under higher magnification, (b) higher magnification of red boxed area in Figure 51a with $Cr_{23}C_6$ precipitates, and (c) atomic resolution HR-STEM of the red boxed area in Figure 51b showing the lattice structure $Cr_{23}C_6$ (right) and γ austenite (left).

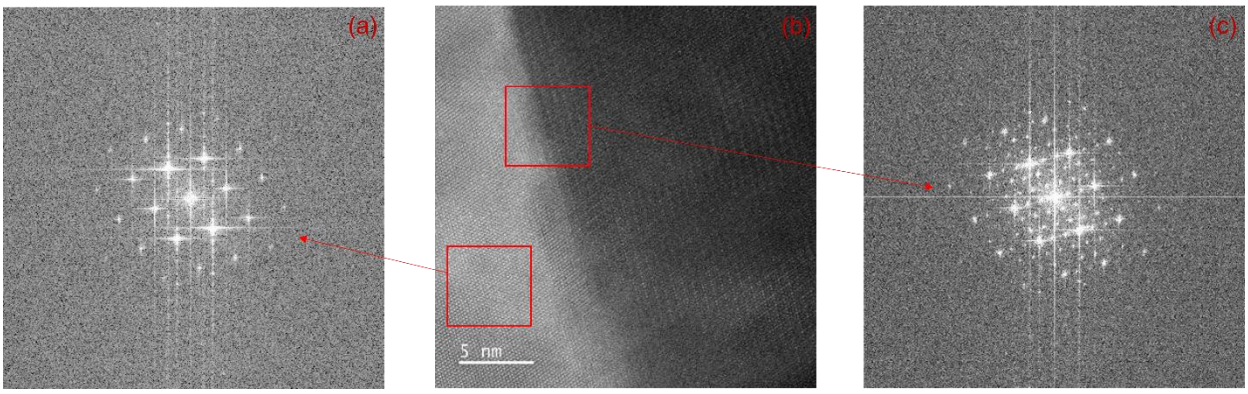

Figure 52. (a) FFT generated from the γ austenitic lattice, (b) atomic resolution HR-STEM of γ austenite and $Cr_{23}C_6$ precipitate used for the FFT (same as Figure 51c) and (c) FFT generated from the γ matrix and a $Cr_{23}C_6$ precipitate showing the lattices are commensurate with a lattice parameter ratio of three.

We believe two cracking mechanisms operate within the 309L butter during BWR NWC hot water immersion under applied tensile load based on analysis associated with Figures 44, 45, 47, and 50. The first mechanism is IASCC that initiates at the free surface and propagates along γ–γ grain boundary where RIS and Cr depletion is a factor. Similarly, IASCC along δ–γ phase boundaries within the duplex region of 309L occurs. We observe elemental redistribution at these phase boundaries (Cr depletion in Figure 23c) as well and this may be an influencing factor. Our experience with the chemical wash, that these phase boundaries were preferentially attacked, suggests susceptibility to SCC. The large residual stress in the 309L butter is likely an exacerbating factor. The second mechanism, the cause of internal cracking, cannot be attributed to SCC since hot water exposure did not occur. But we do attribute this to radiation damage via intergranular $Cr_{23}C_6$ carbide formation. We therefore believe this type of cracking is due to a combination of factors, including the large residual stress in the 309L butter, the presence of intergranular $Cr_{23}C_6$ carbides at the γ–δ phase boundaries and associated lattice strain, and the tensile applied load.

Bibliography for Sections 1-3

1. U.S. NRC, Expanded Materials Degradation Assessment (EMDA), NUREG/CR-7153, J.T. Busby, P.G. Oberson, C.E. Carpenter, and M. Srinivasan, 2014.
2. Zhong, W., Lin, J. L., Chen, Y., Li, Z., An, K., Sutton, B. J., & Heuser, B. J. (2021). Microstructure, Hardness, and Residual Stress of the Dissimilar Metal Weldments of SA508-309L/308L-304L. Metallurgical and Materials Transactions A, 52(5), 1927-1938.
3. Schaeffler, A.L., Constitution diagram for stainless steel weld metal. Metal Progress, 1949. 56(11): p. 680-680B.
4. Kou, S., Welding Metallurgy Second Edition. 2003, Hoboken, New Jersey: John Wiley & Sons, Inc.
5. Brooks, J. and A. Thompson, Microstructural development and solidification cracking susceptibility of austenitic stainless steel welds. International Materials Reviews, 1991. 36(1): p. 16-44.
6. Ziegler, J.F., The stopping and range of ions in matter, in http://srim.org/ 2013.
7. K. An, H. D. Skorpenske, A. D. Stoica, D. Ma, X.-L. Wang and E. Cakmak, "First in situ lattice strains measurements under load at VULCAN," Metallurgical and Materials Transactions A, vol. 42, pp. 95-99, 2011.
8. Li, Z., Zhan, X., Bai, X. M., Lee, S. C., Zhong, W., Sutton, B. J., & Heuser, B. J. (2021). Modified microstructures in proton irradiated dual phase 308L weldment filler material. Journal of Nuclear Materials, 548, 152825.
9. Zhen Li, Xun Zhan, Weicheng Zhong, Benjamin J. Sutton, Brent J. Heuser, Quantification of Precipitation, Clustering, and Void Formation in Proton Irradiated Dual Phase 308L Weldment Filler Materials, submitted Journal of Nuclear Materials, 2022.
10. Malis, T., S. Cheng, and R. Egerton, EELS log-ratio technique for specimen-thickness measurement in the TEM. Journal of electron microscopy technique, 1988. 8(2): p. 193-200.
11. A.L. Bowman, G.P. Arnold, E.K. Storms, and N.G. Nereson, The structure of $Cr_{23}C_6$, Acta Cryst. B28 (1972) 3102-3103.
12. Berkane, R., J. C. Gachon, J. Charles, and J. Hertz, A thermodynamic study of the chromium-carbon system, Calphad, 11(1987) 375-382.
13. Mansur, L., Theory and experimental background on dimensional changes in irradiated alloys. Journal of Nuclear Materials, 1994. 216: p. 97-123.

4. Computational Results

This section was written by Xianming Bai (VT) and Benjamin Spencer (INL). It was written as a standalone document with section, figure, table, and reference numeration independent of Sections 1-3. In lieu of renumbering all sections, figures, tables, and references, which would likely lead to errors, the PI has chosen to keep the document as is.

1. Theoretical explanation of G phase formation in BCC and FCC Fe using Density functional theory (DFT) calculations

In our proton irradiation experiments, it is found that $Mn_6Ni_{16}Si_7$ G phase only forms in body-centered-cubic (BCC) δ ferrite but not in face-centered-cubic (FCC) γ austenite in the duplex 308L stainless steel under proton irradiation. Previously, Chen et al. [1] reported that in thermally-aged CF8 cast austenitic stainless steels in which both δ ferrite and γ austenite exist, the G-phase precipitates were only observed in δ ferrite. Upon heavy-ion irradiation, new G-phase precipitates were observed in δ ferrite matrix but not in γ austenite. Recently, Lin et al. [2] also reported that Mn-Ni-Si rich G phase formed in δ ferrite but not in γ austenite in proton-irradiated 308L. In addition, G phase formation was also observed in thermally treated ferritic steels [3]. These experimental studies suggest that G phase may be energetically more favorable to form in Fe based alloys with a BCC structure (that is, α and δ ferrite) than those with a FCC structure (γ austenite), although this hypothesis has never been proven to our best of knowledge. Here density functional theory (DFT) modeling is used to calculate the interface energies of both G/Fe_{BCC} and G/Fe_{FCC} interfaces, providing a theoretical explanation of the experimental observations.

To provide a theoretical explanation of our experimental observation, DFT calculations were conducted to calculate the interface energies between the G-phase ($Mn_6Ni_{16}Si_7$) and Fe, where both BCC and FCC Fe are considered. $Mn_6Ni_{16}Si_7$ G-phase has a cubic structure (space group: $Fm\bar{3}m$) and one unit cell contains 116 atoms ($Mn_{24}Ni_{64}Si_{28}$) [4]. The lattice parameter (1.112 nm [4]) is about 4 times of BCC Fe and 3 times of FCC Fe. Therefore, to create a G-phase/Fe_{BCC} interface system, a BCC Fe box of 4×4×4 unit cells (128 Fe atoms) is placed on a G phase unit cell along the [001] direction so that the entire system contains 244 atoms. Similarly, to create a G-phase/Fe_{FCC} interface system, a FCC Fe box of 3×3×3 unit cells (108 Fe atoms) is placed on a G phase unit cell along the [001] direction and the total number of atoms is 224. Since periodic boundary conditions are employed, two interfaces are created in each system. The interface energy is thus calculated as,

$$\sigma_{G/Fe} = \frac{E_{G/Fe} - E_G - E_{Fe}}{2A}, \quad (1)$$

where $E_{G/Fe}$ is the total energy of the interface system, E_G is the energy of a standalone bulk G-phase, E_{Fe} is the energy of a standalone bulk Fe that has the same structure and number of atoms as in the interface system, and A is the interface area.

It is well known that BCC α-Fe is stable at low temperatures and has a ferromagnetic (FM) state below the Curie temperature, FCC γ-Fe is stable at moderate temperatures and has a paramagnetic (PM) state, and BCC δ-Fe is stable at high temperatures. The magnetic state of δ-Fe is likely to be paramagnetic. It is well known that δ-Fe is stable at the high temperature range (>1653 K), which is well above the Curie point of Fe (1043 K). The magnetic state of Fe changes from ferromagnetic to paramagnetic above the Curie point and it is reasonable to assume that δ-Fe is in a PM state. It is possible that δ-Fe has a non-magnetic (NM) state as well. In this work, both non-magnetic (NM) and PM states are considered for δ-Fe to distinguish α-Fe and δ-Fe. For comparison purpose, the FM α-Fe result (supported by another project) is also included. For the $Mn_6Ni_{16}Si_7$ G-phase, neutron diffraction experiments [4] show that the magnetic state is complex and temperature dependent, and is dominated by the magnetic moment of Mn. In this work, the $Mn_6Ni_{16}Si_7$ G-phase is treated as FM state, which is the same approach used by King *et al*. [5]. In addition, NM state is also considered for $Mn_6Ni_{16}Si_7$ G-phase to account for the loss of magnetism at high temperatures. Therefore, combinations of different magnetic states between Fe and G-phase are considered for calculating the interface energies, as detailed below.

All the DFT calculations are conducted using the Vienna Ab initio Simulation Package (VASP). During structural relaxation of simulation systems, both the simulation cell and shape as well as atom positions are allowed to change. The Projector-Augmented-Wave (PAW) method [6] is used and the plane wave cutoff energy is set to 450 eV. The electron exchange-correlation interactions are modeled under the generalized gradient approximations (GGA) using the standard Perdew–Burke–Ernzerhof (PBE) functionals [7] implemented in the VASP 5.4. Gaussian smearing with a smear width of 0.05 eV is used to set the partial occupancies of orbitals. The energy convergence criterion is 10^{-4} eV in all simulations. In most of the simulations, the force convergence of 0.01 eV/Å is also used. The spin polarization effect is activated when the magnetic effects are modeled. For FM state, the initial magnetic moment is set to $5\mu_B$ for Fe, and $6\mu_B$ for Mn. To approximate the PM state for both BCC and FCC Fe, the initial magnetic moments of Fe atoms are randomly distributed between $-3\mu_B$ and $3\mu_B$ with a mean value of $0\mu_B$. In all simulations, a 3×3×3 gamma-centered grid is used for k-point mesh. As described above, we considered different magnetic states for G/Fe interfaces. Three scenarios are considered: 1) both Fe and G phase are non-magnetic (NM), 2) both Fe and G phase are ferromagnetic (FM), and 3) Fe is a paramagnetic (PM) and G

phase is ferromagnetic (FM). In each of these three scenarios, both BCC and FCC Fe are modeled. Therefore, a total of six different types of interface systems with different magnetic states and Fe phases are modeled.

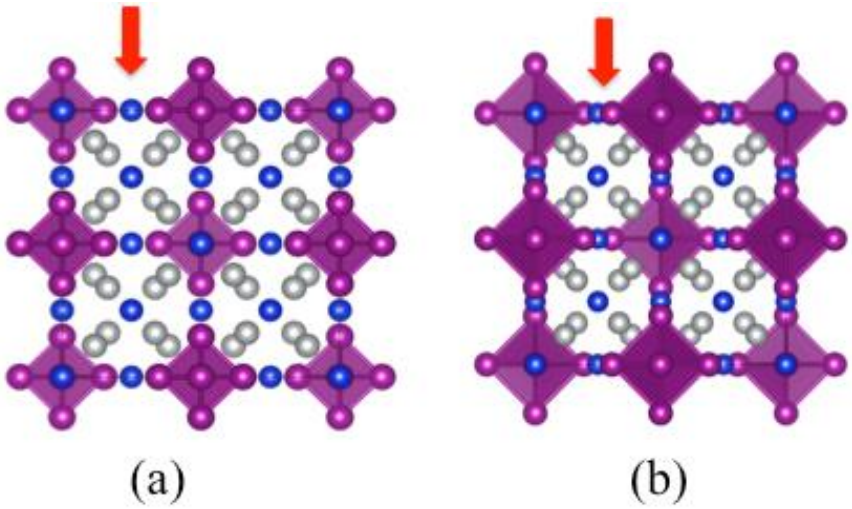

Figure 1. Relaxed crystal structures of $Mn_6Ni_{16}Si_7$ G phase for two different magnetic states. (a) Non-magnetic and (b) Ferromagnetic. Purple spheres – Mn atoms; Blue spheres – Si atoms; Grey spheres – Ni atoms. The arrows indicate the discrepancy between two relaxed structures.

To use Equation (1) to calculate the interface energies, the energies of bulk BCC Fe, FCC Fe, and $Mn_6Ni_{16}Si_7$ G phase of the same magnetic states as in the interface systems are needed. For G phase, both NM and FM states are modeled. The relaxed structures are shown in Figure 1. The structures based on the two magnetic states are similar, although slight discrepancy can be seen regarding the Mn and Si arrangements between two neighboring polyhedrals, as indicated by the red arrow in each figure. It should be noted that the structure based on the FM state (Figure 1b) agrees very well with the refined structure from neutron diffraction experiments [4]. The predicted lattice parameter is 10.98 Å for the NM state and 11.10 Å for the FM state in this work. The latter is in very good agreement with the experimental value of 11.12 Å at 4 K [4] and previous DFT result of 11.10 Å [4]. In addition, the energy of the G phase in the FM state is about 2.89 eV per $Mn_6Ni_{16}Si_7$ formula unit lower than that in the NM state. Therefore, the G phase in the FM state is more consistent with the experimental results than the NM state.

Table 1. DFT results of BCC Fe and FCC Fe of different magnetic states. The systems highlighted in bold are relevant to the three Fe phases (α, γ, δ) in observed in the equilibrium phase diagram.

Fe structure and magnetic state	**Fe phase**	**a_0 (Å)**	**Energy relative to α phase (eV/atom)**
BCC-FM (ground state)	**α (FM)**	**2.83 (Exp: ~2.86 [8])**	**0**
BCC-NM	δ (NM)	2.76	0.472
BCC-PM	**δ (PM)**	**2.83 (Exp: 2.83, this work)**	**0.169**
FCC-NM	γ (NM)	3.45	0.160
FCC-FM	γ (FM)	3.63	0.152
FCC-PM	**γ (PM)**	**3.49 (Exp: 3.53, this work)**	**0.133**

Three magnetic states are modeled for each of BCC and FCC Fe: NM, FM, and PM. The lattice parameter (a_0) and the relative energy with respect to the ground state Fe for each configuration is shown in Table 1. For BCC Fe in the FM state (BCC-FM), which is the ground state and represents α-Fe, the predicted lattice parameter a_0 = 2.83Å is in good agreement with the experimental value of 2.86Å [8]. For non-magnetic BCC Fe (BCC-NM), the predicted lattice parameter a_0 = 2.76Å is smaller than that of α-Fe and the energy is significantly higher (0.472 eV/atom) than α-Fe. For BCC Fe in the PM state (BCC-PM), which is considered to be the δ-Fe surrogate in this work, the predicted lattice parameter a_0 = 2.83Å is identical as our experimental value of 2.83Å. The energy is slightly higher (0.169 eV/atom) than α-Fe. FCC Fe in the PM state (FCC-PM) represents the γ-Fe in this work and the predicted lattice parameter is a_0 = 3.49Å, which is close to our experimental value of 3.53Å. The energy for this structure is slightly higher than α-Fe by 0.133 eV/atom, but is lower than that of δ-Fe. For FCC in NM (FCC-NM) and FM (FCC-FM) states, the predicted a_0 is either lower or higher than the experimental value of γ-Fe, and the respective energies are also slightly higher than the γ-Fe in the PM state. The lattice parameters simulated with DFT are listed in Table 1. Overall, our DFT modeling predicts that the phase order is α (FM) < γ (PM) < δ (PM)

based on eV/atom energies, which is consistent with the experimentally observed stability sequence ($\alpha \rightarrow \gamma \rightarrow \delta$) as the system temperature is increased. These phases are highlighted in bold in Table 1.

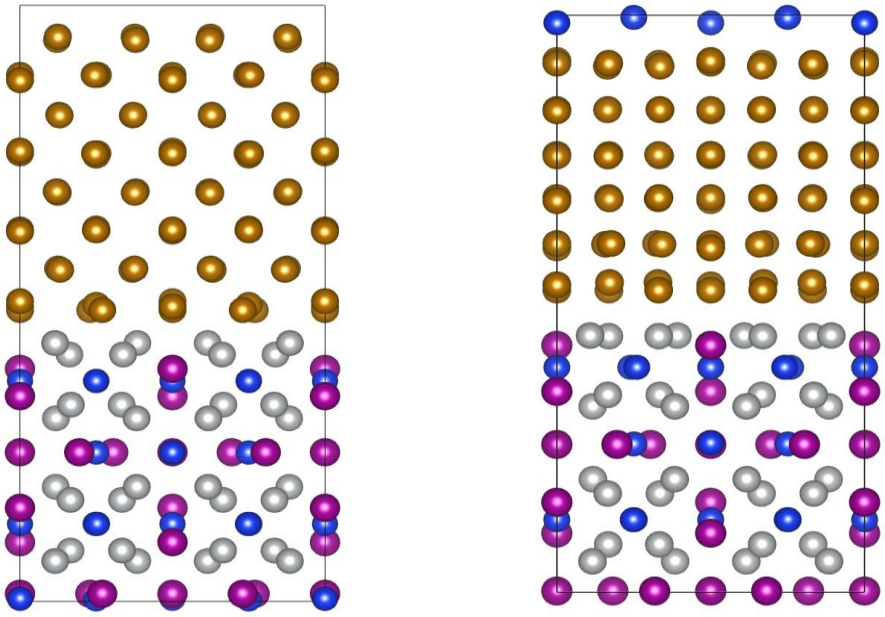

Figure 2. Relaxed interface structures of a) G phase + BCC Fe and b) G phase + FCC Fe. In both cases, the G phase is ferromagnetic and the Fe phases are approximately paramagnetic upon relaxation. Periodic boundary conditions are used so that some atoms wrap back between top and bottom of the system in (b). Yellow spheres: Fe atoms; Purple spheres – Mn atoms; Blue spheres – Si atoms; Grey spheres – Ni atoms.

The G/Fe interface energies for different combinations of magnetic states and Fe crystal structure are calculated using Equation (1) and the results are listed in Table 2. Two representative interface structures, G/Fe_{BCC} and G/Fe_{FCC}, are shown in Figure 2 for illustration. For Case 1 in which both Fe and G phase are non-magnetic (note the reference systems are also non-magnetic for interface energy calculation), the interface energy of G/Fe_{BCC} is -1.06 J/m^2, while that of G/Fe_{FCC} is 1.14 J/m^2. The negative G/Fe_{BCC} interface energy seems surprising because an interface made of the same material (e.g., grain boundaries) always has a positive energy. However, for a heterogeneous interface made of dissimilar materials such as θ–Al_2O_3 + water, a negative interface energy has been reported experimentally [9] because of the chemical reaction and formation of new

bonds between dissimilar materials [10]. The negative interface energy means that the formation of such a heterogeneous interface is an exothermic process and the resulting interface bonds are very strong [10]. Therefore, the negative interface energy of the non-magnetic G/Fe_{BCC} is likely due to the strong chemical effect at this heterogeneous interface. It also suggests that the precipitation of G interface in a BCC Fe matrix, if both are non-magnetic, is a spontaneous process. On the other hand, nucleation of the G phase in a FCC Fe matrix, if both are non-magnetic, has to overcome the large positive interface energy.

Table 2. DFT results of interfacial energies for the six combinations of FCC Fe, BCC Fe, and the G phase of different magnetic states. The systems highlighted in bold are relevant to the three Fe phases (α, γ, δ).

Initial magnetic state	**Final magnetic state**	**Represented Fe Phase**	**Interface energy (J/m^2)**
Both NM	BCC + G, NM	δ (NM)	-1.06
	FCC + G, NM	γ (NM)	1.14
Both FM	**BCC + G, FM**	**α (FM)**	**0.68**
	FCC + G, FM	γ (FM)	0.84
NM Fe + FM G	**PM BCC + FM G**	**δ (PM)**	-2.22 (Ref: NM BCC Fe, lower limit) **0.35 (Ref: PM BCC Fe)** 0.66 (Ref: PM FCC Fe, upper limit)
	PM FCC + FM G	**γ (PM)**	1.05 (Ref: NM FCC Fe) **1.25 (Ref: PM FCC Fe)**

For Case 2 in which both Fe and G phase are ferromagnetic (note the reference systems are also ferromagnetic), the interface energy of G/Fe_{BCC} is 0.68 J/m^2, while that of G/Fe_{FCC} is 0.84 J/m^2.

Again, the interface energy between BCC Fe and the G phase is lower compared to FCC Fe and the G phase, although the difference is small. Note here the ferromagnetic G/Fe_{BCC} interface can be related to the precipitation of G phase in a ferritic α-Fe matrix. This interface energy is moderate so that the formation of G phase in a ferritic α-Fe is possible. This prediction is consistent with some experimental observations of G phase formation in ferritic Fe-based steels upon heat treatment [3].

To model the more complex Case 3 in which Fe is a paramagnetic and G phase is ferromagnetic, the initial interface system consists of a non-magnetic BCC or FCC Fe and a ferromagnetic G phase. Since the spin polarized DFT is used, BCC or FCC Fe atoms gain some magnetic moments automatically after relaxation. The magnetic moments of these Fe atoms are either positive or negative and the magnitudes vary significantly. Therefore, the magnetic states of BCC and FCC Fe in the interface system upon relaxation can be approximated as the paramagnetic state, as we do for bulk BCC δ-Fe (PM) and FCC γ-Fe (PM). To calculate the interface energies, both non-magnetic and paramagnetic Fe are considered as the reference systems to check how the interface energy is sensitive to the magnetic state of Fe. When the non-magnetic BCC Fe is used as a reference system, which is the initial condition of Fe before the interface is relaxed, the calculated G/Fe_{BCC} interface energy is −2.22 J/m^2, a very low value due to the high energy of BCC-NM Fe (Table 1). This value can be considered as a lower limit of the interface energy for G/Fe_{BCC} since the magnetic states of Fe in the relaxed interface system are not exactly the same as in the reference bulk Fe. When the paramagnetic BCC Fe is used as a reference system, which is close to the final state of Fe after the interface is relaxed, the calculated G/Fe_{BCC} interface energy is 0.35 J/m^2. As the Fe is in a nearly paramagnetic state in this relaxed interface system, this interface energy is the most relevant case to the G phase precipitation in δ-Fe observed in our experiments. Since FCC-PM γ-Fe is more stable than BCC-PM δ-Fe and the former has a lower energy than the latter (Table 1), we also can use the energy (per atom) of FCC-PM γ-Fe as the reference energy to determine the upper limit of the G/δ-Fe interface energy. The calculated value is 0.66 J/m^2, as shown in Table 2. For the interface energy between FCC Fe and paramagnetic G phase (G/Fe_{FCC}), the calculated value is 1.05 J/m^2 if the non-magnetic FCC Fe is used as the reference system, and 1.25 J/m^2 if the paramagnetic FCC Fe is used as the reference system. The difference is not as significant as for the G/Fe_{BCC} interface. The latter value (1.25 J/m^2) can be considered to be the interface energy for a G phase precipitation in the γ-Fe. Comparing the interface energy between G/Fe_{BCC} and G/Fe_{FCC} in Case 3, the G/Fe_{BCC} always has a much lower interface energy, even at the upper limit.

Table 2 lists the interface energies for different combinations of G phase and Fe. Regardless of which magnetic state is assumed, the G/Fe_{BCC} interface energy is always lower than that of G/Fe_{FCC}. Considering the known magnetic states in α, γ, and δ Fe, the interface energy should be 0.68 J/m^2 for α/G, 1.25 J/m^2 for γ/G, and 0.35 J/m^2 for δ/G. These interface energies are highlighted in bold in Table 2. Therefore the interface energy in δ-Fe is smallest and that in γ-Fe is largest. If δ-Fe and γ-Fe phases coexist in steels, such as in 308L studied in this work, the G phase will preferentially precipitate in δ-Fe rather than in γ-Fe based on interface energy considerations. Therefore, our DFT calculations provide a thermodynamics-based explanation for the preferential precipitation of the G phase in δ ferrite but not in γ austenite. This conclusion holds for both in our experiments as well as other observations in the published literature [1].

For comparison we can calculate the bulk strain energy associated with misfit interfacial lattice strain u_{coh} given by,

$$u_{coh} = 2\mu\left(\frac{1+\upsilon}{1-\upsilon}\right)h\varepsilon^2, \qquad (2)$$

where μ is the shear modulus, ν is Poisson's ratio, h is the thickness, and ε is the misfit strain. The multiplication by h leads to units of energy per area [11]. The shear modulus (91, 81, and 80 GPa) and Poisson's ratio (0.28, 0.33, and 0.31) values were used for the G-phase, γ-austenite, and δ-ferrite, respectively. Equation (2) is derived assuming two cubic lattices oriented along the [100] direction, as is the case here. The misfit strains between the G-phase lattice and either FCC-γ or BCC-δ lattice are 0.012 and -0.053, respectively, using our measured lattice parameters of the two phases. The misfit strain dominates the comparison since the elastic properties of the three systems do not differ significantly. We use the G-phase supercell thickness, corresponding to one unit cell, for h. The bulk strain energies are 0.05 and 0.92 J/m^2 for the G-phase//γ and G-phase// δ, respectively. An alternative estimation of the bulk strain energy can be obtained by a simple integration of Hooke's Law assuming completely elastic behavior. This leads to an equation similar to Eq. (2), but reduced by a factor of 2/(1-ν). The corresponding to bulk strain energies are 0.02 and 0.07 J/m^2 for the G-phase// γ and G-phase// δ, respectively. It is not surprising that misfit strain energy would favor precipitation in the austenitic phase given the lower lattice misfit. However, the electronic/magnetic factors captured by the DFT computations must govern the observed precipitation. We note also that the DFT computations implicitly include lattice misfit strain effects since the interfacial coherency was maintained in the supercell.

We also note that the self-diffusivity in BCC is significantly larger (around 100 times larger) than in FCC [12-15]. Therefore the kinetics may also play a role on the G phase formation in δ ferrite, although the radiation-enhanced diffusion could provide sufficient diffusion kinetics of G-phase elements in both δ ferrite and γ austenite. As mentioned earlier, actually G phase formation was observed in ferritic α-Fe matrix [3], even though α-Fe has a lower self-diffusivity than δ-Fe [16] and possibly γ-Fe as well. The interface energy in α-Fe is moderate (0.68 J/m^2) according to our DFT calculations so precipitation of G phase in α-Fe is thermodynamically possible. Therefore, we believe the interface energy plays a major role in determining if G phase can precipitate in different Fe phases.

2. Molecular dynamics calculations of GB strength in Ni-based and Fe-based oxides

Grain boundaries (GBs) in Ni-based and Fe-based alloys are prone for corrosion. The intergranular corrosion lowers the GB strength and therefore may lead to stress corrosion cracking (SCC). When GBs are fully oxidized, the formed oxides include NiO in Ni-based alloys and Fe_2O_3 in Fe-based alloys. In this project, we first use molecular dynamics (MD) simulations to understand the role of oxidation on the GB cohesive strength. For MD simulations, a reliable interatomic potential is essential for modeling the oxide structure. Therefore it is important to evaluate the existing interatomic potentials for both NiO and Fe_2O_3. The interatomic potentials for oxides typically are Buckingham + Coulomb type. In such a potential, the interaction energy between ions i and j at a distance of r_{ij} has the form,

$$V(r_{ij}) = \frac{1}{4\pi\varepsilon_0}\frac{q_i q_j}{r_{ij}} + \left[A_{ij}e^{(-r_{ij}/\rho_{ij})} - \frac{C_{ij}}{r_{ij}^6}\right], \qquad (3)$$

where the first term is the Columbic term, q_i and q_j are the ionic charges of ions i and j respectively, and ε_0 is vacuum permittivity; the second term is the Buckingham term with A_{ij}, ρ_{ij} and C_{ij} being the Buckingham potential parameters.

Table 3. Potential parameters for NiO [17].

	A_{ij} (eV)	ρ_{ij} (Å)	C_{ij} (eV/Å^6)
Ni-Ni	0.0	3.0	0.0
Ni-O	641.2	0.337	0.0
O-O	22760	0.149	35.71

The NiO potential parameters [17] are shown in the Table 3. NiO has a rock salt structure and its space group is $Fm\bar{3}m$. The Ni and O ions have +2 and -2 normal charges, respectively. The evaluation of the NiO potential is conducted with the LAMMPS software [18]. The cutoff distance for the potential is set to 12 Å. The equilibrium lattice constant is obtained by finding the minimum energy with a set of initial lattice constants. The final result is a_{NiO} = 4.164 Å, which is very close to the result of 4.168 Å from Ref. [17]. The elastic constants are calculated by stress-strain method. Table 4 lists the elastic constants for NiO calculated in this work. The results agree well with the literature results, indicating the potential parameters are correctly implemented.

Table 4. Elastic constants for NiO calculated from the MD simulations using the empirical potential [17].

	C11 (GPa)	**C12 (GPa)**	**C44 (GPa)**
This work	262.58	172.25	173.56
Literature [17]	265.70	172.90	172.90

Using this empirical potential, three grain boundaries (GB) in NiO are studied: Σ3(111), Σ5(210), and Σ5(310). Each GB contains around 4000 atoms. The minimum-energy GB structure is obtained by the gamma surface mapping method. In this gamma surface mapping method, the top grain is shifted along a 2-D grid in the GB plane, with a typical grid size of 0.2 Å. At each grid point, the GB structure is minimized. The final minimum-energy structures of three GBs are shown in Figure 3. Their GB energies are shown in Table 5.

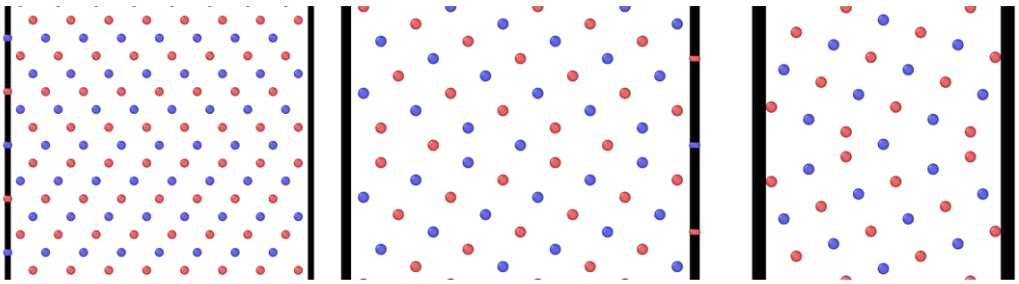

Figure 3. Three minimum-energy GBs in NiO (Σ3(111), Σ5(210), Σ5(310)) obtained through the gamma surface mapping method in MD. The blue and red spheres represent Ni and O atoms respectively.

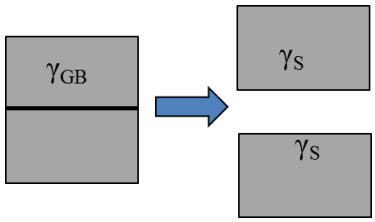

Figure 4. Schematic of using a GB fracture model for calculating the GB strength.

For these NiO GBs, we calculate their GB cohesive strength. The GB cohesive strength (γ^0) is defined as the minimum energy needed to fracture a GB into two free surfaces, as schematically shown in Figure 4. Therefore, it is related to the energy of the free surface (γ_S) and the grain boundary energy (γ_{GB}),

$$\gamma^0 = 2\gamma_S - \gamma_{GB}. \qquad (4)$$

The factor of 2 in Equation (4) is due to the formation of two equivalent free surfaces after the fracture. To calculate the surface energy of the same crystallographic orientation as a GB, a 100 Å vacuum distance is added in the simulation box to create two free surfaces. The system is annealed at a high temperature first then minimized at 0 K to avoid the meta-stable structures. The results are shown in Table 5. For the Σ3(111) GB, the GB energy is lowest, because it is a coherent twin GB. Its surface energy, however, is the highest. Therefore, this GB has the highest cohesive strength.

For the Σ5(210) GB, both the GB energy and surface energy are moderate. The cohesive strength is also moderate. Interestingly, the GB energy of the Σ5(310) GB is higher than the surface energy of (310). The GB cohesive strength is lowest, only about 1.06 J/m^2. The MD results suggest that the Σ5(310) GB in NiO is very brittle while the Σ3(111) GB is very strong. However, further experimental measurement or DFT modeling is needed to validate this prediction based on the empirical potential.

Table 5. GB energies, surface energies, and GB cohesive strength for three GBs in NiO predicted by the MD simulations using an empirical potential.

NiO	**Σ3(111)**	**Σ5(210)**	**Σ5(310)**
$\boldsymbol{\gamma_{GB}}$ **(J/m^2)**	0.878	1.2706	1.8847
$\boldsymbol{\gamma_S}$ **(J/m^2)**	3.069	1.7481	1.4716
$\boldsymbol{\gamma^0}$ **(J/m^2)**	5.26	2.2256	1.0585

Table 6. Potential parameters for Fe_2O_3 [19, 20].

	Charge	**A_{ij} (eV)**	**ρ_{ij} (Å)**	**C_{ij} (eV/Å^6)**
Potential 1 [19]				
Fe-Fe	+3 for Fe	0.0	3.0	0.0
Fe-O		1102.40	0.3299	0.0
O-O	-2 for O	22764.0	0.1490	27.88
Potential 2 [20]				
Fe-Fe	+1.4175 for Fe	0.0	3.0	0.0
Fe-O		8020.285	0.190	0.0
O-O	-0.945 for O	9022.821	0.265	85.092

The interatomic potentials for Fe_2O_3 are also evaluated. Two potentials for Fe_2O_3 are evaluated: Potential 1 developed by de Leeuw et al. [19] and Potential 2 developed by Ta et al. [20]. Similar to NiO, both potentials are Buckingham + Coulomb type. Potential 1 treats both Fe and O ions as fully charged while Potential 2 treats them partially charged. These potential parameters are listed in Table 6. The structure of α-Fe_2O_3 is hematite and its space group is $R3\bar{c}$. Since the crystal

structure for α-Fe_2O_3 is trigonal, there are two lattice constants: *a* and *c*. Here the equilibrium lattice constants are obtained by searching for the minimum energy state with different *a* and *a/c* values. The elastic constants are calculated using the same method as for NiO. The calculated lattice constants and elastic constants are listed in Tables 7 and 8, respectively. For lattice constants, the values predicted by the Potential 2 agree better with experimental values than by the Potential 1, as shown in Table 7. For elastic constants, both potentials have large discrepancies with the DFT results [21], although the Potential 2 has slightly better agreement with the DFT [21] than the Potential 1, as shown in Table 8. Overall, the Potential 2 predicts better material properties than the Potential 1, although none of them is very satisfactory. Therefore the GB strength in Fe_2O_3 is not calculated using these empirical potentials.

Table 7. Lattice constants for Fe_2O_3 predicted by two potentials.

Lattice constants	**a (Å)**	**c/a**
Potential 1 – this work	5.06	2.64
Potential 2 – this work	5.05	2.75
MD – literature [19]	5.06	2.64
Experiment [19]	5.04	2.73

Table 8. Elastic constants for Fe_2O_3 predicted by two potentials.

	C11	**C12**	**C13**	**C14**	**C33**	**C44**
Potential 1 –this work	506.12	201.22	145.87	44.90	402.56	126.81
Potential 2 –this work	266.23	107.10	102.77	6.32	279.29	60.61
DFT [21]	325.0±19.0	131.8±5.6	105.8±22.9	1.2±2.9	264.2±25.1	103.0±6.4

Although these empirical potentials can predict some reasonable properties of the oxide systems (e.g., lattice constants, elastic constants), they have inherent limitations. Both potentials are fixed-charge potentials so that the important charge transfer effect cannot be modeled by them. In addition, these potentials can only be used to model the perfectly stoichiometric oxide systems. During the GB oxidation process, metallic GBs do not transform to fully oxidized GBs instantly.

Before the metallic GBs are fully oxidized, they may contain some oxygen atoms to form partially oxidized GBs. These oxygen atoms may form some local ionic bonds with the surrounding metal atoms while other regions still maintain the metallic bonds. Even if the GBs are fully oxidized, the oxide/metal interface can have some significant charge transfer. These realistic scenarios cannot be captured by the empirical potentials studied here. Therefore, we concluded that the quantum-mechanics-based density functional theory (DFT) method is more suitable and accurate for modeling these GB oxidation problems because the charge transfer effect can be captured by DFT. As a result, the DFT method is selected to model the GB strengths of both partially and fully oxidized GBs, as well as the strength of the metal/oxide interface, as detailed in the next section.

3. DFT modeling of oxidation effects on GB strength in FCC Ni

As mentioned earlier, nickel-base alloys such as alloys 82/182 are susceptible to stress corrosion cracking (SCC) when they are in corrosive environment and under tensile stress. In general, oxidation prefers to occur at grain boundaries (GBs) and therefore the SCC facture behavior is mainly intergranular type. When GBs are oxidized, the lower fracture toughness of GB oxides leads to intergranular fracture. At the crack tip, oxygen can penetrate into the metal and form solid solution with the metal. Experimental works have shown that when crack tip oxidization occurs, GB oxide can be either protective which prevents further corrosion or non-protective because of its porous microstructures [22, 23]. Regardless of the oxide microstructures at GBs, the oxidation at GBs can lead to SCC. However, it is unclear how the oxidation affects the GB strength. In this work, we use density functional theory (DFT) calculations to study the effect of oxidation on GB strength in Ni. A few factors are considered: GB type, oxygen concentration, oxygen incorporation type (interstitial and substitutional), partially (Ni + O) and fully (NiO) oxidized GBs, as well as the Ni/NiO metal-oxide interface.

In this work, a brittle fracture at GBs is assumed. The definition of the GB strength of a pristine GB is the same as in Equation (4). Here this equation is rewritten below again in order to better explain the impurity effect:

$$\gamma^0 = 2\gamma_S - \gamma_{GB}\,, \tag{5}$$

where γ^0 is GB strength, γ_S is free surface energy, γ_{GB} is GB energy. When the GB contains some impurities such as oxygen, the GB strength changes. According to the Rice and Wang model [24], the new GB strength is

$$\gamma^{imp} = \gamma^0 + \frac{(\Delta E_{seg}^{GB} - \Delta E_{seg}^{FS})}{A} = \gamma^0 + \Delta\gamma^{imp}, \quad (6)$$

where ΔE_{seg}^{GB} is the impurity segregation energy at the GB, ΔE_{seg}^{FS} is the impurity segregation energy at the free surface, A is GB area, and $\Delta\gamma^{imp}$ is the change of GB strength due to the impurity with respect to the pristine GB.

To build GB structures, the coincident-site lattice (CSL) model [25] is used. First, three pure NiO GBs are constructed: $\Sigma3(111), \Sigma3(112)$ and $\Sigma5(210)$. Note the $\Sigma3(111)$ GB is a coherent twin GB. These GBs represent fully oxidized GBs. The GB strengths of these GBs are calculated and the results are compared with the counterparts in pure Ni. Next, three partially oxidized GBs of the same types are studied: $\Sigma3(111), \Sigma3(112), \Sigma5(210)$. In the partially oxidized GBs, oxygen atoms are incorporated at both interstitial and substitutional sites. The concentration of oxygen atoms at GBs also varies, ranging from one single oxygen atom to four atoms. All DFT calculations are performed using the Vienna Ab initio Simulation package (VASP) [26, 27], with the Generalized Gradient Approximation PBE (GGA-PBE) functional [28] and projected augmented-wave (PAW) method [29]. All systems are simulated with 420 eV cut-off energy and spin polarization. The minimization is conducted using the conjugate gradient [26] relaxation algorithm. For NiO, the DFT+U approach is used to treat the d-electrons in Ni ions. The Hubbard U term in the DFT+U correction has an effective value of U_{eff} = 5.3 eV. Since NiO is an antiferromagnetic material, opposite magnetic moments are introduced as the initial input in all calculation related to NiO.

First, some basic properties in pure Ni metal and NiO oxide are calculated with DFT. These values are compared with the experimental and other DFT results in literature. Our predicted lattice constants of Ni and NiO are 3.518 Å and 4.179 Å, respectively, which are in very good agreement with the experimental values (3.508 Å for Ni [30] and 4.168 Å for NiO [31]). The energies of GBs and free surfaces in pure Ni are also calculated, as listed in Table 9. The results from our work are in good agreement with the DFT and MEAM (modified embedded atom method) results in literature, indicating our DFT methods are reliable.

Table 9. Energies of GBs and free surfaces in pure Ni from this work and literature.

	DFT, This work (J/m^2)	Literature (J/m^2)
$\Sigma 3(111)$ GB	0.0725	0.05, DFT [32]
$\Sigma 3(112)$ GB	0.8879	0.866, DFT [33]
$\Sigma 5(210)$ GB	1.3167	1.23, DFT [34]
111 Surface	1.8663	2.035, MEAM [35]
112 Surface	2.1971	2.335, MEAM [35]
012 Surface	2.4033	2.34, DFT [34]

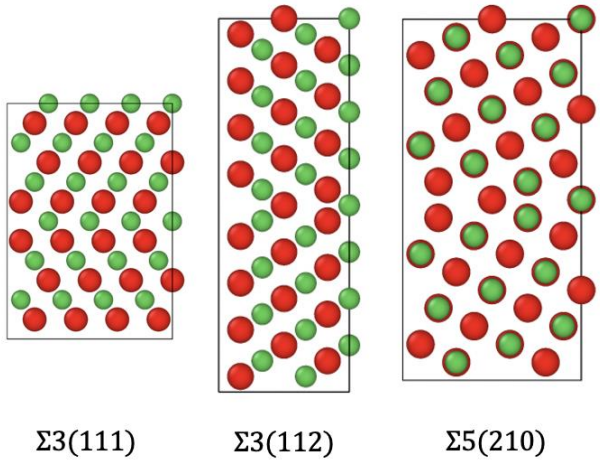

Figure 5. Three fully oxidized GB structures in NiO: $\Sigma 3(111)$, $\Sigma 3(112)$ and $\Sigma 5(012)$. Green spheres represent Ni ions and red spheres represent oxygen ions.

When Ni GBs are fully oxidized, the oxide (NiO) also forms GBs. It is unclear whether the GBs in the oxide form the same CSL structures as the metal GBs. However, the crystal space groups of Ni and NiO are both cubic $Fm\bar{3}m$. The NiO crystal structure can be viewed as that all Ni octahedral interstitial sites are occupied by oxygen atoms. Therefore, here we assumed that NiO GBs have the same CSL types as the original Ni GBs. As a result, the $\Sigma 3(111), \Sigma 3(112)$ and $\Sigma 5(210)$ NiO GBs are chosen to study. The GB structures are shown in Figure 5. The GB energies, free surface energies, and GB strengths in both pure Ni and NiO are calculated using Equation (5), as shown in Table 10. In pure Ni, all three GBs have similar strengths around 3.5 J/m^2. For NiO, the GB strength strongly depends on the GB type. Interestingly, the strength of $\Sigma 3(111)$ coherent

twin GB in NiO is even higher than all metallic GBs in pure Ni, indicating that the coherent twin GB may be difficult to fracture even after it is fully oxidized. For other two types of GBs in NiO, the GB strengths are much smaller than the counterparts in pure Ni, suggesting that the fully oxidized GBs are much weaker than those in pure Ni. In particular, the strength of the $\Sigma 3(112)$ incoherent twin GB in NiO is extremely small, which is opposite to the $\Sigma 3(111)$ coherent twin GB in NiO. The general trend is that the fully oxidized GBs have lower strength than the metallic counterparts, except for the special $\Sigma 3(111)$ coherent twin GB.

Table 10. DFT results of GB energies, free surface (FS) energies, and GB strengths in pure Ni metal and NiO oxide.

	Ni $\boldsymbol{\Sigma 3(111)}$	**Ni** $\boldsymbol{\Sigma 3(112)}$	**Ni** $\boldsymbol{\Sigma 5(210)}$	**NiO** $\boldsymbol{\Sigma 3(111)}$	**NiO** $\boldsymbol{\Sigma 3(112)}$	**NiO** $\boldsymbol{\Sigma 5(210)}$
GB energy (J/m^2)	0.0725	0.8879	1.3167	1.3456	1.4890	2.4578
FS energy (J/m^2)	1.8663	2.1971	2.4033	2.6775	1.0155	2.1373
GB strength (J/m^2)	**3.6601**	**3.5063**	**3.4899**	**4.0093**	**0.5420**	**1.8168**

At the crack tip region, oxygen can diffuse into the crack tip and form solid solution with Ni metal so that the GB is partially oxidized. Here the GB strengths of partially oxidized GBs are calculated at different oxygen concentrations using Equation (6). Both substitutional and interstitial types of oxygen incorporation at GBs are considered. In Equation (6), the change of GB strength due to impurity ($\Delta\gamma^{imp}$) with respective the pristine GB can be used to quantify the SCC susceptibility. Here a negative value of $\Delta\gamma^{imp}$ indicates the embrittlement potency while a positive value means strengthening tendency. For substitutional oxygen, the first step is to find the substitutional site that has the largest $\Delta\gamma^{imp}$ in absolute value, or in other words, the highest embrittlement potency. As shown in Fig. 6, three possible substitutional sites in each GB are chosen. Each site represents one molecular layer (ML). Here the fracture plane is assumed to always occur at the middle of each GB. Our results show that the substitution site at the position 0 leads to the highest embrittlement potency in all GBs. Therefore the GB site 0 is chosen as the substitutional site in this work. For interstitial oxygen sites at GBs, their locations are not obvious because GB structures are complex. To find the optimum interstitial sites at each GB, we use the method developed by Jiang [36]. The advantage of this method is that it can find the interstitial sites in an

arbitrary atomic structure, which is suitable for the complex GB structures. The final optimum interstitial sites are shown in Figure 7.

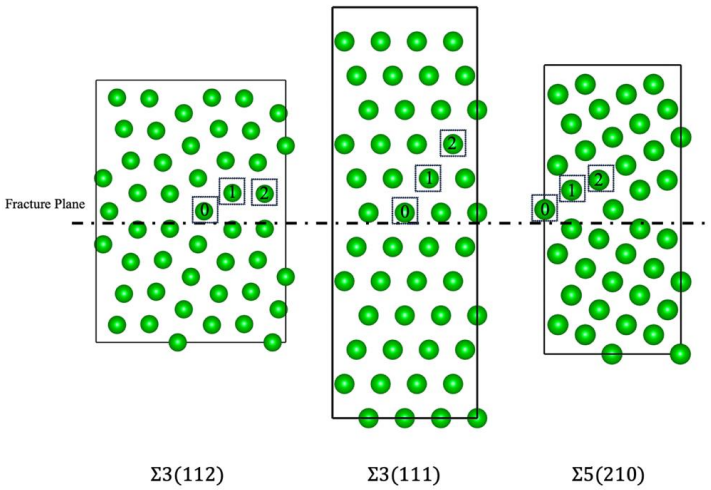

Figure 6. Three fully relaxed GB structures in pure Ni for modeling partially oxidized GBs. The labels in each GB indicate the possible substitutional sites by oxygen.

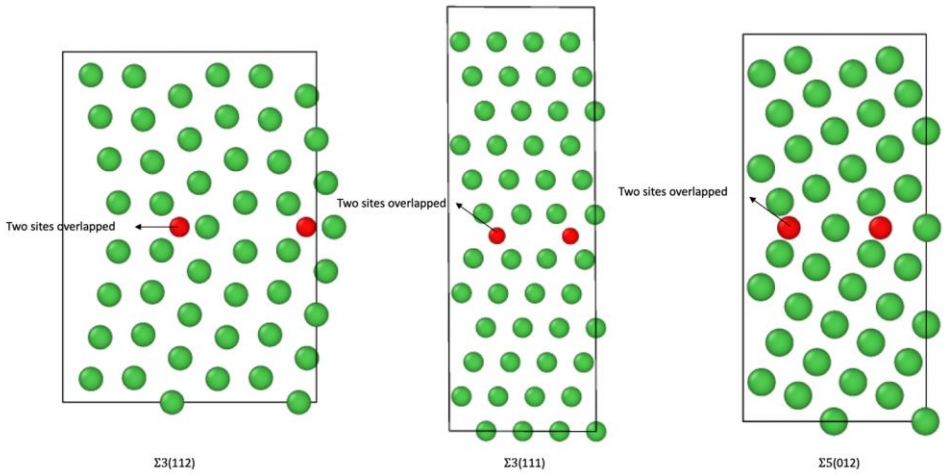

Figure 7. The oxygen interstitial sites (red spheres) identified at each partially oxidized Ni GB. There are four interstitial positions at each GB. Green spheres represent Ni ions and red spheres represent oxygen ions.

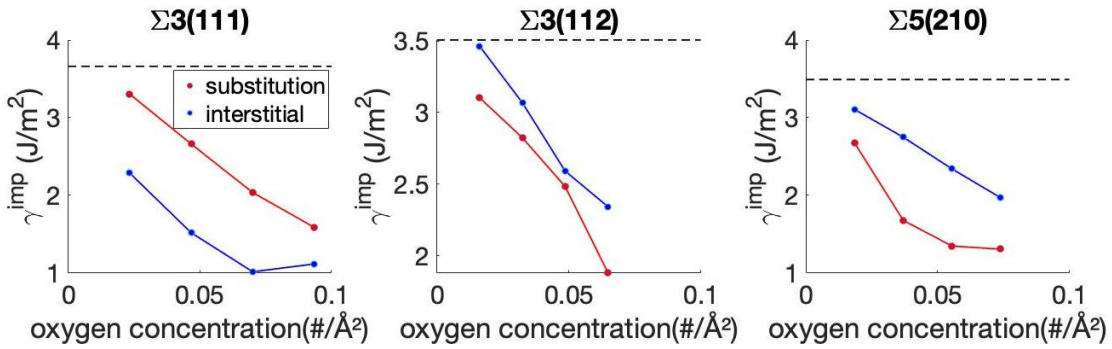

Figure 8. GB strengths at different oxygen concentrations or coverage. Both interstitial and substitutional oxygen types are considered for each GB. The dashed line in each figure shows the strength of the pristine GB.

To study the effect of oxygen concentration on the GB strength in the partially oxidized GBs, the oxygen concentration is varied for both substitutional and interstitial oxygen. To have a fair comparison between different GBs, the oxygen concentration is used, which is the number of oxygen atoms per unit GB area. Here the oxygen concentration ranges from $1/A_{GB}$ to $4/A_{GB}$, where A_{GB} is GB area. The results are shown in Figure 8. In all three GBs, the GB strength decreases with the increasing oxygen concentration for both interstitial and substitutional oxygen, indicating that the increasing oxidation level can reduce the GB strength significantly. Interestingly, in the $\Sigma3(111)$ GB the interstitial oxygen causes more reduction in strength than substitutional oxygen. However, in the other two GBs, the trend is opposite: substitutional oxygen has stronger effects than interstitial oxygen on the GB strength. For substitutional oxygen, the strength of $\Sigma5(210)$ GB decreases most than the other two GBs at high oxygen concentration. For interstitial oxygen, the strength of $\Sigma3(111)$ GB decreases most than the other two GBs at high oxygen concentration. Overall, the strength of partially oxidized GBs can decrease to similar values as the fully oxidized GBs (Table 10), suggesting that fracture could initiate from partially oxidized crack tips as well.

When a GB is fully oxidized, the oxide can form two metal-oxide interfaces with the two metal grains. If the metal-oxide interface is weak, it can also be a favorable crack initiation site. To calculate the metal-oxide interface strength, a block of Ni and a block of NiO are placed together along the [001] direction. For the NiO block, the DFT+U correction is used while no such correction is used for the Ni block. Our result shows that the strength of the Ni/NiO interface is only 0.41 J/m^2. It should be noted that this strength is the weakest one among all the interfaces

considered in this work: three fully oxidized GB, three partially oxidized GBs with different oxygen incorporation, and the metal/oxide interface.

In summary, first-principles DFT calculations are conducted to study the strengths in both partially oxidized GBs and fully oxidized GBs in Ni, as well as the Ni/NiO interface. Our results show that in general oxidation can reduce the GB strength significantly, except for the fully oxidized $\Sigma3(111)$ coherent twin GB in NiO. For other fully oxidized GBs, GB strengths of $\Sigma3(112)$ and $\Sigma5(210)$ in NiO are much lower than the counterparts in pure Ni. For partially oxidized GBs, our results show that both interstitial and substitutional oxygen can reduce the GB strengths significantly, in particular at high oxygen concentrations. However, their relative effects depend on GB type. The strengths of partially oxidized GBs at high oxygen concentrations can reach similar values as the fully oxidized GBs, indicating that fracture could initiate at the partially oxidized crack tips. For the Ni/NiO interface, its strength is the lowest among all the interfaces or GBs modeled in this work, indicating that the metal/oxide interface could be a favorable place for crack initiation, assuming that the GBs can be fully oxidized before fracture occurs.

4. DFT modeling of oxidation effects on GB strength in FCC Fe

Iron (Fe) based stainless steels such as alloys 308/309 are widely used as structural and weldment materials in nuclear reactors. However, they are also susceptible to stress corrosion cracking (SCC) under corrosive environment and tensile stress [37]. Similar as Ni-base alloys, in stainless steels oxidation prefers to occur at grain boundaries (GBs) so that the SCC facture behavior is mainly intergranular type. Therefore, it is important to understand how oxidation impacts the mechanical strength of GBs in these Fe-based steels. In the previous section, we have used density functional theory (DFT) calculations to study how oxidation reduces the GB strength in FCC Ni. In this work we use a similar approach to study the oxidation effect on the GB strength in FCC Fe (as a model system for γ austenite steels), using a $\Sigma5(210)$ GB as a representative example.

To build the $\Sigma5(210)$ GB structure, the coincident-site lattice (CSL) model [25] is used. After a pure $\Sigma5(210)$ GB in FCC Fe is built, only the substitutional oxygen is studied. In this work, up to four substitutional oxygen atoms are added to the GB, as shown in Figure 9. These substitutional oxygen atoms correspond to 1/4 to 1 monolayer coverage at the central GB plane. Again, the fracture plane is assumed to occur at the center of the GB. The method for calculating the oxidation effect on GB strength in FCC Fe is similar as for Ni. Specifically, Equations (5) and

(6) are used to calculate the strengths of the pristine GB and partially oxidized GB, respectively. All DFT calculations are performed using the Vienna Ab initio Simulation package (VASP) [26, 27], with the Generalized Gradient Approximation PBE (GGA-PBE) functional [28] and projected augmented-wave (PAW) method [29]. All systems are simulated with 420 eV cut-off energy. The minimization is conducted using the conjugate gradient [26] relaxation algorithm. In our simulations we treat FCC Fe as non-magnetic.

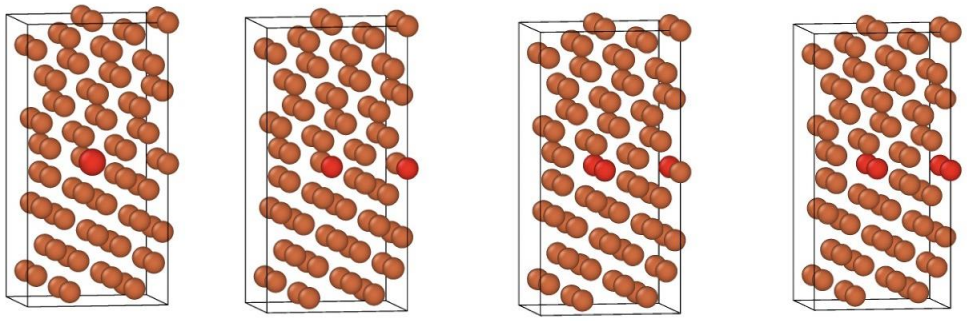

Figure 9. Configurations of a Σ5(210) GB in a FCC Fe with 1/4 to 1 monolayer oxygen coverage at the middle GB plane. Here brown spheres represent Fe atoms and red spheres represent substitutional oxygen atoms.

Our DFT modeling predicts that the lattice constant for an FCC Fe is 3.44 Å, which is close to the simulation result (3.45 Å) reported in literature [38]. For the pure Σ5(210) GB, the GB energy is predicted as 1.55 J/m^2. The pure (210) surface energy is predicted as 3.54 J/m^2. Using Equation (5), the GB strength of the pristine Σ5(210) GB in FCC Fe is 5.53 J/m^2. Figure 10 shows the reduction of GB strength ($\Delta\gamma^{imp}$) of the Σ5(210) GB at different concentrations of substitutional oxygen atoms. As expected, the GB strength drops as the oxygen concentration increases. We also find that the GB strength decreases almost linearly from 1O to 3O while drops sharply at 4O (one full monolayer coverage). We think this effect mainly comes from the complete bond change (metallic to ionic) at the GB plane. When the oxygen forms a full monolayer at 4O, all the strong metallic bonds are substituted by the brittle ionic bonds, which can lead to a large decrease of the GB strength. Similar to the partially oxidized Ni GBs, the GB strength in FCC Fe can decrease significantly. At the one full monolayer coverage, the strength can decrease to about 30% of the pristine GB strength for this Σ5(210) GB.

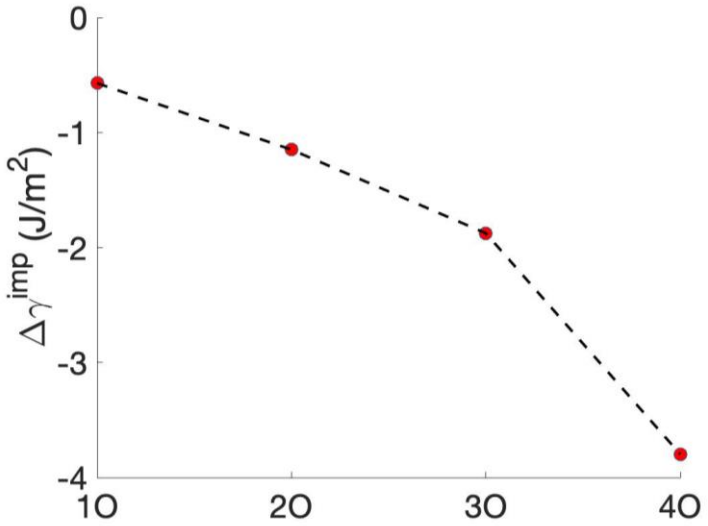

Figure 10. Reduction of GB strength as a function of oxygen concentration. Substitutional 1O to 4O atoms represent 1/4 to 1 monolayer coverage at the Σ5(210) GB plane as shown in Figure 9. Note $\Delta\gamma^{imp} = 0$ is referenced to the strength of the pristine Σ5(210) GB in FCC Fe, which is 5.53 J/m^2.

5. Rate theory modeling of radiation-induced segregation (RIS) in alloys 82/182

Nickel (Ni) based alloys 82/182 are important weldment materials in nuclear reactors. Alloys 82/182 contain moderate concentration of chromium (Cr), ranging from 18-22 wt.% in alloy 82 and 13-17 wt.% in alloy 182. Under irradiation, Cr as well as other solute/impurity elements may couple with radiation-induced defects and segregate to defect sinks such as grain boundaries (GB). This phenomenon is called radiation-induced segregation (RIS) [39]. Depending on the solute type and irradiation conditions, both depletion and enrichment of solute/impurity elements can happen at GBs. Since Cr is the major corrosion-resistant solute element, depletion of Cr at GBs (if occur) may lead to undesirable irradiation assisted stress corrosion cracking (IASCC). As a result, intergranular fracture under relatively low tensile stress can occur. Therefore, prediction of the RIS behavior of Cr in alloys 82/182 is important for understanding their IASCC behavior. In this work, we use the Ni-Cr binary alloy as a model system for alloys 82/182. The commonly used rate theory based RIS model [39] is used to predict the Cr segregation behavior under irradiation.

Under irradiation, radiation-induced defects such as vacancies and interstitials can be produced from cascade. The concentration of these point defects can be much higher than the thermally generated defects. These point defects are mobile so that they can diffuse in the crystal.

Some opposite types of defects (interstitials and vacancies) can annihilate each other through a recombination process. Some defects of the same type can accumulate to form larger clusters (dislocation loops and voids). Some defects can flow to defect sinks such as GBs. When defects diffuse to GBs, they can carry solute elements either through the interstitial mechanism or vacancy exchange mechanism. However, their transport rates are not equal. As a result, the preferential transport of some alloying elements can lead to RIS (either enrichment or depletion) of these elements at GBs. Rate theory based modeling can be used to model the RIS process [39], which is described below.

In an A-B binary alloy, the atomic fractions or concentrations of A and B elements are represented by C_A and C_B, respectively. Under irradiation, the concentrations of interstitials and vacancies are represented by C_i and C_v, respectively. Interstitials and vacancies flow from the bulk crystal towards the GB, which induce fluxes (J) of A and B. In the 1-D space (in the direction perpendicular to the GB plane), the time evolution of interstitials (i), vacancies (v), A and B can be described by the following partial differential equations (PDEs):

$$\frac{\partial C_i}{\partial t} = -\nabla J_i + \epsilon K_0 - R C_v C_i - z_i D_i C_i \rho_s, \quad (7)$$

$$\frac{\partial C_v}{\partial t} = -\nabla J_v + \epsilon K_0 - R C_v C_i - z_v D_v C_v \rho_s, \quad (8)$$

$$\frac{\partial C_A}{\partial t} = -\nabla J_A, \quad (9)$$

$$\frac{\partial C_B}{\partial t} = -\nabla J_B. \quad (10)$$

Here ∇ is gradient, K_0 is dose rate, ϵ is cascade efficiency, R is the recombination rate between vacancies and interstitials and $R = \frac{500}{a_0^2}(D_v + D_i)$ [39], a_0 is the lattice parameter, D_i and D_v are interstitial and vacancy diffusion coefficients, respectively; The z_v and z_i are the absorption efficiencies for vacancies and interstitials, respectively; The ρ_s is the sink strength (e.g., dislocation density).

The fluxes of defects and alloying elements have the following forms:

$$J_i = -\alpha d_{A-i} C_i \nabla C_A - \alpha d_{B-i} C_i \nabla C_B - D_i \nabla C_i, \quad (11)$$

$$J_v = \alpha d_{A-v} C_v \nabla C_A + \alpha d_{B-v} C_v \nabla C_B - D_v \nabla C_v, \quad (12)$$

$$J_A = -D_A \alpha \nabla C_A + d_{A-v} C_A \nabla C_v - d_{A-i} C_A \nabla C_i, \quad (13)$$

$$J_B = -D_B \alpha \nabla C_B + d_{B-v} C_B \nabla C_v - d_{B-i} C_B \nabla C_i, \quad (14)$$

here we assume $\alpha = 1$ for an ideal solution. The d_{e-d} is the interdiffusion coefficient between alloying element type *e* and defect type *d*, which is expressed as:

$$d_{e-d} = \frac{z}{6}\lambda^2 \omega_{e-d} f_{e-d} \exp(-\frac{E^m_{e-d}}{k_B T}), \quad (15)$$

where λ, ω and f are the jump distance, jump frequency and correlation factors, respectively. The parameter *z* is the coordination number, which is 12 for FCC metals. The E^m_{e-d} is the migration barrier for element *e* via defect type *d*. The k_B and T are Boltzmann constant and temperature, respectively.

The total diffusion coefficients (D) of defects and alloying elements have the forms,

$$D_i = d_{A-i}C_A + d_{B-i}C_B, \quad (16)$$

$$D_v = d_{A-v}C_A + d_{B-v}C_B, \quad (17)$$

$$D_A = d_{A-i}C_i + d_{A-v}C_v, \quad (18)$$

$$D_B = d_{B-i}C_i + d_{B-v}C_v. \quad (19)$$

Solving the PDE Equations. (7 – 10), the time evolution of C_i, C_v, C_A, and C_B can be obtained if the initial and boundary conditions are provided. The initial conditions at t = 0 are:

$$C_A(t=0,x) = C_A^0, \quad C_B(t=0,x) = C_B^0 \quad (20)$$

$$C_i(t=0,x) = exp(-E_i^f/k_B T), \quad (21)$$

$$C_v(t=0,x) = exp\left(\frac{S_v^f}{k_B}\right) exp(-E_v^f/k_B T), \quad (22)$$

where C_A^0 and C_B^0 are the initial atomic fractions of alloying elements A and B, respectively; S_v^f is vacancy formation entropy, E_v^f is vacancy formation energy, and E_i^f is interstitial formation energy. The typical boundary conditions for RIS include those at the GB ($x = 0$) and in the bulk ($x = L$). In the bulk region ($x = L$), we assume the concentrations of alloying elements remain constant at their nominal values, while the fluxes of interstitials and vacancies are zero:

$$C_A(t, x = L) = C_A^0, \quad C_B(t, x = L) = C_B^0, \quad (23)$$

$$J_i(t, x = L) = J_v(t, x = L) = 0. \quad (24)$$

At the GB ($x = 0$), we assume the GB is a perfect sink so that the concentrations of vacancies and interstitials remain at their thermal equilibrium values. The fluxes of alloying elements are set to zero:

$$J_A(t, x = 0) = 0, \quad J_B(t, x = 0) = 0, \tag{25}$$

$$C_i(t, x = 0) = exp(-E_i^f / k_B T), \tag{26}$$

$$C_v(t, x = 0) = exp\left(\frac{S_v^f}{k_B}\right) exp(-E_v^f / k_B T). \tag{27}$$

Since the GB is symmetric, we only need to solve the PDE equations at one side of GB ($0 \leq x \leq L$). Another constraint is $C_A + C_B = 1$ because the total atomic fraction of all alloying elements should be unity everywhere.

In this work, we first use our model to simulate the RIS in a Ni-18at.%Cr system under irradiation. The results are compared with previous experimental results [40] reported in literature to calibrate our model. Then we use our calibrated model to predict the RIS behavior in alloys 82/182 under different irradiation conditions. In our RIS model, the 1-D simulation domain length is set to be L = 100 nm, with a mesh size of $dx = 1\ nm$. The finite difference method is used to discretize the PDE Equations. The CVBand solver in the SUNDIALS package [41], which is an implicit solver and allows much larger time steps than explicit solvers, is used to solve these discretized PDE equations. Here the time step is set to 0.1 s. The parameters for our RIS model are listed in Table 11. Previous RIS modeling [42] shows that the model can predict opposite RIS trend to the experimental results in the Ni-Cr system if the density functional theory (DFT) predicted diffusion parameters were directly used. Instead, these parameters need to be adjusted/fitted to match with experiments. Previous RIS modeling [43] also showed that in FCC alloys such as Fe-Cr-Ni, the vacancy mechanism alone is sufficient to predict the RIS trend. In this work we use the same approach and assume that the interstitial flux has a neutral effect on RIS. Therefore the migration barriers and jump frequency are set to the same for both Ni and Cr interstitials. In previous ab initio molecular dynamics (AIMD) calculations [44], the Ni and Cr interstitial barriers are in the range of 0.31 – 0.37 eV. So here 0.35 eV is used for both interstitial migration barriers. For vacancies, the migration barriers are the same for Ni and Cr (1.09 eV [45]), while the jump frequency of Cr vacancy is slightly larger than the Ni vacancy. Using this simplified approach, our modeling results agree well with Allen's experimental results [40], as shown below.

Table 11. Parameters used for modeling RIS in Ni-Cr.

Parameter	Notation	Value
Lattice parameter	a_0	$3.53 \times 10^{-10} m$
Jump distance	λ	$2.5 \times 10^{-10} m$
Sink strength	ρ_s	$1.0 \times 10^{13} m^{-2}$
Absorption efficiency for vacancies	z_v	1.0 [46]
Absorption efficiency for dislocations	z_i	1.2 [46]
Cascade efficiency	ϵ	1.0
Vacancy jump frequency for Ni	ω^0_{Ni-v}	1.5×10^{13} s^{-1} [47]
Vacancy jump frequency for Cr	ω^0_{Cr-v}	2.1×10^{13} s^{-1}
Interstitial jump frequency for Ni	ω^0_{Ni-i}	5.0×10^{12} s^{-1} [47]
Interstitial jump frequency for Cr	ω^0_{Cr-i}	5.0×10^{12} s^{-1} [47]
Vacancy migration energy for Ni	E^m_{Ni-v}	1.09 eV [45]
Vacancy migration energy for Cr	E^m_{Cr-v}	1.09 eV
Interstitial migration energy for Ni	E^m_{Ni-i}	0.35 eV
Interstitial migration energy for Cr	E^m_{Cr-i}	0.35 eV
Vacancy jump correlation factor for Ni	f_{Ni-v}	1.0
Vacancy jump correlation factor for Cr	f_{Cr-v}	1.0
Interstitial jump correlation factor for Ni	f_{Ni-i}	1.0
Interstitial jump correlation factor for Cr	f_{Cr-i}	1.0
Formation entropy of vacancy	S^f_v	5.71 k_B [45]
Formation enthalpy of vacancy	E^f_v	1.61 eV
Formation enthalpy of interstitial	E^f_i	4.0 eV [48]

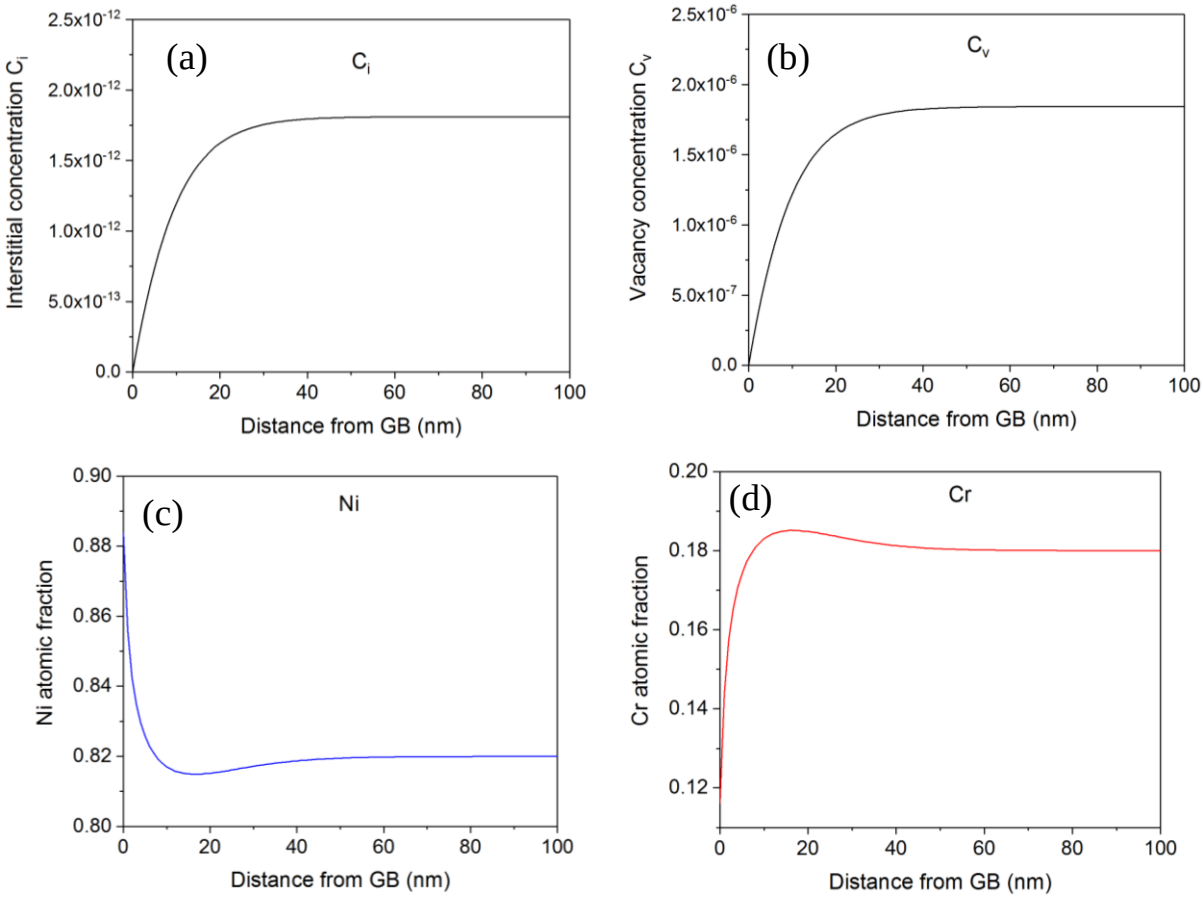

Figure 11. Our rate theory modeling of RIS behavior in a Ni-18at.%Cr at 300°C under an irradiation dose rate of 7×10^{-6} dpa/s to a 0.5 dpa dose. (a) Interstitial concentration profile. (b) Vacancy concentration profile. (c) Ni concentration profile. (d) Cr concentration profile.

First we use our model to simulate the RIS behavior in a Ni-18at.%Cr alloy under irradiation and compare the results with Allen's experimental results [40]. In Allen's experiment, a Ni-18at.%Cr alloy was irradiated with 3.2 MeV protons to a dose of 0.5 dpa with dose rate of 7×10^{-6} dpa/s. The irradiation temperature was in the range of 200 – 500 °C. These irradiation conditions are used in our modeling. Figure 11 shows the concentration profiles of interstitial, vacancy, Ni, and Cr as a function of the distance from the GB at 300 °C. Both interstitial and vacancy concentrations are very low at the GB while they remain constant in the bulk region. This is expected because our GB is a perfect defect sink. Our model predicts that Ni is enriched while Cr is depleted at the GB, which is consistent with the experimental observation [40]. One interesting

phenomenon is that both Ni and Cr concentrations do not monotonically increase or decrease when the distance approaches the GB. This kind of non-monotonic concentration profile has been frequently observed in experiments in different systems [49]. This behavior could be a competition between the driving forces induced by the defect concentration gradient and alloying element concentration gradient.

To have a quantitative comparison of the RIS magnitude between our modeling and Allen's experiment [40], we model RIS in the Ni-18at.%Cr alloy at 300, 400, 500, and 600 °C using the same parameter set. The dose rate is still 7×10^{-6} dpa/s and the total dose is 0.5dpa. Figure 12 shows the comparison of the Cr concentration after irradiation between our modeling and Allen's experiment at these temperatures. Clearly, the agreement is pretty good, except that our modeling predicts slightly more Cr depletion at 200 °C. In particular, our modeling captures the turnaround of Cr depletion at 500 °C without any further parameter adjustments.

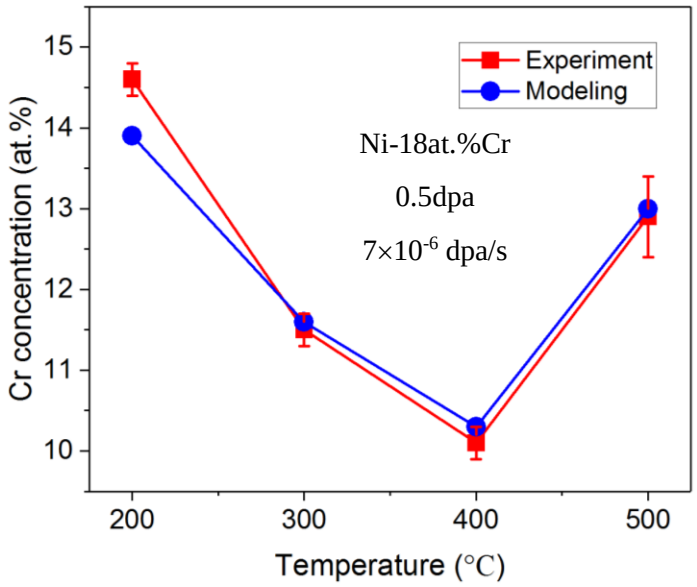

Figure 12. Comparison of Cr concentration after irradiation between our RIS modeling and Allen's experiment [40] in a Ni-18at.%Cr at 200 – 500°C under proton irradiation to a dose of 0.5dpa with a dose rate of 7×10^{-6} dpa/s.

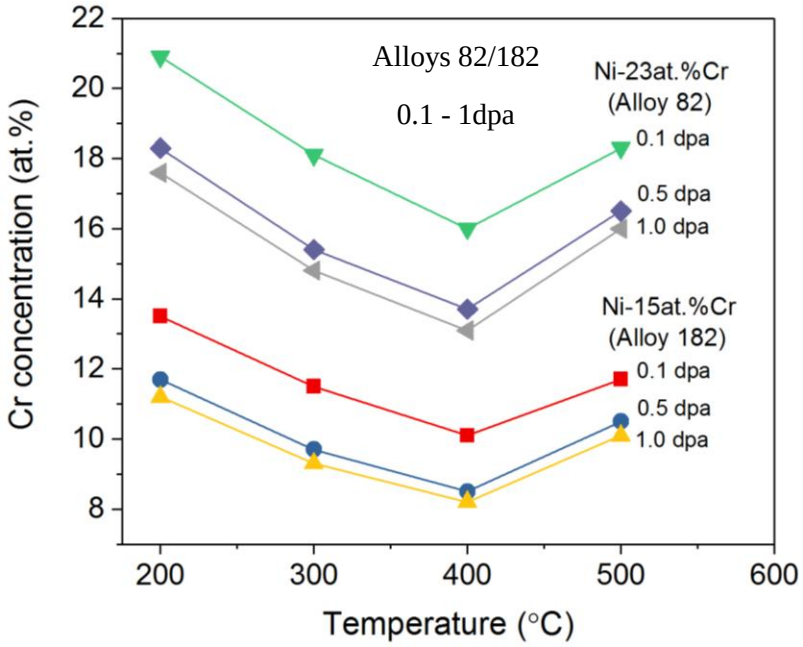

Figure 13. Our RIS modeling prediction of Cr concentration after irradiation in Ni-23at.%Cr (alloy 82) and Ni-15at.%Cr (alloy 182) at different temperatures (300, 400, 500, and 600 °C) and different irradiation doses (0.1, 0.5, 1.0 dpa).

After our RIS model is calibrated against Allen's Ni-18at.%Cr experiment, we apply our model to predict the Cr segregation in Ni-base alloys 82 and 182. In alloy 82, the Cr concentration is in the range of 18-22 wt.%, which is approximately 19.86 – 24.15 at.%Cr in Ni. Here we use Ni-23at.%Cr as a model alloy for alloy 82. In alloy 182, the Cr concentration is in the range of 13-17 wt.%, which is approximately 14.43 – 18.78 at.%Cr in Ni. Here we use Ni-15at.%Cr as a model alloy for alloy 182. The irradiation is assumed to reach a total dose of 1 dpa with a dose rate of 1×10^{-5} dpa/s. The irradiation temperature is again in the range of 200 – 500 °C. Figure 13 shows our prediction of Cr concentrations after irradiation for both Ni-15at.%Cr (alloy 182) and Ni-23at.%Cr (alloy 82) at different temperatures (300, 400, 500, and 600 °C) and different irradiation doses (0.1, 0.5, 1.0 dpa). As expected, the overall behavior is similar as in Figure 12 for both alloys. The magnitude of Cr depletion initially increases with temperature, then turns around at 400 °C. For the dose effect, the 0.1 dpa dose induces much less Cr depletion than those at 0.5 and 1.0 dpa. The difference between 0.5 and 1.0 dpa is small, indicating that the RIS may reach a steady state after 0.5 dpa. Therefore, further increase of irradiation dose may not lead to significantly more Cr

depletion. It should be noted that our model parameters are calibrated against the irradiation experiment using a pure Ni-18at.%Cr model alloy under specific irradiation conditions. In alloys 82/182, there are many other alloying elements. Even though their concentrations are not high, they may affect the defect diffusivities as well as other thermo-kinetic properties. Therefore, it is likely that our model parameters need to be adjusted slightly for the real alloys 82/182 in order to predict the quantitative RIS magnitude of Cr. Unfortunately, the experimental RIS data for the alloys 82/182 are not available in this project so that the modeling results cannot be validated. Regardless, we expect that the qualitative behavior (e.g., Cr depletion) predicted by our model will not change.

6. Rate theory modeling of radiation-induced segregation (RIS) in alloys 308/309

Iron (Fe) based stainless steels 308L/309L are important structural and weldment materials in nuclear reactors. Both 308L and 309L contain moderate concentration of chromium (Cr) and nickel (Ni). The major composition in 308L is Fe-21.07at.%Cr-9.69at.%Ni while in 309L is Fe-24.38at.%Cr-12.80at.%Ni [50]. Other minor elements such as Mn and Si are also present in these alloys. Under irradiation, major alloying element (Fe, Cr, Ni) as well as other minor solute/impurity elements (e.g., Si) may couple with radiation-induced defects and segregate to defect sinks such as grain boundaries (GBs). This phenomenon is called radiation-induced segregation (RIS) [39]. Depending on the solute type and irradiation conditions, both depletion and enrichment of alloying elements can happen at GBs. Since Cr is the major corrosion-resistant solute element, depletion of Cr at GBs may lead to undesirable stress corrosion cracking (SCC). On the other hand, enrichment of Ni and Si at GBs may lead to the precipitation of brittle Ni_3Si γ' phase or Ni-Si clusters [50]. As a result, intergranular fracture under relatively low tensile stress can occur. Therefore, prediction of the RIS behavior of Fe, Cr, and Ni in 308L/309L stainless steels is important for understanding their irradiation assisted SCC (IASCC) behavior. In our experiments, we have measured the RIS profiles of the three major elements (Fe, Cr, Ni) at a γ-γ GB in 308L under proton irradiation at 360 °C. In this work, we use the Fe-Cr-Ni ternary alloy as a model system for alloy 308L so that we can directly compare our RIS modeling and experimental results. Similar as our RIS modeling for binary Ni-Cr alloys as discussed in the previous section, the commonly used rate theory based RIS model [39] is used to predict the Fe, Cr, and Ni segregation behavior under irradiation.

The RIS model for the ternary system is similar to the binary system, although the equations and terms that are related to element C need to be added to those equations described in this previous section, which is straightforward. For the recombination rate (R) between vacancies and

interstitials, a new form of $R = \frac{4\pi R_{iv}}{\Omega}(D_v + D_i)$ [46] is used, where R_{iv} is the spontaneous recombination radius, Ω is the atomic volume of an FCC Fe atom, D_i and D_v are interstitial and vacancy diffusion coefficients, respectively. In previous RIS modeling [43] showed that in FCC alloys such as Fe-Cr-Ni, the vacancy mechanism alone is sufficient to predict the RIS trend. In this work we use the same approach and assume that the interstitial flux has a neutral effect on RIS. Therefore the migration barriers and jump frequencies are set to the same for all Fe, Cr, and Ni interstitials. For vacancies, the migration barriers are set to be the same for all elements, while the order of their jump frequencies is $\omega^0_{Ni-v} < \omega^0_{Fe-v} < \omega^0_{Cr-v}$. The parameters are listed in Table 12. The numerical method for solving PDEs is the same as for the binary Ni-Cr systems.

Table 12. Parameters used for modeling RIS in Fe-Cr-Ni.

Parameter	Notation	Value
Lattice parameter	a_0	$3.57 \times 10^{-10} m$
Jump distance	λ	$2.52 \times 10^{-10} m$
Atomic volume	Ω	$1.14 \times 10^{-29} m^3$
Sink strength	ρ_s	$1.0 \times 10^{13} m^{-2}$
Spontaneous recombination radius	R_{iv}	$1.0 \times 10^{-9} m$
Absorption efficiency for vacancies	z_v	1.0
Absorption efficiency for dislocations	z_i	1.0
Cascade efficiency	ϵ	0.1
Vacancy jump frequency for Fe	ω^0_{Fe-v}	2.5×10^{13} s^{-1} [47]
Vacancy jump frequency for Cr	ω^0_{Cr-v}	3.1×10^{13} s^{-1}
Vacancy jump frequency for Ni	ω^0_{Ni-v}	1.6×10^{13} s^{-1}
Interstitial jump frequency for Fe	ω^0_{Fe-i}	5.0×10^{12} s^{-1} [47]
Interstitial jump frequency for Cr	ω^0_{Cr-i}	5.0×10^{12} s^{-1} [47]
Interstitial jump frequency for Ni	ω^0_{Ni-i}	5.0×10^{12} s^{-1} [47]

Vacancy migration energy for Fe	E_{Fe-v}^{m}	1.2 eV [47]
Vacancy migration energy for Cr	E_{Cr-v}^{m}	1.2 eV [47]
Vacancy migration energy for Ni	E_{Ni-v}^{m}	1.2 eV [47]
Interstitial migration energy for Fe	E_{Fe-i}^{m}	0.5 eV
Interstitial migration energy for Cr	E_{Cr-i}^{m}	0.5 eV
Interstitial migration energy for Ni	E_{Ni-i}^{m}	0.5 eV
Formation entropy of vacancy	S_v^f	5.0 k_B
Formation enthalpy of vacancy	E_v^f	1.4 eV [47]
Formation enthalpy of interstitial	E_i^f	4.0 eV [48]

Our experimental team has irradiated a dual phase 308L weldment filler material [50]. The irradiation experiment was conducted using 2 MeV protons at 360 °C with a dose rate of about 9.9×10^{-6} dpa/s and to a damage level of 5 dpa. In their experiment, they found that Cr depletion and Ni enrichment at an austenitic γ-γ GB. To be consistent with our experiment in which a few percent of other minor elements are present in the 308L, the constraint of $C_A + C_B + C_C = 0.981$ is used here. Specifically, the initial concentrations of the three elements are: C_A^0 = 0.683 for Fe, C_B^0 = 0.204 for Cr, and C_C^0 = 0.094 for Ni. The dose rate is 1×10^{-5} dpa/s and the total irradiation dose is 5 dpa. The simulation temperature is 360 °C, which is the same as in our experiment. Figure 14(a) shows our modeling results of the concentration profiles of Ni, Fe, and Cr as a function of distance from the austenitic γ–γ GB (lines), along with our experimental results (symbols) for comparison. The experimental measurements were obtained from STEM-EDS line profiles. Figure 14(b) shows the simulated profile trend from the boundary to the bulk over a longer distance. To have a better visual comparison, we add a mirror image of each concentration profile on the left-hand side of the GB based on the assumption that the profiles are symmetric. Overall, the agreement between the experimental results and the computed profiles is good in terms of the segregation tendencies and magnitudes of these elements. Both show significant Cr depletion and Ni enrichment due to RIS. The observed sharpness of the Cr/Ni depletion/enrichment at the GB is captured by the simulation. Specifically, the width of the perturbation at the GB and the peak/valley concentrations are both captured. However, the length scale associated with the subsequend rise and fall of Cr and Ni (i.e.,

non-monotonically increase or decrease when the distance approaches the GB), respectively, is off by approximately a factor of four (10 versus 40 nm). Regardless of these discrepancies, overall we consider the agreement satisfactory. Therefore, our efforts demonstrate that we have developed our own capabilities of using a combined experimental and modeling approach to study the RIS trends in 308L, which could be extended to other alloy systems and under different irradiaiton conditions in the future.

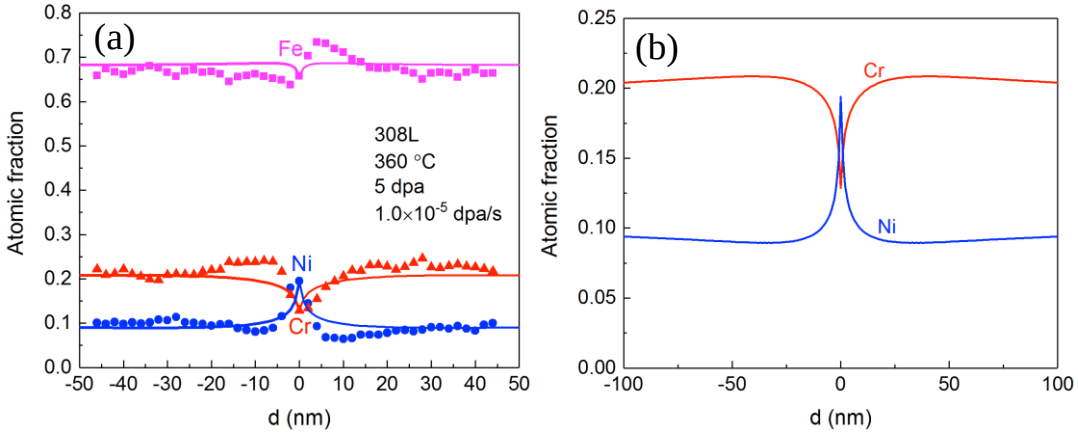

Figure 14. (a) Comparison of measured (plotting symbols) and calculated (solid lines) elemental profiles at a γ–γ GB in 308L stainless steel. (b) The calculated profiles for Cr and Ni out to 100 nm from the GB. The RIS model assumes symmetric profiles so that the profiles for $d < 0$ are the mirror images of their counterparts at $d > 0$. The simulated damage level (5 dpa), damage rate (1×10^{-5} dpa/s), and temperature (360 °C) correspond to the experimental proton irradiation conditions at the depth of the measured elemental profiles.

7. Development of intergranular fracture models in Grizzly at INL

One of the major objectives of the present project is to characterize the effects of degradation of grain boundaries in Ni-based and Fe-based alloys on the homogenized response of the polycrystalline material. This is being done using microstructure models of a representative volume element (RVE) of material, with grain boundary behavior modeled using a zero-thickness cohesive zone model (CZM). The focus of the effort documented here is to develop the foundational capabilities for including CZMs in finite element models using the Grizzly code, which is based on the MOOSE framework [51].

CZMs are a widely used numerical technique to represent localized behavior that occurs on a surface in a three-dimensional (3D) model or a line in a two-dimensional (2D) model. CZMs are typically used in finite element models in which the behavior of the material in the volume is modeled using continuum elements, while the interface behavior is modeled with zero-thickness interface elements. These interface elements are special finite elements that consist of two sets of surfaces (in 3D) or lines (in 2D) with matching pairs of nodes on the opposing surfaces or lines. These paired nodes initially have the same position, but as the model deforms mechanically, they can move relative to each other. Special constitutive models, known as CZMs, are used to predict the traction vs. separation behavior of the material, which represents fracture or debonding. These can be used for multiple applications, including for problems where the locations of interfaces are pre-defined (as in the case of grain boundary fracture), as well as for problems where interfaces would be inserted into the domain in locations where fractures propagate.

As previously mentioned, CZMs are typically modeled using zero-thickness interface elements. One of the objectives of this work is to use the Grizzly code for modeling grain boundary fracture. Grizzly is based on the MOOSE framework, which is a general environment for multiphysics finite element simulations. When this project was originally proposed, neither MOOSE nor Grizzly had support for CZM modeling, and the original plan was to use the extended finite element method (XFEM) as the vehicle for including CZMs in the finite element model. XFEM is a general technique that is used to model arbitrary discontinuities in a finite element model, without forcing the finite element mesh to conform to the discontinuities. This is particularly useful for fracture problems, where the crack path is not known *a priori*. It is also useful for problems for which creating a mesh that conforms to the locations of the discontinuities is challenging. This is an attractive feature for modeling polycrystalline grain structures. While it is reasonably straightforward to create a 2D finite element mesh that conforms to grain boundaries, this can be quite challenging in 3D. Thus, the original intent in this project was to develop and use an XFEM-based CZM capability for modeling grain boundary failure.

At the beginning of this project, MOOSE already had an XFEM capability [52, 53]. This is based on the phantom-node approach [54], which duplicates finite elements cut by a discontinuity, so that there are two overlapping elements that are connected to the rest of the computational mesh in a way that appropriately represents the discontinuity, as well as continuity with material on either side of that discontinuity. Appropriate modifications are made to the integration rules for these duplicated elements to correctly reflect the fact that they only partially represent physical material.

Without any additional modifications, this algorithm treats the model as if there are no interactions between the material across the interface. This is appropriate for some problems, such as the mechanical behavior of brittle fractures, but for many applications, it is important to include some interaction across these discontinuities. For example, heat transfer across a fracture could be important, or in the case of ductile fracture or grain boundary fracture, it could be important to represent cohesive behavior in the mechanical response of the system. In MOOSE's implementation of XFEM, special constraints are used to represent interactions across the surface. There are many documented applications of the use of CZMs with XFEM (e.g. [55]), but this was not supported by MOOSE at the beginning of this project. To allow the use of CZMs on XFEM interfaces, this system needs to be expanded to allow for more complex interactions across these interfaces.

The primary challenge in implementing a CZM capability for use with XFEM in MOOSE was that there was no support for managing the history-dependent data that CZMs typically use in their formulations. Special integration points that exist on these XFEM interfaces are used to apply the constraints. MOOSE has a well-developed system for managing history-dependent material data at standard integration points, such as those in volume elements and on the surfaces of those elements. However, this system is not sufficiently flexible to handle additional integration points that are added at arbitrary locations and points in time, as is needed for the XFEM application. To support the present project, a special material property manager was developed that works together with the XFEM models to manage material data at the integration points on the XFEM interfaces. This system in theory can work together with complex CZMs, and has been demonstrated on a simple CZM that represents linear softening behavior under normal opening, and is dependent on the maximum opening over the course of the analysis. Example applications of this model are shown here.

Independent of the present effort, over the last several years, a more traditional CZM capability was developed for MOOSE that can be used to model interfaces on the boundaries of volume finite elements was also developed [56]. This has reached the point where it is a full-featured capability, and multiple CZMs are implemented within this system. This system is somewhat unique, because rather than using zero-thickness elements, it models CZMs using surface integral terms that contribute to the residual in the partial differential equation system being solved. MOOSE provides a generic system for surface integrals at interfaces between elements known as InterfaceKernels. The CZM capability uses special InterfaceKernels, as well as a mesh modification system that splits meshes along boundaries between blocks representing different

materials and works with the InterfaceKernels to appropriately pair elements on opposing sides of the material boundary.

Although the XFEM-based CZM approach was developed for this project, the InterfaceKernel-based approach has been used as the basis for the majority of the modeling in this project. It is more mature than the XFEM-based approach and supports a wider variety of models. Also, it is able to handle triple junctions, or points at the boundary of three separate grains, with the XFEM-based approach is not yet able to do. Nevertheless, the XFEM-based CZM capability developed for this project is still a very useful development and could be used as the foundation for improved capabilities in the future. It could significantly simplify model creation for polycrystal simulations, especially in 3D, with additional development, and is also useful for modeling arbitrary evolving fractures in ductile or quasibrittle materials.

To demonstrate the XFEM-based CZM capability, a simple square domain with a pre-defined horizontal interface at the center of the domain is modeled, both using the interface-based and XFEM-based CZM capabilities in MOOSE. This model has dimensions somewhat representative of those seen in a grain-scale model, with edge lengths of 8 μm. The bulk material has a Young's modulus of 170 GPa and Poisson's ratio of 0.3. A CZM with linear softening behavior is used. The penalty stiffness of this CZM is 2e6 MPa/μm, which is sufficiently high relative to the stiffness of the bulk material to have a minimal effect on the system response. The strength of the interface is 400 MPa, and the fracture energy is 10 J/m^2. The material is modeled in 2D with plane-strain assumptions.

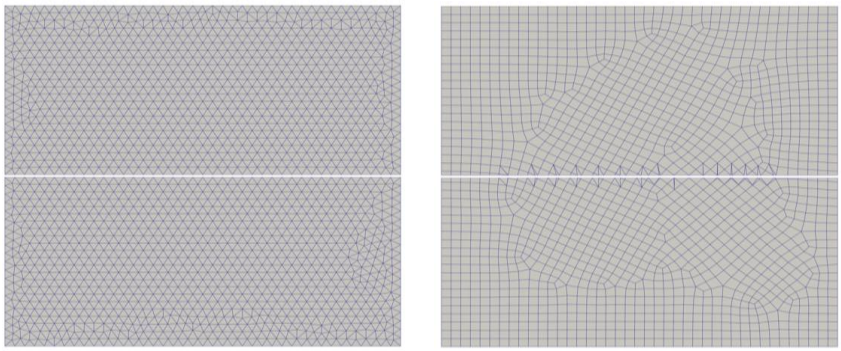

Figure 15. Finite element meshes for (left) the interface-based CZM model demonstration and (right) the XFEM-based CZM model demonstration at the end of the simulation after the interface has lost all its strength.

Figure 15 shows the meshes used in the two simulation approaches. The interface-based CZM model uses an irregular triangular mesh that conforms to the horizontal interface passing through the middle of the model. The XFEM CZM model uses a quadrilateral mesh with an element size equivalent to the interface-based CZM model. This mesh is intentionally distorted to illustrate how XFEM is able to represent arbitrary discontinuities through the elements. In Figure 15, the two meshes are shown in their deformed configurations after they have been pulled upward on the top surface until they have fully separated and lost all strength on the interface. From the XFEM mesh, it can be seen that the algorithm cuts a horizontal line through the elements, which have a variety of orientations. Some of the partial elements are shown as a combination of multiple triangle elements, but that is an artifact of the visualization tool. All of the cut elements are actually quadrilateral elements.

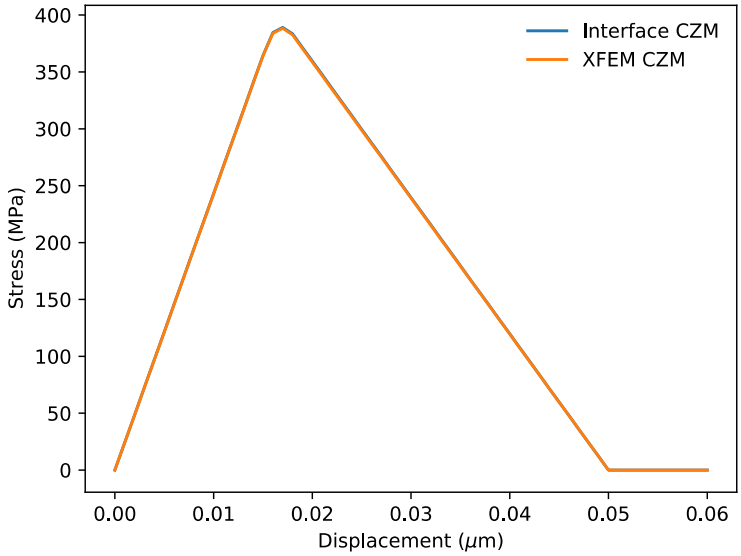

Figure 16. Average stress in the loading direction vs displacement for the interface-based and XFEM-based CZM models. Results are nearly indistinguishable, so they appear as a single line.

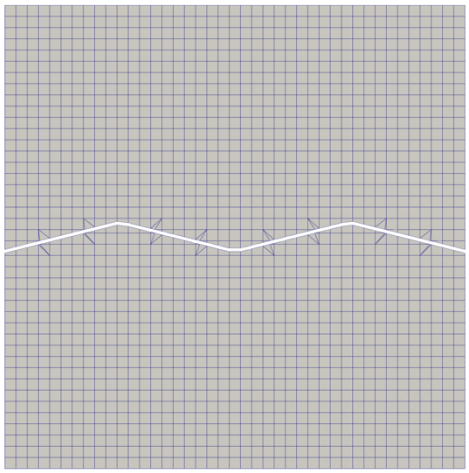

Figure 17. Demonstration simulation using XFEM to model a non-straight interface, showing deformed state after the interface has lost all its strength.

A plot of the stress in the vertical direction vs. the vertical displacement applied to the top surface for these two models is shown in Figure 16. The results are nearly indistinguishable, indicating that both approaches adequately model the physical behavior of the CZM, regardless of the differences in how the interface is actually represented in the finite element model. To illustrate how XFEM could be used to facilitate the simulation of complex grain boundary structures, Figure 17 shows the same problem, but with a wavy interface whose shape is defined by the geometry of the cutting planes, rather than the finite element mesh. As previously noted, this approach currently has the important limitation that it cannot model junctions between three line segments, although this could be removed with further development.

8. Modeling intergranular fracture in polycrystalline alloys 82/182 and 308/309 in MOOSE

Nickel (Ni) based alloys 82/182 and iron (Fe) based alloys 308/309 are important structural and weldment materials in nuclear reactors. These alloys contain moderate concentration of chromium (Cr) for improving their corrosion resistance. However, under irradiation, Cr as well as other solute/impurity elements may couple with radiation-induced defects and segregate to defect sinks such as grain boundaries (GBs). This phenomenon is called radiation-induced segregation (RIS). Depending on the solute type and irradiation conditions, both depletion and enrichment of solute/impurity elements can happen at GBs. In our previous sections, we have used rate theory based RIS modeling to predict that Cr depletion occurs in both alloys 82/182 and alloys 308L/309L under irradiation. Since Cr is a major corrosion-resistant solute element, depletion of Cr at GBs may lead to GB corrosion. In our previous section, we have also used atomic-level density functional theory (DFT) to prove that the strength of oxidized GBs in both Ni and Fe can decrease significantly. The reduction of GB strength may lead to brittle intergranular fracture. Such an

irradiation-assisted stress corrosion cracking (IASCC) behavior is a major concern for the use of these metallic alloys in reactor environment. Our original plan is to use the extended finite element method (XFEM) in the MOOSE-Grizzly to model the SCC behavior in polycrystal alloys 82/182 and 308/309. However, the current XFEM in MOOSE has some challenges to model the fracture near triple junctions, which is critical for correctly modeling the intergranular fracture behavior in polycrystals. During the course of this project, some new capabilities have been developed for the more mature cohesive zone model (CZM) in MOOSE, which is more suitable for modeling the intergranular fracture behavior than the current XFEM. Therefore, in this work, the cohesive zone model (CZM) that is based on the bilinear mixed mode traction separation law in the MOOSE framework (which is accessible by Grizzly) is used for modeling the SCC-induced intergranular fracture under a tensile load. The full details of the bilinear mixed model theory can be found in the technical report by Camanho and Dávila [57]. The key equations of this model also can be found in the online documentation of the MOOSE framework [51].

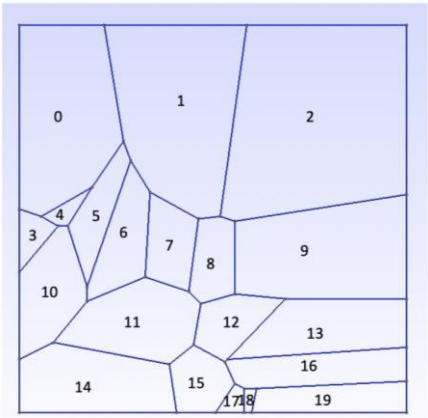

Figure 18. A polycrystal sample containing 20 grains (labeled with 0 – 19) generated by the Voronoi tessellation method. The simulation domain dimensions are $16\mu m \times 16\mu m$.

First we use the Voronoi tessellation algorithm to generate the initial node points for GBs and use Gmsh [58] to generate the mesh grid. The 2D simulation domain dimensions are $16\mu m \times 16\mu m$ and the element size is $0.2\mu m$. The polycrystal structure is shown in Figure 18. There are 20 grains labeled from 0 to 19. In our CZM modeling in MOOSE, the B-K criterion is applied for predicting the displacement propagation. The input parameters are shown in Table 13. The typical strength for Ni-based alloys ranges from 300 MPa to around 700 MPa in experimental stress-strain tests [59]. Therefore in our simulation we set both the tensile and shear strength for pristine GBs at 400 MPa. In our simulations we assume that G_{IC} (critical energy release rate for Mode I fracture)

will dominate the fracture process. Therefore, G_{IIC} (critical energy release rate for Mode II fracture) is set to be much larger than G_{IC}. From our previous DFT calculations, the typical GB G_{IC} or GB strength before oxidation in Ni is around 3.5 J/m^2; When GBs are oxidized, the GB G_{IC} drops to around half of its pristine value in average. It should be noted that the GB G_{IC} obtained from our DFT calculations is the minimum energy per GB area required for a perfectly brittle fracture at a GB. Since in reality the plastic deformation always occurs during the cracking process, as an approximation, we set the G_{IC} = 10 J/m^2 for pristine GBs and 5 J/m^2 for oxidized (weak) GBs so that the reduction ratio is similar as in DFT calculations. To simulate intergranular fracture, we manually choose 2 different weak/oxidized paths. The two weak path configurations are shown in Figure 19.

Table 13. Parameters for bilinear mix-mode model with B-K criterion for modeling alloy 82/182.

G_{IC} (critical energy release rate for Mode I)	10 J/m^2 (pristine); 5 J/m^2 (weak/oxidized)
G_{IIC} (critical energy release rate for Mode II)	30 J/m^2 (pristine); 15 J/m^2 (weak/oxidized)
N (normal strength)	400 MPa (pristine); 200 MPa (weak/oxidized)
S (shear strength)	400 MPa (pristine); 200 MPa (weak/oxidized)
K (penalty stiffness)	2×10^5 MPa/m
η	2.4
Elastic constant (GPa)	279.8 154.7 154.4 0 0 0 154.7 277.8 153.4 0 0 0 154.4 153.4 277.2 0 0 0 0 0 0 131.3 0 0 0 0 0 0 129.6 0 0 0 0 0 0 130.1

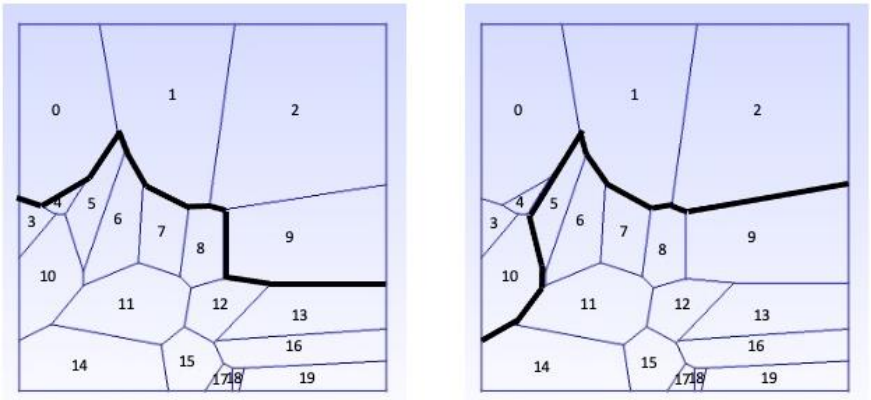

Figure 19. Two manually assigned weak paths (black solid lines) in the polycrystalline Ni-base alloys. The weak paths (thick black lines) represent oxidized GBs. The properties of pristine and oxidized GBs in Ni-base alloys are listed in Table 13. (a) Weak Path #1. (b) Weak Path #2.

To fracture these samples, a tensile stress is imposed through a prescribed displacement on the top boundary of each sample, and the results are shown in Figures 20 – 22. Note in these microstructure figures, the color scheme is used for visualization purpose and does not have fracture-related physical meaning. Figure 20 shows the fracture path in the pristine sample. With the applied tensile stress in the vertical direction, the opening cracks are mostly perpendicular to the loading direction, indicating that the Mode I fracture dominates. The fracture stress (largest stress) is about 390 MPa, close to our pre-defined tensile strength (400 MPa) from the stress-displacement curve. When there exists a weak path, the actual fracture path may or may not be the same as the weak path, depending on the configuration, as shown below.

Figure 21 shows the fracture result with the Weak Path #1 (shown in Figure 19a). In this specific example, the actual fracture path is consistent with our pre-defined one. We found that the fracture starts from the edge and then propagates to middle region. In this example, most of the fractured GBs are perpendicular to the loading direction, indicating that the Mode I fracture still dominates. However, one fractured GB (indicated by the black circle in Figure 21) is almost parallel to the loading direction. It can be clearly seen that some shear sliding occurs at this GB, indicating this is a Model II fracture, even though the G_{IIC} is 3 times higher than G_{IC}. The fracture stress for this weak path is around 240 MPa, which is much lower than the pristine one (390 MPa).

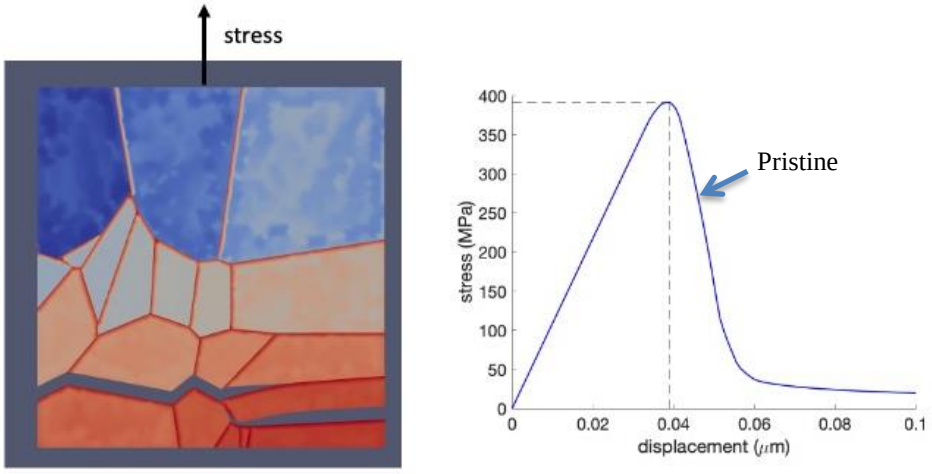

Figure 20. MOOSE-based CZM modeling of intergranular fracture in a pristine (i.e., before oxidation) polycrystalline Ni-base alloy. The tensile stress is applied on the top domain boundary while the bottom domain boundary is fixed. The left figure shows the fracture path, and the right figure shows the stress vs displacement curve.

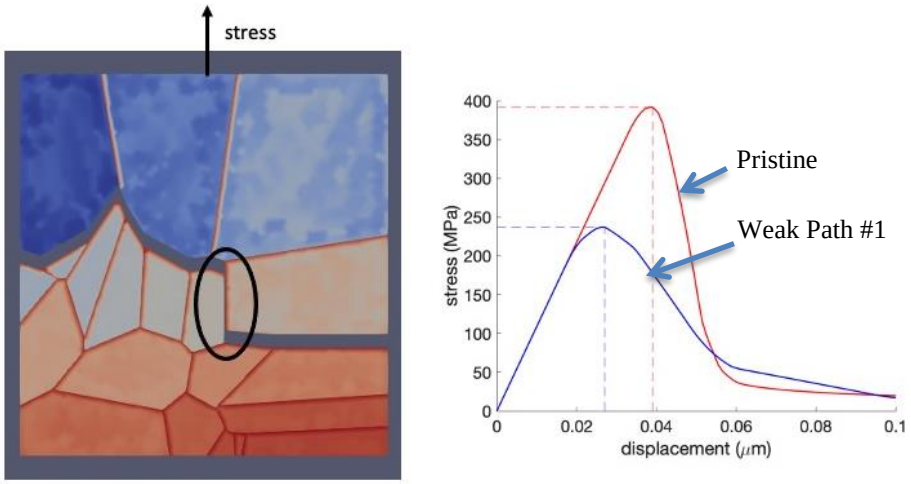

Figure 21. MOOSE-based CZM modeling of intergranular fracture in a polycrystalline Ni-base alloy with a pre-defined weak/oxidized path (Weak Path #1). The tensile stress is applied on the top domain boundary while the bottom domain boundary is fixed. The left figure shows the fracture path, and the right figure shows the stress vs displacement curve. The black circle in the left figure indicates that the weak GB is parallel to the stress and fractures through shear sliding.

Figure 22 shows the fracture result with the Weak Path #2 (shown in Figure 19b). In this example we found that the actual fracture path propagates mostly along the pre-defined weak GBs

except for the GBs inside the black circle. These weak GBs do not crack from our simulation result. Instead, the crack prefers to propagate along the horizontal direction even though those GBs are strong (pristine). Again, our simulation result shows that the crack still starts from the left and right edges and propagates towards the center. When both cracks reach the triple junctions around black circle region shown in Figure 22, the GBs inside this region may be under a compression condition, which can divert the cracks to other paths, even though the GBs in those paths are strong. This example demonstrates that the GB strength is not the only factor that determines the fracture path. The fracture propagation is the interplay of the loading direction, GB strength, and interactions between neighboring grains. The final fracture stress is around 210 MPa, which is lower than that with Weak Path #1 (240 GPa).

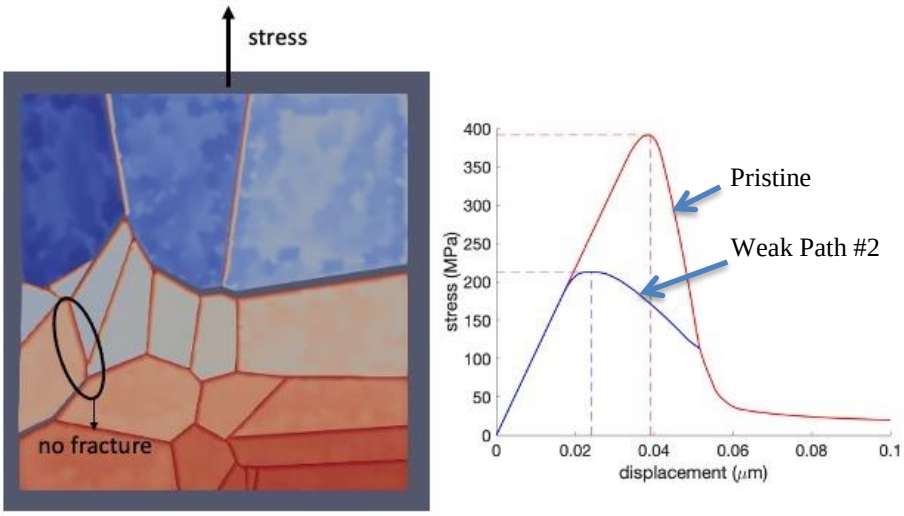

Figure 22. MOOSE-based CZM modeling of intergranular fracture in a polycrystalline Ni-base alloy with a pre-defined weak/oxidized path (Weak Path #2). The tensile stress is applied on the top domain boundary while the bottom domain boundary is fixed. The left figure shows the fracture path, and the right figure shows the stress vs displacement curve. The black circle in the left figure indicates the weak GBs that do not fracture during tensile loading.

For modeling alloys 308/309, the input tensile and shear strengths are slightly lower than those for nickel-base alloys because the elastic constants of the stainless steels are lower. The parameters are shown in Table 14. For the pristine polycrystal sample, the same GB structure as for the Ni-base alloys (Figure 18) is used. The tensile stress is also applied on the top of the domain boundary through a prescribed displacement. As shown in Figure 23, the fracture GBs are still

mainly perpendicular to the loading direction. The cracks occur on both top and bottom, which are different from the results for the pristine Ni-based alloys (Figure 20), although they use the same polycrystal structure. The fracture stress for the pristine Fe-base alloys is around 350 MPa, which is close to the tensile strength (360 MPa).

Table 14. Parameters for bilinear mix-mode model with B-K criterion for modeling alloy 308/309.

G_{IC} (critical energy release rate for Mode I)	10 J/m^2 (pristine); 5 J/m^2 (weak/oxidized)
G_{IIC} (critical energy release rate for Mode II)	30 J/m^2 (pristine); 15 J/m^2 (weak/oxidized)
N (normal strength)	360 MPa (pristine); 180 MPa (weak/oxidized)
S (shear strength)	360 MPa (pristine); 180 MPa (weak/oxidized)
K (penalty stiffness)	2×10^5 MPa/m
η	2.4
Elastic constant （GPa）	$\begin{matrix} 211 & 137 & 137 & 0 & 0 & 0 \\ 137 & 211 & 211 & 0 & 0 & 0 \\ 137 & 137 & 211 & 0 & 0 & 0 \\ 0 & 0 & 0 & 130 & 0 & 0 \\ 0 & 0 & 0 & 0 & 130 & 0 \\ 0 & 0 & 0 & 0 & 0 & 130 \end{matrix}$

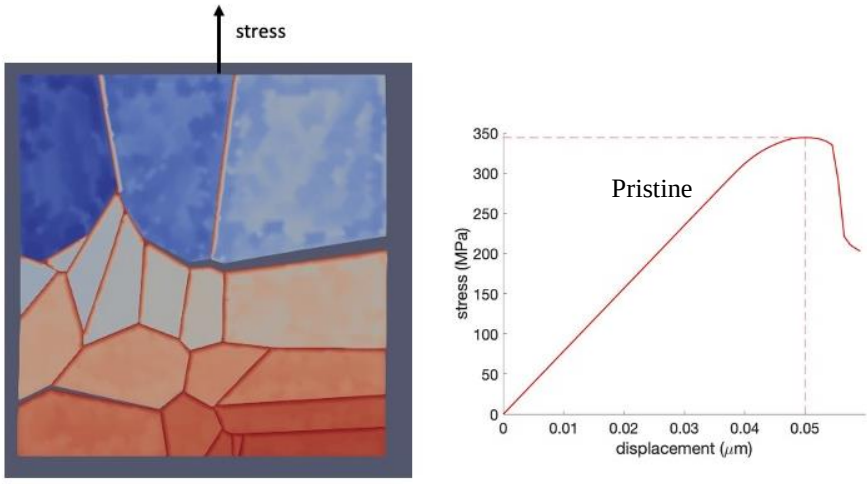

Figure 23. MOOSE-based CZM modeling of intergranular fracture in a pristine (i.e., before oxidation) polycrystalline Fe-base alloy. The tensile stress is applied on the top domain boundary while the bottom domain boundary is fixed. The left figure shows the fracture path, and the right figure shows the stress vs displacement curve.

Instead of setting a continuous weak path, we randomly assign five discontinuous weak/oxidized GBs for the Fe-base alloy, as shown in Figure 24a. Four of them are perpendicular to the loading direction, while one is parallel (the GB between grains 11 & 12). The fracture path is shown in Figure 24b. The fracture completely propagates along the bottom side of the sample. The fracture path overlaps with two weak GBs (between grains 6 & 11, grains 9 & 12). In the pristine case (Figure 23), one fracture path is close to the topside of the sample. However, even we add some weak GBs (between grains 1 & 7, grains 0 & 4) along this path, the crack still does not occur along this path. The reason could be that the two GBs in the current fracture path are more favorably oriented with the loading direction than the other two weak GBs. In this example, the GB that is parallel to the loading direction (between grains #11 & 12) does not fracture. The fracture stress with randomly distributed weak GBs is about 290 MPa, only slightly lower than the pristine case (350 MPa), as shown in Figure 24c. This is different from the cases for the Ni-base alloy containing a continuous weak path, in which the fracture stress drops about 50% of the pristine value. This result indicates that the percolation extent of the weak path is another important factor for the crack propagation.

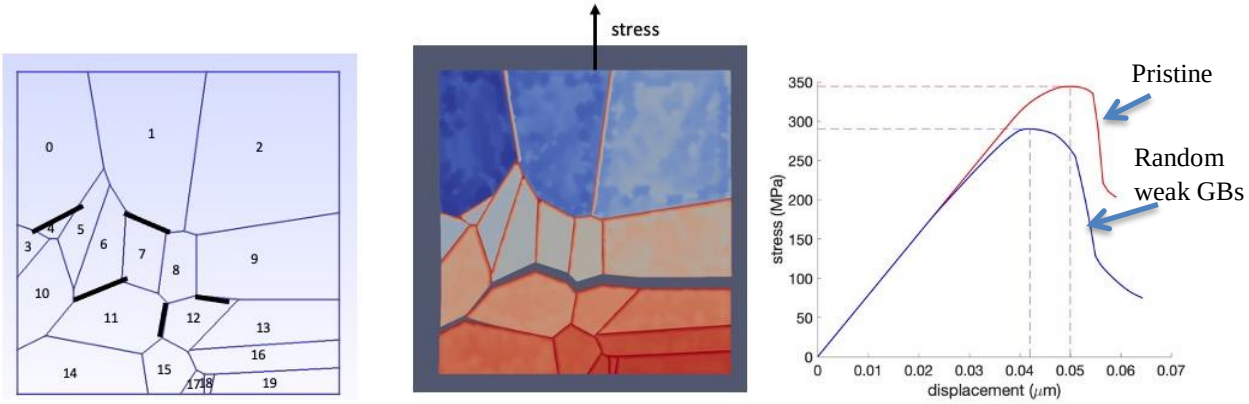

(a) (b) (c)

Figure 24. MOOSE-based CZM modeling of intergranular fracture in a polycrystalline Fe-base alloy with randomly distributed weak/oxidized GBs. (a) The random distribution of weak GBs, as indicated by black solid lines. (b) The actual fracture path when a tensile loading is applied on the top. (c) The stress vs displacement curve.

In summary, we have applied the cohesive zone model (CZM) that is based on the bilinear mixed mode traction separation law in the MOOSE framework to study the SCC-induced intergranular fracture behavior in both polycrystalline Ni-base (for modeling alloys 82/182) and Fe-base (for modeling alloys 308/309) alloys at the microstructural length scale. We use our previous DFT results and experimental values to justify the input parameters for our model. In our simulations, different weak/oxidized paths are used, including both continuous and discontinuous paths. Overall, we found that the fracture prefers to occur at weak GBs with orientations perpendicular to the loading direction. However, we also found that the fracture may not always occur along the weak GBs. In some circumstances, fracture can occur at weak GBs that are parallel to the loading direction through a shear sliding mechanism. In addition, some strong (pristine) GBs near triple junctions also can fracture. Regardless, the presence of weak (oxidized) GBs can facilitate the fracture initiation and propagation, as evident by the drop of fracture stress. The drop of fracture stress depends on the distribution of weak paths: percolated weak paths lead to a larger drop while discontinuous weak paths result in a smaller drop. Our results demonstrate that the reduction in GB strength due to oxidation is not the only factor that determines the fracture path. The fracture propagation is the interplay of the loading direction, GB strength, distribution of weak GBs, and interactions between neighboring grains. This work also shows that the CZM model in MOOSE can be a very useful tool for studying the SCC problems under tensile loading.

9. References

[1] W.-Y. Chen, M. Li, X. Zhang, M. A. Kirk, P. M. Baldo, and T. Lian, *In situ TEM study of G-phase precipitates under heavy ion irradiation in CF8 cast austenitic stainless steel*, Journal of Nuclear Materials **464**, 185 (2015).

[2] X. Lin, Q. Peng, J. Mei, E.-H. Han, W. Ke, L. Qiao, and Z. Jiao, *Corrosion of phase and phase boundary in proton-irradiated 308L stainless steel weld metal in simulated PWR primary water*, Corrosion Science **165**, 108401 (2020).

[3] W. Sun, R. Marceau, M. Styles, D. Barbier, and C. Hutchinson, *G phase precipitation and strengthening in ultra-high strength ferritic steels: Towards lean 'maraging' metallurgy*, Acta Materialia **130**, 28 (2017).

[4] S. J. Ahmed, J. E. Greedan, C. Boyer, and M. Niewczas, *Magnetic and Structural Studies of G-Phase Compound Mn6Ni16Si7*, Inorganic chemistry **57**, 14144 (2018).

[5] D. King, M. Yang, T. Whiting, X. Liu, and M. Wenman, *G-phase strengthened iron alloys by design*, Acta Materialia **183**, 350 (2020).

[6] G. Kresse, and D. Joubert, *From ultrasoft pseudopotentials to the projector augmented-wave method*, Physical Review B **59**, 1758 (1999).

[7] J. P. Perdew, K. Burke, and M. Ernzerhof, *Generalized gradient approximation made simple*, Physical review letters **77**, 3865 (1996).

[8] E. Yelsukov, E. Voronina, and V. Barinov, *Mössbauer study of magnetic properties formation in disordered Fe-Al alloys*, Journal of magnetism and magnetic materials **115**, 271 (1992).

[9] Z. Łodziana, N.-Y. Topsøe, and J. K. Nørskov, *A negative surface energy for alumina*, Nature materials **3**, 289 (2004).

[10] Z. Łodziana, N.-Y. Topsøe, and J. K. Nørskov, *Negative surface energy—clearing up confusion*, Nature materials **4**, 186 (2005).

[11] R. Smallman, and A. Ngan, *Morden Physical Metallurgy* (Butterworth-Heinemann, Oxford, UK, 2014).

[12] H. Fredriksson, and J. Stjerndahl, *Solidification of iron-base alloys*, Metal science **16**, 575 (1982).

[13] E. Hämäläinen, A. Laitinen, H. Hänninen, and J. Liimatainen, *Mechanical properties of powder metallurgy duplex stainless steels*, Materials science and technology **13**, 103 (1997).

[14] M. Campos, A. Bautista, D. Caceres, J. Abenojar, and J. Torralba, *Study of the interfaces between austenite and ferrite grains in P/M duplex stainless steels*, Journal of the European Ceramic Society **23**, 2813 (2003).

[15] H. Mehrer, *Diffusion in solids: fundamentals, methods, materials, diffusion-controlled processes* (Springer Science & Business Media, 2007), Vol. 155.

[16] D. James, and G. Leak, *Self-diffusion and diffusion of cobalt in alpha and delta-iron*, The Philosophical Magazine: A Journal of Theoretical Experimental and Applied Physics **14**, 701 (1966).

[17] C.-X. Guo, O. Warschkow, D. E. Ellis, V. P. Dravid, and E. C. Dickey, *Oxide–Oxide Interfaces: Atomistic and Density Functional Study of Cubic-ZrO2 (100) ∥ NiO (111)*, Journal of the American Ceramic Society **84**, 2677 (2001).

[18] S. Plimpton, *Fast Parallel Algorithms for Short-Range Molecular Dynamics*, Journal of Computational Physics **117**, 1 (1995).

[19] N. H. de Leeuw, and T. G. Cooper, *Surface simulation studies of the hydration of white rust Fe(OH)2, goethite α-FeO(OH) and hematite α-Fe2O3*, Geochimica et Cosmochimica Acta **71**, 1655 (2007).

[20] D. T. Ta, A. K. Tieu, H. T. Zhu, and B. Kosasih, *Thin film lubrication of hexadecane confined by iron and iron oxide surfaces: A crucial role of surface structure*, The Journal of Chemical Physics **143**, 164702 (2015).

[21] H. Guo, and A. S. Barnard, *Modeling the iron oxides and oxyhydroxides for the prediction of environmentally sensitive phase transformations*, Physical Review B **83**, 094112 (2011).

[22] S. M. Bruemmer, M. J. Olszta, M. B. Toloczko, and D. K. Schreiber, *Grain boundary selective oxidation and intergranular stress corrosion crack growth of high-purity nickel binary alloys in high-temperature hydrogenated water*, Corrosion Science **131**, 310 (2018).

[23] G. S. Was *et al.*, *Corrosion and stress corrosion cracking in supercritical water*, Journal of Nuclear Materials **371**, 176 (2007).

[24] J. R. Rice, and J.-S. Wang, *Embrittlement of interfaces by solute segregation*, Materials Science and Engineering: A **107**, 23 (1989).

[25] R. W. Balluffi, A. Brokman, and A. H. King, *CSL/DSC Lattice model for general crystalcrystal boundaries and their line defects*, Acta Metallurgica **30**, 1453 (1982).

[26] G. Kresse, and J. Furthmüller, *Efficient iterative schemes for ab initio total-energy calculations using a plane-wave basis set*, Physical Review B **54**, 11169 (1996).

[27] G. Kresse, and J. Furthmüller, *Efficiency of ab-initio total energy calculations for metals and semiconductors using a plane-wave basis set*, Computational Materials Science **6**, 15 (1996).

[28] J. P. Perdew, K. Burke, and M. Ernzerhof, *Generalized Gradient Approximation Made Simple*, Physical Review Letters **77**, 3865 (1996).

[29] P. E. Blöchl, *Projector augmented-wave method*, Physical Review B **50**, 17953 (1994).

[30] P. Haas, F. Tran, and P. Blaha, *Calculation of the lattice constant of solids with semilocal functionals*, Physical Review B **79**, 085104 (2009).

[31] M. D. Towler, N. L. Allan, N. M. Harrison, V. R. Saunders, W. C. Mackrodt, and E. Aprà, *Ab initio study of MnO and NiO*, Physical Review B **50**, 5041 (1994).

[32] M. O. Løvvik, D. Zhao, Y. Li, R. Bredesen, and T. Peters, *Grain Boundary Segregation in Pd-Cu-Ag Alloys for High Permeability Hydrogen Separation Membranes*, Membranes **8** (2018).

[33] D. J. Siegel, and J. C. Hamilton, *Computational study of carbon segregation and diffusion within a nickel grain boundary*, Acta Materialia **53**, 87 (2005).

[34] M. Všianská, and M. Šob, *The effect of segregated sp-impurities on grain-boundary and surface structure, magnetism and embrittlement in nickel*, Progress in Materials Science **56**, 817 (2011).

[35] J.-M. Zhang, F. Ma, and K.-W. Xu, *Calculation of the surface energy of FCC metals with modified embedded-atom method*, Applied Surface Science **229**, 34 (2004).

[36] C. Jiang, S. A. Maloy, and S. G. Srinivasan, *A computational method to identify interstitial sites in complex materials*, Scripta Materialia **58**, 739 (2008).

[37] H. H. Pham, and T. Cagin, *Fundamental studies on stress-corrosion cracking in iron and underlying mechanisms*, Acta Materialia **58**, 5142 (2010).

[38] Y. A. Du, L. Ismer, J. Rogal, T. Hickel, J. Neugebauer, and R. Drautz, *First-principles study on the interaction of H interstitials with grain boundaries in $\ensuremath{\alpha}$- and $\ensuremath{\gamma}$-Fe*, Physical Review B **84**, 144121 (2011).

[39] G. S. Was, *Fundamentals of Radiation Materials Science: Metals and Alloys (2nd Ed.)* (Springer, New York, NY, 2017).

[40] T. R. Allen, L. Tan, G. S. Was, and E. A. Kenik, *Thermal and radiation-induced segregation in model Ni-base alloys*, Journal of Nuclear Materials **361**, 174 (2007).

[41] https://computation.llnl.gov/projects/sundials.

[42] L. Barnard, J. D. Tucker, S. Choudhury, T. R. Allen, and D. Morgan, *Modeling radiation induced segregation in Ni–Cr model alloys from first principles*, Journal of Nuclear Materials **425**, 8 (2012).

[43] T. R. Allen, and G. S. Was, *Modeling radiation-induced segregation in austenitic Fe–Cr–Ni alloys*, Acta Materialia **46**, 3679 (1998).

[44] L. Barnard, and D. Morgan, *Ab initio molecular dynamics simulation of interstitial diffusion in Ni–Cr alloys and implications for radiation induced segregation*, Journal of Nuclear Materials **449**, 225 (2014).

[45] J. D. Tucker, R. Najafabadi, T. R. Allen, and D. Morgan, *Ab initio-based diffusion theory and tracer diffusion in Ni–Cr and Ni–Fe alloys*, Journal of Nuclear Materials **405**, 216 (2010).

[46] X.-M. Bai, H. Ke, Y. Zhang, and B. W. Spencer, *Modeling copper precipitation hardening and embrittlement in a dilute Fe-0.3at.%Cu alloy under neutron irradiation*, Journal of Nuclear Materials **495**, 442 (2017).

[47] S. Watanabe, N. Sakaguchi, K. Kurome, M. Nakamura, and H. Takahashi, *On the mechanism of radiation-induced segregation*, Journal of Nuclear Materials **240**, 251 (1997).

[48] C. M. Barr *et al.*, *Grain boundary character dependence of radiation-induced segregation in a model Ni–Cr alloy*, Journal of Materials Research **30**, 1290 (2015).

[49] A. J. Ardell, *Radiation-Induced Solute Segregation in Alloys*, in *Materials Issues for Generation IV Systems*, edited by V. Ghetta *et al.* (Springer Netherlands, 2008), pp. 285.

[50] Z. Li, X. Zhan, X.-M. Bai, S.-C. Lee, W. Zhong, B. J. Sutton, and B. J. Heuser, *Modified microstructures in proton irradiated dual phase 308L weldment filler material*, Journal of Nuclear Materials **548**, 152825 (2021).

[51] C. J. Permann *et al.*, *MOOSE: Enabling massively parallel multiphysics simulation*, SoftwareX **11**, 100430 (2020).

[52] Z. Zhang, W. Jiang, J. E. Dolbow, and B. W. Spencer, *A modified moment-fitted integration scheme for X-FEM applications with history-dependent material data*, Computational Mechanics **62**, 233 (2018).

[53] W. Jiang, B. W. Spencer, and J. E. Dolbow, *Ceramic nuclear fuel fracture modeling with the extended finite element method*, Engineering Fracture Mechanics **223**, 106713 (2020).

[54] A. Hansbo, and P. Hansbo, *A finite element method for the simulation of strong and weak discontinuities in solid mechanics*, Computer Methods in Applied Mechanics and Engineering **193**, 3523 (2004).

[55] N. Moës, and T. Belytschko, *Extended finite element method for cohesive crack growth*, Engineering Fracture Mechanics **69**, 813 (2002).

[56] A. Rovinelli, M. C. Messner, and T. L. Sham, United States, 2020).

[57] P. Camanho, and C. Dávila, *Mixed-Mode Decohesion Finite Elements for the Simulation of Delamination in Composite Materials*, (2002).

[58] C. Geuzaine, and J.-F. Remacle, *Gmsh: A 3-D finite element mesh generator with built-in pre- and post-processing facilities*, International Journal for Numerical Methods in Engineering **79**, 1309 (2009).

[59] A. Telang *et al.*, *Surface grain boundary engineering of Alloy 600 for improved resistance to stress corrosion cracking*, Materials Science and Engineering: A **648**, 280 (2015).

5. Publications, technical presentations, acknowledgements, and lessons learned.

Publications

1. Zhong, W., Lin, J. L., Chen, Y., Li, Z., An, K., Sutton, B. J., & Heuser, B. J. (2021). "Microstructure, Hardness, and Residual Stress of the Dissimilar Metal Weldments of SA508-309L/308L-304L," Metallurgical and Materials Transactions A, 52(5), 1927-1938.
2. Li, Z., Zhan, X., Bai, X. M., Lee, S. C., Zhong, W., Sutton, B. J., & Heuser, B. J. (2021). "Modified microstructures in proton irradiated dual phase 308L weldment filler material," Journal of Nuclear Materials, 548, 152825.
3. Zhen Li, Xun Zhan, Weicheng Zhong, Benjamin J. Sutton, Brent J. Heuser, "Quantification of Precipitation, Clustering, and Void Formation in Proton Irradiated Dual Phase 308L Weldment Filler Materials," submitted Journal of Nuclear Materials, 2022.
4. Zhen Li, Xun Zhan, Weicheng Zhong, Benjamin J. Sutton, Brent J. Heuser, SCC and IASCC "Mechanisms in SA508-304L Weldments Subjected to BWR NWC environments," in preparation for a peer-review journal.
5. Z. Xiao and X.M. Bai, "First principal studies of oxidation effect on grain boundary strength in nickel", draft manuscript, in preparation for a peer-review journal.

Presentations

1. Zhen Li, Xun Zhan, X.M. Bai, Shao-Chun Lee, Weicheng Zhong, Benjamin J. Sutton, Brent J. Heuser, "Selective Irradiation Behavior in Dual Phase 308L Filler of SA508-304L Dissimilar Metal Weldment after Proton Irradiation," MiNES, October 2019, Baltimore, MD.
2. Zhen Li, Xun Zhan, X.M. Bai, Shao-Chun Lee, Weicheng Zhong, Benjamin J. Sutton, Brent J. Heuser, "Selective Irradiation Behavior in Dual Phase 308L Filler of SA508-304L Dissimilar Metal Weldment after Proton Irradiation," MS&T, October 2020, virtual
3. Zhen Li, Weicheng Zhong, Gary S. Was, Brent J. Heuser, "Irradiation Assisted Stress Corrosion Cracking in SA508-304 Weldment under BWR/NWC Simulated Environment," MS&T, October 2021, Columbus, Ohio.
4. X.M. Bai, "Computer Modeling of Radiation and Oxidation Effects in Ni- and Fe-base Alloys", Department of Engineering Physics, University of Wisconsin – Madison, 10/2021 (invited department seminar).
5. Z. Xiao and X.M. Bai, "Modeling Effects of Oxidation and Solute Segregation on Grain Boundary Fracture in Nickel-Based Alloys", 2020 International Conference on Plasticity, Damage, and Fracture, Riviera Maya, Mexico, 01/2020. (Keynote presentation).
6. Z. Xiao and X.M. Bai, "Density Functional Theory Studies of Effects of Oxidation on Grain Boundary Fracture in Nickel", 2019 Materials in Nuclear Energy Systems (MiNES) Conference, Baltimore, MD, 10/2019.
7. Z. Xiao and X.M. Bai, "First-Principles Studies of Effects of Oxygen Impurity on Grain Boundary Strength in Nickel", 2019 Materials Research Society (MRS) Spring Meeting, Phoenix, AZ, 04/2019.

Acknowledgements

This work was supported by the US Department of Energy Nuclear Energy University Programs (NEUP) under contract number DE NE0008699. A portion of the experiments presented here were carried out at the Materials Research Laboratory Central Research Facilities, University of Illinois. The Michigan Ion

Beam Laboratory was used to perform the proton irradiation exposures. The B.J.H. at UIUC is grateful to Dr. Ovidiu Toader for support in performing the irradiations, as well as Dr. Miao Song for help with sample electropolishing prior to proton irradiation. Much of the experimental work at UIUC was performed by Dr. Z. Li, a PDRA in the PI Heuser's research group. Atom probe tomography measurement and data analysis training was provided to this project at no cost by the UIUC MRL and this is gratefully acknowledged, as are Drs. M. Sardela and W. Swiech at UIUC. Much of the modeling work was performed or initiated by Z. Xiao and W. Chen, graduate students in Co-PI Bai's research group at Virginia Tech. A portion of the modeling work was performed using the high performance computing facilities at the Advanced Research Computing at Virginia Tech. X.M.B. at Virginia Tech also acknowledges the Faculty Joint Appointment Program at Idaho National Laboratory. The DFT modeling of the G phase by X.M.B. made use of the resources of the High Performance Computing Center at Idaho National Laboratory, which is supported by the Office of Nuclear Energy of the U.S. Department of Energy and the Nuclear Science User Facilities under Contract No. DE-AC07-05ID14517.

Lessons learned

1. Access to a well-functioning autoclave with a load frame for immersion testing is obviously critical. Measurement of dissolved oxygen, water conductivity, and pH (water analytics) are necessary. Stable temperature, pressure, applied load, and dissolved oxygen control are required over the course of days to weeks. The ability to measure electrochemical corrosion potential is helpful but was not necessary for this work. The autoclave used for this work did not have ECP measurement capability.
2. Analysis of cracking after immersion testing was complicated by extensive spinel formation on the wetted surfaces. Spinel formation is unavoidable in autoclave immersion tests. Chemical washes used by others on single phase austenitic steels attacked the γ–δ phase boundaries present in the duplex microstructure of recrystallized 308L and 309L weld filler and butter. A chemical wash that does not attack these phase boundaries would facilitate the identification of crack initiation sites on the surface. We resorted to pulling to failure to induce visible surface cracking in the presence of the spinel crystals decorating the free surface.
3. The more aggressive BWR NWC autoclave environment with high dissolved oxygen levels (2000 ppb wt. DO) was helpful and likely necessary to facilitate SCC in reasonable immersion testing periods.
4. One immersion testing procedure we did not use was to pull to a large strain (4-6%) and then hold for an extended period of time. This may have resulted in cracking similar to that induced by pulling to failure, but without specimen failure.
5. The study of SCC and IASCC of SA508-304L weldments must take into account microstructure variation of the butter. The butter is subjected to a post-weld heat treatment. Carbon diffusion from SA508 induces a dilution zone of single phase γ austenite. Further, $Cr_{23}C_6$ intergranular carbides form at the γ–δ phase boundaries in the duplex region next to the dilution zone. This does not occur in the 308L groove filler or the 309L butter at locations far removed from the dilution zone.
6. 304L austenite used here was not a single phase material, but contained δ ferrite lamella. These are occasionally observed in austenitic steels and are due to deformation induced by hot rolling. Although this microstructure did not influence the behavior of 304L austenite in this work, it could potentially affect the study of SCC.

7. Characterization of residual stresses is important since weldments are known to have large residual stresses. Neutron diffraction is an ideal characterization tool to quantify residual stress provided an engineering diffractometer is used with sufficient incident intensity to allow for small probe volume. However this analysis is time consuming since sample preparation is unique. One critical aspect of residual stress characterization with diffraction is a strain-relieved d_o specimen. The lattice parameter is a function of composition and this dictates a d_o specimen from the weldment. Strain relief is done by creating a "comb" sample were each interrogation voxel is only connected along one edge to a single neighboring voxel. We believe our comb sample did not have complete lattice strain relief, but this was impossible to prove. As a consequence, the measured residual stresses (residual strains are actually measured and then converted to residual stress) may be affected by residual lattice strain in the d_o specimen.

8. Atom probe tomography is a useful but not necessary tool for this work. APT is time consuming and expensive. The APT work performed here was provided at no cost by the UIUC MRL. Most if not all of the APT analysis was redundant with TEM and STEM-EDS. The exception was the Ni-Si cluster morphology and composition analysis provided by APT; no analogy was provided by the electron-based microanalytical analysis tools we used.

9. The ability to perform FIB lift outs at specific locations is critical to identification of the factors influencing SCC and IASCC. This ability is complicated by spinel formation on the free surface and led us to pull specimens to failure, as mentioned above. Access to a FIB with SEM capability is necessary.

10. Access to a state of the art TEM/STEM instrument is crucial for microstructure analysis. We relied heavily on the UIUC MRL Themis Z analytical TEM/STEM with enhanced EDS detection capability. This instrument allowed us to perform elemental mapping, characterize matrix G phase and intergranular $Cr_{23}C_6$ precipitation, quantify Cr depletion and Ni segregation due to RIS, quantify void and G phase variation with depth and demonstrate that this scales with dpa, and correlate cracking to microstructural features such as the intergranular $Cr_{23}C_6$ precipitates and Cr depleted grain and phase boundaries.

11. The radiation-induced segregation (RIS) model has many input parameters and some of them are empirical. The model prediction is also sensitive to these parameters. In our work, we only have one experimental RIS data set near a grain boundary in 308L. Although the current RIS model matches well with this specific experimental measurement, the model might not quantitatively predict other grain boundaries or radiation conditions well. To have a more robust model, more experimental data are needed for calibration.

12. The current extended finite element method (XFEM) in the MOOSE/Grizzly has some limitations for handling the triple junctions in polycrystalline materials and thus it is currently not suitable for modeling intergranular fracture. To solve this problem, we have used a more mature cohesive zone model (CZM) to model the intergranular fracture related to stress corrosion cracking (SCC) in both Ni- and Fe-based alloys. The CZM results look very reasonable.

13. The empirical potentials for molecular dynamics simulations have some limitations after our evaluation. They are also not suitable for modeling partially oxidized grain boundaries as well as the metal/oxide interface. To solve these challenges, density functional theory (DFT) modeling is used. However, the computational cost of DFT is expensive so that only some special grain boundaries with small system sizes can be simulated.

14. The grain boundary strength obtained from DFT modeling is for ideal brittle fracture and ignores the plastic deformation contribution. If the atomistic-level DFT results are used directly in the continuum-scale CZM modeling, they are too small and can cause convergence problems. Therefore, the grain boundary strengths used in CZM modeling are much larger than the DFT results. However, the reduction ratio of grain boundary strength due to oxidation obtained from the DFT modeling is used to inform the parameter selection in the CZM modeling.